NUMERICAL SIMULATION OF STRUCTURAL, ELECTRONIC, OPTICAL AND THERMAL PROPERTIES OF PLATINUM DICHALCOGENIDES

Submitted by: Chris Nhamo Maregedze

(1420375)

Supervised by: Professor Daniel Joubert

A dissertation submitted to the Faculty of Science,
University of Witwatersrand in fulfillment
of the requirements for the degree of Master of Science (MSc).

School of Physics,
University of Witwatersrand,
Johannesburg

May, 2019

DECLARATION

I declare that this dissertation is my own and unaided work under the supervision of Professor Daniel Joubert. It is being submitted for the Degree of Master of Science at the University of the Witwatersrand, Johannesburg. This dissertation has not been submitted before for any degree at any other University and may not be reproduced for any purpose without prior permission of the author or the University of Witwatersrand.

Chris Nhamo Maregedze

15th day of May 2019 in Johannesburg

ABSTRACT

An ever-growing interest in transition metal chalcogenide materials due to their intriguing properties has led to extensive investigations of their structural, electronic, optical and thermal properties and their applications as building blocks for optoelectric and thermoelectric devices.

Properties of PtS_2, $PtSe_2$ and $PtTe_2$ were investigated from first principles DFT calculations. PBE+TS functional had lattice parameters more comparable to experimental volume and were therefore used for further studies. Phonon and elastic constants calculations confirmed dynamical and mechanical stability.

Pt was the dominant contributor to acoustic modes and as volume increased from S, Se to Te the frequency dispersion of acoustic modes decreased. Their bulk moduli increased as volume increased.

Electronic, optical and thermal properties were explored to ascertain suitability as building blocks for optoelectric and thermoelectric devices. Optical properties illustrated anisotropy within the visible range, 1.6 eV-3.1 eV. Lattice thermal conductivity at 300K in out-of-plane was observed to be much lower compared to in-plane for all the materials.

DEDICATION

In memory of my late mother and father

Alice Maregedze

1957-2005

Sylvester Maregedze

1949-2014

ACKNOWLEDGEMENTS

First and foremost, I thank the Almighty God for giving me the opportunity to further my studies. I am grateful for my lovely wife Nonkululeko Octavia and my son Shaun Tafadzwa for their unconditional support and motivation throughout the duration of my studies.

Special mention also goes to my family for their support during the course of my studies. My sincere gratitude goes to my supervisor, Professor Daniel Joubert for his insurmountable support and professional assistance towards my studies.

Special thanks to my mentor and colleague, Elkana Rugut for his professional support and guidance throughout the duration of my studies as well as PhD students from the school of Physics.

CONTENTS

List of figures

List of Tables

1 Introduction

Every global era in the history of mankind is characterized by materials used in it. In 2004 [1] a new era in material science was opened: the era of graphene or, commonly known as two-dimensional (2-D) materials. Graphene, a 2-D honey-comb structure of carbon is a one-atom-thick layer of carbon atoms arranged in a hexagonal lattice [2]. It is the building-block of graphite (which is used, among others things, in pencil tips), but graphene is a remarkable substance on its own with a multitude of astonishing properties [3].

The pioneer of 2-D materials, graphene, was first isolated in 2004 which sparked intense activity in fundamental research laboratories everywhere across the globe. Graphene is the thinnest material known to mankind at one atom thick, and also incredibly strong - about 200 times stronger than steel, meaning the material has the potential to make better electronics, more effective solar cells [4], and could even be used in medicine. On top of that, graphene is an excellent conductor of heat and electricity and has fascinating light absorption abilities. An ever-growing interest in the various layered 2-D materials has led to an extensive investigation of their electronic, mechanical, and optical properties and their application towards different devices [5]. Graphene's major weakness is its lack of a bandgap [6], which is what makes silicon and other semiconductors useful for digital electronics. A bandgap allows electrical conduction through a material to be turned on and off, which is crucial for building a transistor (a semiconductor device used to amplify or switch electronic signals and electrical power). This led to more research in order to tune the bandgap [7][8].

Like carbon which has different allotropes, Transition Metal Dichalcogenides (TMDs), in addition to multi-layered systems have several polymorphs with different dimensionalities as shown in Fig 1.1 below. In their 2-D form, TMDs exhibit a slew of different properties, from semiconducting to metallic to superconducting. Some of

them even behave as topological insulators; that is, most of the material is insulating while only the very perimeter conducts electricity [9][10].

Bulk (or 3-D) TMDs have been known and used for a very long time, though most of the older applications (i.e. as solid lubricants) were related to their unique mechanical properties determined by the presence of van der Waals bonding between the layers.

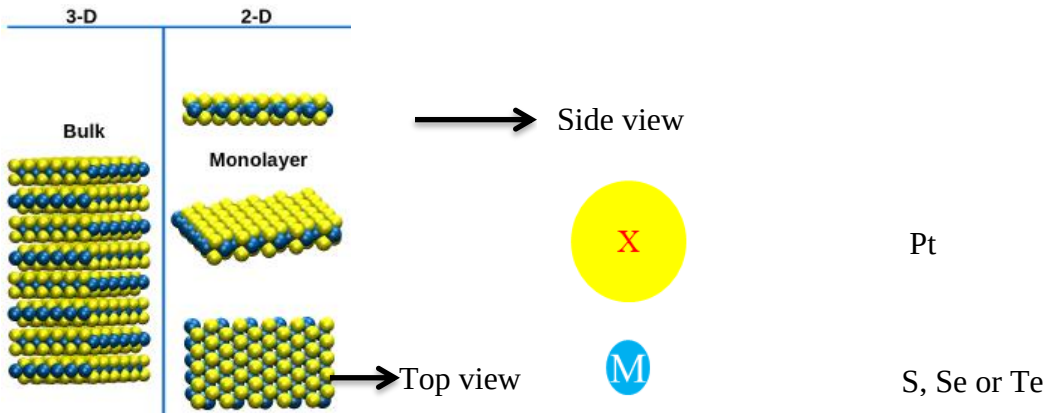

Figure 1.1: Polymorphs of transition metal dichalcogenide compounds.

1.1 Chalcogenides

Chalcogenides are chemical compounds that consist of at least one chalcogen anion and at least one more electropositive element. All group 6 elements of the periodic table are defined as chalcogens, however the term chalcogenide is more commonly reserved for sulfides, selenides, tellurides, and polonides rather than oxides. Oxygen and polonium are not commonly considered as chalcogenides due to their very different chemical behaviors. Chalcogenides are mostly semiconductors with a bandgap typically of 1–3 eV [11], depending on composition.

TMDs monolayers are atomically thin semiconductors of the type MX_2, with M being a transition metal atom (Mo, W, Pt, etc.) and X a chalcogen atom (S, Se, Te, etc). One layer of M atoms is sandwiched between two layers of X atoms. Group 4-7 transition elements TMDs have layered structures while those from group 8-10 are non-layered.

The thickness of the layers ranges between 6-7 Å [12]. They exhibit a wide range of electrical properties, depending on polytype and the number of transition metal d-electrons. TMDs monolayers have properties that are distinctly different from those of the semimetal graphene. They have bandgaps in the near-infrared to the visible region, in contrast to the zero bandgap of graphene. The discovery of graphene highlights how new physical properties emerge as a bulk crystal is thinned down to monolayers. TMDs monolayers such as MoS_2, WS_2, $MoSe_2$, WSe_2, $MoTe_2$ have been shown to possess direct bandgaps, a property well suited for photonics and optoelectronics applications. Single layers of MoS_2 have a large intrinsic bandgap of 1.8 eV, with previously reported mobilities in the 0.5-3 $cm^2\ V^{-1}\ s^{-1}$ [13] range being too low for practical devices. However it is relatively easy to fabricate complex structures from them to increase their mobilities [14].

1.2 Layered transition metal dichalcogenides

1.2.1 Crystal Structure and composition

In the layered TMDs the metal-chalcogen covalent bonding within the layers is very strong, whilst that between the layers is much weaker (van der Waals interactions). Due to this weak interlayer bonding, layers slides over each other upon application of shear stress, causing low friction [15]. Structurally TMDs (MoS_2, $MoSe_2$, WS_2, and WSe_2) crystallize in hexagonal layered configuration, in which a plane of metallic atoms (Mo or W) are bonded and sandwiched between two chalcogen (S or Se) planes, to form a slab, (X-M-X). Repeated stacking of these slabs in the c-axis direction gives rise to the hexagonal structure as shown in Figures 1.1 and 1.2.

Semiconducting TMDs have a variety of polymorphs depending on atomic arrangement of chalcogen atoms. By fluctuating the stacking sequence of consecutive X-M-X layers sandwiching along the hexagonal c-axis, different polytypes, 1T, 2H, and 3R, can be attained. In the abbreviated notation of polytypes, the integer indicates the number of X-M-X layers per unit cell along the c-axis and the letters T, H, and R

represent trigonal, hexagonal, and rhombohedral symmetries, respectively [16][17]. The 1T phase exhibits ABC sequence due to symmetry. The 2H phase exhibit ABA BAB stacking sequence whereby the chalcogen atoms overlap along the z-axis with the transition metal atoms of the adjacent layer and the 3R structure exhibits BCB, CAC ABA stacking sequence in the unit cell where the metal and chalcogen atoms are shifted.

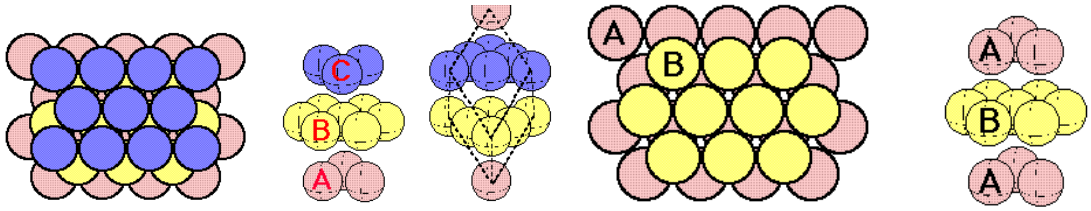

Figure 1.2: Stacking sequence for cubic close packing and hexagonal close packing.

Monolayer TMDs exhibit only two polymorphs, the trigonal prismatic and octahedral phases. The former belongs to the D_{3h} point group whereas the latter belongs to the D_{3d} group. Under ambient conditions most of the TMDs crystallize to $2H_c$ structure as shown in the Figure 1.3 below [18].

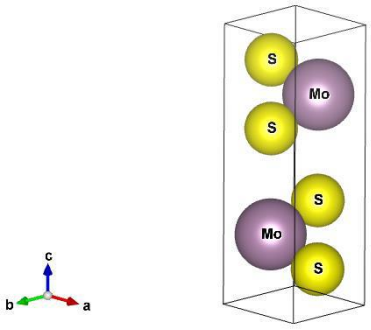

Figure 1.3: Atomic arrangements in MoS_2 - $2H_c$ type unit cell.

1.2.2 Electronic and optical properties

Layered TMDs materials exhibit interesting intrinsic electronic properties due to the highly anisotropic nature of their structures. The electronic structures of 2-D TMDs are largely determined by their crystal structures. Even though structurally TMDs

resemble graphene, MX_2 compounds have three atomic layers and exhibit finite bandgaps, making them promising materials for catalysis, energy storage, sensing and electronic devices such as field-effect transistors and logic circuits. In contrast to graphene or silicon where the electronic properties are based on hybridization of the *s* and *p* orbitals, the electronic structure of TMDs depends on the filling of *d* orbitals of the transition metals. When the *d* orbitals are partially filled, the TMDs exhibit a metallic behavior, whereas when they are fully occupied they have a semiconducting character.

The optical properties of materials are largely determined by their electronic band structure, screening and are dominated by excitonic transitions instead of band-to-band transitions [19][20][21]. The optical spectra are evaluated to understand the visible-light absorption ability of the TMDs heterostructures.

1.2.3 Thermal properties

In addition to their superior optical, electrical, and mechanical properties, TMDs thermal transport properties have also attracted attention progressively due to the central roles in various applications, such as heat dissipation, photonics and thermoelectric devices. Thermal transport properties of single layer TMDs, MX_2 were investigated systematically, by solving the Boltzmann transport equation based on first-principle calculations. In most MX_2 structures, thermal conductivities decrease with the increasing mass of either atom M or X [22]. Conversely, the thermal conductivities of TMDs sulfides and selenides increase as M changes from Cr to Mo to W, which contradicts our traditional understanding. The abnormal trend originates from the rapid increase of phonon relaxation time. Fundamental transport mechanisms were analyzed by the heat capacity, phonon group velocity, phonon relaxation time and phonon dispersion.

1.2.4 Dissertation Outline

The focus of this study is on recent progress in electronic, opto-electronic, electrochemical and thermo-dynamical properties of newly studied TMDs. Chapter two provides detailed literature review of TMDs. The theoretical background of DFT and its approximations in determining the structural, dynamical, electronic, optical and thermal properties of PtS_2, $PtSe_2$, $PtTe_2$ compounds is discussed in chapter three. Computational details are discussed in chapter four. The penultimate chapter provides results and discussion on the TMDs under study with the conclusions and future plan of action discussed in the last chapter of the dissertation.

All computations during this study were done using the VASP code which is based on the DFT and solves the Kohn-Sham equations using the projector augmented wave (PAW) method. The method is a generalization of the pseudopotential and linear augmented-plane-wave methods, allowing density functional theory calculations to be performed with better computational accuracy and efficiency. The first stage is a DFT calculation which will enable us to obtain the electronic structures of the systems which will be used as input for the second stage, the GW calculation. The third stage will be the Bethe Salpeter calculation where the optical properties will be determined based on the GW calculation input data. Lastly the thermal transport properties will be computed by means of the Boltzmann transport equation (BTE).

2. Review of TMDs

TMDs materials as discussed before have attracted significant attention because of their unique electronic and photonic properties which provide a unique opportunity to build up high quality and atomically sharp heterostructures. The integration of TMDs heterostructures into the semiconductor industry is presently hindered by limited options in reliable production methods. Most of the properties and device designs which have been studied are mainly based on the exfoliation methods of bulk TMDs crystals. These methods are commonly more difficult to consider for large scale integration processes and hence, continued developments of different fabrication strategies are essential for further advancements in this area [9]. Through synthesization, new covalent chemical bonds appear and due to these covalent bonds the materials show higher resistance against corrosion. This innovative property in itself makes novel applications, such as photo-electrochemical energy conversion electrode possible [23].

The field of 2-D materials is an ever-expanding research area, and the search for other 2-D materials beyond graphene is not just limited to TMDs [24] for possible applications, which include touch screens for liquid crystal displays (LCD) or organic light-emitting diode displays (OLED), transistors, computer chips, water filters, solar cells and many more [25][26]. New 2-D materials such as silicene and phosphorene are strong contenders in the rapidly emerging realms of 2-D materials. Figure 2.1 is an illustration of the transition metals and chalcogen elements which are building blocks of TMDs. A summary of common TMDs and their experimental bandgaps is given in Table 2.2.1.

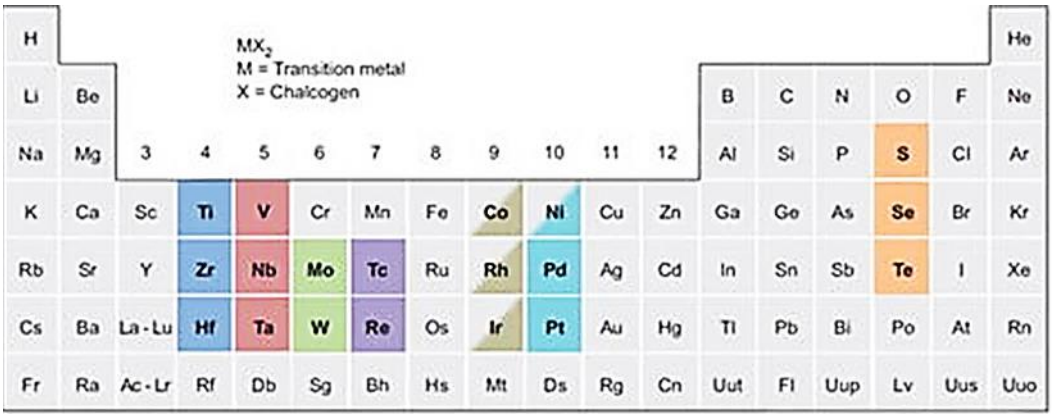

Figure 2.1: The transition metals and three chalcogen elements which are the building blocks of the 40 different TMDs.

Bandgap (eV)		Mo	W	Ti	Zr	Hf	V	Nb	Ta	Ni	Pd	Pt
S	monolayer	1.8-2.1	1.8-2.1	~0.65	~1.2	~1.3	~1.1	metal	metal	~0.6	~1.2	~1.9
	Bulk	1.0-1.3	1.3-1.4	~0.3	~1.6	~1.6	metal	metal	metal	~0.3	~1.1	~1.8
Se	monolayer	1.4-1.7	1.5-1.7	~0.51	~0.7	~0.7	metal	metal	metal	~0.12	~1.1	~1.5
	Bulk	1.1-1.4	1.2-1.5	metal	~0.8	~0.6	metal	metal	metal	metal	~1.3	~1.4
Te	monolayer	1.1-1.3	~1.03	~0.1	~0.4	~0.3	metal	metal	metal	metal	~0.3	~0.8
	Bulk	1.0-1.2	metal	metal	metal	metal	metal	metal	metal	metal	~0.2	~0.8

Table 2.2.1: The summary of common TMDs and their experimental bandgaps [10].

TMDs materials indirect bandgap in their bulk structure decreases as the atomic number of the chalcogen element increases (i.e., X = S, Se, Te) [27] and increases from bulk to monolayer limit. Diverse electronic properties can also be achieved by choosing the appropriate combinations of the M and X elements. The bandgaps of group VI monolayer TMDs are in the 1–2 eV range [28], ideal for optoelectronic applications [29]. Indirect optical bandgap materials reduce their efficiency in photovoltaic applications because photons with energy close to the bandgap can only be absorbed in phonon-assisted processes. They require surface plasmons in metallic nanoparticles embedded in a solar cell to increase the efficiency [30][31] leading to costly fabrication of large area materials.

The TMDs monolayer crystal structure has no inversion center, which allows to access a new degree of freedom of charge carriers, namely the k-valley index, and to open up a new field of physics namely valleytronics. These degrees of freedom are the real electron spin, the layer pseudospin, and the valley pseudospin. The strong spin-orbit coupling in TMDs monolayers leads to a spin-orbit splitting of hundreds meV in the valence band and a few meV in the conduction band, which allows control of the electron spin by tuning the excitation laser photon energy and handedness [32].

Thermal transport properties of TMDs display a substantial size effect and by considering the effects of boundary scattering and geometric sizes calculation results agrees with experimental results [33]. Zhang *et al*. [34] and Liu *et al*. [34] reported that their measured thermal conductivities of MoS_2 were approximately 85 $Wm^{-1}K^{-1}$, with a sample width size $d \approx 5$ μm and length $L \approx 15$ μm. Sahoo *et al*. [35] reported that the thermal conductivity of MoS_2 with size $d \approx 4$ μm and $L \approx 10$ μm as 52 $Wm^{-1}K^{-1}$. While Yan *et al*. [36] demonstrated that MoS_2 with a smaller circle sample (≈ 1.2 μm) had a much smaller value of 34.5 $Wm^{-1}K^{-1}$. The rare and rich thermal properties of TMDs materials can lay a solid foundation for understanding new phonon transport physics and potentially lead to novel applications in various emerging fields.

2.1 Transition metal dichalcogenides

2.1.1 Platinum disulfide (PtS_2)

PtS_2 can be made by precipitation in water solution of Pt(IV) treated with hydrogen selenide, or by heating platinum tetrachloride with elemental selenium. The compound assumes the cadmium iodide structure, being composed of sheets of octahedral Pt and pyramidal sulfide centers. Single crystals are grown by chemical vapor transport using phosphorus as the transport agent [37]**.** PtS_2 has an approximated bandgap of 0.95 eV and is able to reach high Pt oxidation states and has an advantage over Mo and W sulfides due to the fact that it contains a cation which is a noble metal [38].

PtS_2 properties have a very strong layer-dependence as a result of the hybridization of the p_z orbital of interlayer S atoms in PtS_2. This strong hybridization also leads to the interlayer shear and breathing vibrations nearly being isotropic. Therefore the need to establish fundamental understandings of the d-electron count on the interlayer interactions and layer-dependent properties of the compounds [39].

2.1.2 Platinum diselenide ($PtSe_2$)

Minozzi was the first in 1909 to report the synthesising of platinum diselenide from its elements. Platinum diselenide can be formed through heating of thin foils of platinum in selenium vapour at 400 °C. A platinum 111 surface exposed to selenium vapour at 270 °C forms a monolayer of $PtSe_2$ [40]. Besides these selenization methods, platinum diselenide can also form crystals in the cadmium iodide structure which is a prototype which crystal structures and many other compounds can be considered to be based on. The material forms layers with a "1T" structure and has a trigonal structure [41].
$PtSe_2$ is nonmagnetic. However, it is predicted to become ferromagnetic when there are approximately 10% platinum vacancies and when put under 5% strain [37]. Theoretical calculations suggested a transition from semimetal to semiconductor with reduced $PtSe_2$ thickness. It was shown experimentally by Wang *et al*. [40][42] that monolayer $PtSe_2$ has a bandgap of approximately 1.2 eV and exhibits helical spin texture with spin-layer locking induced by the local dipole field induced R-2 Rashba effect.

2.1.3 Platinum ditelluride ($PtTe_2$)

Tellurides of all platinum metals have been synthesized and characterized through x-ray and optical methods. Roessler in 1897 [9]. prepared platinum ditelluride by heating platinum with an excess of tellurium in an open furnace. In 1933, Wcihler *et al*. [43] likewise prepared and analyzed the compound an in 1929 Thomassen [43] synthesized

the material from the elements and determined its structure. Crystal of platinum ditelluride can be grown when the charges of platinum, sulfur, phosphorus and tellurium in the mole ratio of 1:3:1:2 are held at 875°C and the growth zone is cooled to 690°C [18]. Adding chlorine to a pressure of 75-100 torr enhances the transport. $PtTe_2$ crystallizes in the CdI_2-type trigonal (1T) structure with, $P\bar{3}m1$ space group and is a metal with a complex Fermi surface.

3 Theoretical Background

Over the past decades or more all sciences have seen an explosion in the use of computer simulations to model materials. Computational methods now stand alongside theoretical and experimental methods in value [44]. Most solid-state applications make use of Density Functional Theory (DFT). However, although the theory is well established, it fails to account for certain components particularly the exchange and correlation terms. Thus, approximations are required to improve the accuracy of the results. Hence, methods such as the Kohn-Sham equations, total energy functionals, exchange and correlation functionals, many-body perturbation theory, GW approximation and Bethe-Salpeter equation (BSE) will form an integral part of this study. Optical properties are determined from the BSE approximation. Thermal properties of TMDs are also determined through the Boltzmann transport equation combined with first-principles methods [45][46].

3.1 Density functional theory (DFT)

DFT is used in modelling in physics, chemistry and materials science to investigate the electronic structure, i.e. principally the ground state of many-body systems in atoms, molecules, and condensed phases. It is a formulation where formally, the ground state density is the controlling variable of all properties of a system and all physical properties can formally be determined from the ground state density [47]. The Kohn-Sham formulation is used in DFT which gives us information on the ground state density and energy of a system. These two quantities will be exact if the correct exchange-correlation functionals are used, however approximations to the exchange-correlation functionals have to be used. Computational investigation through simulating properties of their structural, electronic, optical and thermal properties through atomic scale materials modelling will then be used to estimate the performance

of materials under study as well as to explore and gain new insights into the latest technology.

The core spirit of DFT is to substitute the complicated and thus hard-to-compute many-electron wavefunction. Hohenberg and Kohn showed in their first theorem that the ground state properties of a many-electron system are uniquely determined by an electron density [48]. The idea is to replace the physical system of interacting electrons with a fictitious system (the Kohn-Sham system) of non-interacting electrons. These two systems have the same ground state electron density [49]. Then the energy of the system is a functional of the electron density and the goal now becomes to find the value of the functional and approximations are therefore required. The wavefunction of any state can thus be determined by solving the Schrödinger equation. The time-independent Schrödinger equation takes the following form:

$$H\Psi = E\Psi, \tag{3.1.1}$$

where H is the Hamiltonian operator, and E and Ψ represent the energy eigenvalue and wavefunction respectively. For a single electron problem, the equation takes the form:

$$\left[-\frac{\hbar^2}{2m}\nabla^2 + V(\vec{\boldsymbol{r}})\right]\Psi(\vec{\boldsymbol{r}}) = E\Psi(\vec{\boldsymbol{r}}). \tag{3.1.2}$$

It is too cumbersome and expensive to solve Eq (3.1.2) directly for a many body problem (more than one electron) because of the high dimensionality, it depends on the position of every electron in the system. The equation for the many-body system excluding spin dependency takes the form:

$$\left[\sum_i^N \left(-\frac{\hbar^2}{2m}\nabla^2 + V(\vec{\boldsymbol{r}})\right) + \sum_{i<j} U(\vec{\boldsymbol{r_i}}, \vec{\boldsymbol{r_j}})\right]\Psi(\vec{\boldsymbol{r_1}}, \vec{\boldsymbol{r_2}}, \dots, \vec{\boldsymbol{r_N}}) = E\Psi(\vec{\boldsymbol{r_1}}, \vec{\boldsymbol{r_2}}, \dots, \vec{\boldsymbol{r_N}}). \tag{3.1.3}$$

Where N is the number of electrons and $U(\vec{r}_i, \vec{r}_j)$ represents the electron-electron interactions, $\boldsymbol{r_i}$ and $\boldsymbol{r_j}$ are the coordinates of electrons i and j.

Therefore, it is imperative to reduce the computational challenges of the solution of the Schrödinger equation. The electron density $n(\vec{r})$, can be treated as the fundamental unknown in a many-electron system. Since $n(\vec{r})$ is a function which only depends on three spatial coordinates, numerical simulations of large molecules or even solids become possible. Subsequently our system only depends on the potential $V(\vec{r})$, therefore specifying $V(\vec{r})$ and substituting into the Schrödinger equation enables us to solve the equation for the wavefunction Ψ. Observables such as the particle density are then calculated using the calculated wavefunction. The quantum mechanical approach to equation (3.1.1) can be summarized as shown in (3.1.4) below.

$$V(\vec{r}) \overset{SE}{\Rightarrow} \Psi((\vec{r}_1, \vec{r}_2, \dots, \vec{r}_N) \xrightarrow{\langle\Psi|\dots|\Psi\rangle} observables \qquad (3.1.4)$$

One of the observables calculated in this way is the particle density expressed as:

$$n(\vec{r}_i) = N \int d^3\vec{r}_2 \int d^3\vec{r}_3 \dots \int d^3\vec{r}_N \, \Psi^*(\vec{r}_1, \vec{r}_2, \dots, \vec{r}_N)\Psi(\vec{r}_1, \vec{r}_2, \dots, \vec{r}_N), \quad (3.1.5)$$

$n(\vec{r}_i)$ determines the probability of finding any of the N electrons within volume element, $d\vec{r}$. Expressing potential of $V(\vec{r})$, in terms of electron density gives us:

$$\hat{V} = \int d^3\vec{r} V(\vec{r})\hat{n}(\vec{r}_i). \qquad (3.1.6)$$

The expectation value of the potential can also be known explicitly in terms of the density $n(\vec{r})$. All the properties of a system defined by the potential $V(\vec{r})$, are determined by the ground state density. The density functional approach can be summarized by the following sequence:

$$n(\vec{r}) \Rightarrow \Psi((\vec{r}_1, \vec{r}_2, \dots, \vec{r}_N) \Rightarrow V(\vec{r}). \qquad (3.1.7)$$

Hence the knowledge of $n(\vec{\boldsymbol{r}})$ implies that the knowledge of the wavefunction, potential and all other observables can be obtained [49][50][51][52].

3.2 Hohenberg-Kohn theorem

The Hohenberg-Kohn theorem states that the ground state density $n(\vec{\boldsymbol{r}})$ of a system of interacting electrons in an external potential $V_{ext}(\vec{\boldsymbol{r}})$ uniquely determines the total energy of the system [53].

The ground state total energy is a functional of the electron density, $n(\vec{\boldsymbol{r}})$, that is:

$$E = E[n]. \tag{3.2.1}$$

An assumption of nondegenerate ground state is made even though the proof can be extended to degenerate ground states. The external potential V_{ext}, distinctively determines the ground state wavefunction Ψ, as a solution of the Schrodinger equation. Thus, the electron density $n(\boldsymbol{r})$, can then be calculated by:

$$n(\boldsymbol{r}) = n[V_{ext}(\boldsymbol{r})]. \tag{3.2.2}$$

To prove that there is only one function $V_{ext}(\boldsymbol{r})$, which yields $n(\boldsymbol{r})$, *Reductio ad absurdum* (proof by contradiction) is applied. If we assume there is another potential $V'_{ext}(\boldsymbol{r})$, that yields the same electron density $n(\boldsymbol{r})$, denoting the ground states energies and Hamiltonians associated with Ψ and Ψ' by E, E', H and H' respectively we can denote the following expressions:

$$H = T + U_{el} + V_{ext} \Rightarrow H\Psi = E\Psi, \tag{3.2.3}$$

and

$$H' = T + U_{el} + V'_{ext} \Rightarrow H'\Psi' = E'\Psi', \tag{3.2.4}$$

According to the Rayleigh-Ritz's variation principle, since we are assuming that E' is the ground state energy we obtain,

$$E' = \langle \Psi' | H' | \Psi' \rangle < \langle \Psi | H' | \Psi \rangle, \tag{3.2.5}$$

Consequently,

$$\langle \Psi | V_{ext} | \Psi \rangle = \sum_{i=1}^{N} \frac{1}{N} dr_i \, V_{ext}(\boldsymbol{r_i}) n(\boldsymbol{r_i}) = \int dr V_{ext}(\boldsymbol{r}) \, n(\boldsymbol{r}), \tag{3.2.6}$$

Therefore:

$$\langle \Psi | H' | \Psi \rangle = \langle \Psi | H - V_{ext}(\boldsymbol{r}) + V'_{ext} | \Psi \rangle = E + \int dr \, n(r) [V'_{ext}(\boldsymbol{r}) - V_{ext}(\boldsymbol{r}), \tag{3.2.7}$$

and,

$$E' < E + \int d\boldsymbol{r} n(\boldsymbol{r}) [V'_{ext}(r) - V_{ext}(\boldsymbol{r})]. \tag{3.2.8}$$

Starting with E as in equation (3.2.8), we get,

$$E = \langle \Psi | H | \Psi \rangle < \langle \Psi' | H | \Psi' \rangle = E' + \int d\boldsymbol{r} n'(\boldsymbol{r}) [V_{ext}(r) - V'_{ext}(\boldsymbol{r})], \tag{3.2.9}$$

Through the assumption that $n(\boldsymbol{r}) = n'(\boldsymbol{r})$, therefore:

$$E < E' + \int d\boldsymbol{r} n(\boldsymbol{r}) [V_{ext}(\boldsymbol{r}) - V'_{ext}(\boldsymbol{r})], \tag{3.2.10}$$

By adding the two above inequalities, (3.2.8) and (3.2.10) we get:

$$E' + E < E + E'. \tag{3.2.11}$$

which is a contradiction meaning that there can only be one $V_{ext}(\boldsymbol{r})$ yielding $n(\boldsymbol{r})$. That is, there is a one-to-one mapping between the ground state density and the external potential. Thus the ground state electron density is sufficient to construct the full Hamilton operator and hence to calculate, in principle all ground state properties of the system without the knowledge of the many electron wavefunction **[**52][55]**.**

3.3 Kohn-Sham (K-S) equations

Theoretically it should be possible to calculate all observables since the Hohenberg-Kohn theorem assures that they are all functionals of the ground state electron density. Practically one does not know how this is done clearly. The Kohn-Sham equations can thus be used to solve the challenge. This is done by replacing the original many-body problem by an auxiliary independent particle problem. This ansatz has made possible approximate formulations that have been remarkably successful. The Kohn-Sham self-consistent approach replaces the complicated many-body system with an auxiliary system that can be solved more easily. The ansatz of Kohn and Sham makes use of the following two assumptions:

- The ground state density of an original interacting system is the same as that of a fictitious system of non-interacting particles (typically electrons).
- The single particle Hamiltonian for one of these non-interacting particles is chosen to consist of the usual kinetic energy operator and an effective local potential V_{eff}(r), acting on an electron at a point, r in the auxiliary system [56].

The only properties that are guaranteed to be correct through the Kohn-Sham approach are the density and energy.

Kohn-Sham DFT gives a set of variational equations that are solved self consistently and the total energy of a system is expressed as a functional of the charge density as shown below in equation (3.3.1) [57].

$$E[n(\vec{\boldsymbol{r}})] = T_s[n(\vec{\boldsymbol{r}})] + \int d\vec{\boldsymbol{r}}\, V_{ext}(\vec{r})n(\vec{\boldsymbol{r}}) + E_H[n(\vec{\boldsymbol{r}})] + E_{xc}[n(\vec{\boldsymbol{r}})]. \qquad (3.3.1)$$

where T_s is the K-S kinetic energy, V_{ext}, E_H and E_{xc} represents the sum of the external potential acting on the interacting system, Hartree and exchange-correlation energies respectively. The K-S kinetic energy can thus be expressed by re-introducing the Kohn-Sham (independent particle) wavefunction Ψ, as:

$$T_s[n(\vec{r})] = \sum_{i=1}^{N} \int d\vec{r} \Psi_i^*(\vec{r}) \left(-\frac{\hbar^2}{2m}\nabla^2\right) \Psi_i(\vec{r}), \quad (3.3.2)$$

and Hartree energy as:

$$E_H[n(\vec{\boldsymbol{r}})] = \frac{e^2}{2} \int d\vec{\boldsymbol{r}} \int d\vec{\boldsymbol{r}}' \frac{n(\vec{\boldsymbol{r}})n(\vec{\boldsymbol{r}}')}{|\vec{\boldsymbol{r}}-\vec{\boldsymbol{r}}'|}, \quad (3.3.3)$$

The K-S equations are created by varying the total energy expression with respect to a set of orbitals to yield the Kohn-Sham potential as:

$$V_{eff}(\vec{\boldsymbol{r}}) = V_{ext}(\vec{\boldsymbol{r}}) + e^2 \int \frac{n(\vec{\boldsymbol{r}}')}{|\vec{\boldsymbol{r}}-\vec{\boldsymbol{r}}'|} d\vec{\boldsymbol{r}}' + \frac{\delta E_{xc}[n(\vec{\boldsymbol{r}})]}{\delta n(\vec{\boldsymbol{r}})}. \quad (3.3.4)$$

Where V_{XC} is the exchange correlation potential

$$V_{xc}(\vec{\boldsymbol{r}}) = \frac{\delta E_{xc}[n(\vec{\boldsymbol{r}})]}{\delta n(\vec{\boldsymbol{r}})}, \quad (3.3.5)$$

Substituting into equation (3.1.1) gives:

$$\left[-\frac{\hbar^2}{2m}\nabla^2 + V_{eff}(\vec{\boldsymbol{r}})\right] \Psi_i(\vec{\boldsymbol{r}}) = E\Psi_i(\vec{\boldsymbol{r}}). \quad (3.3.6)$$

$$n(\vec{\boldsymbol{r}}) = \sum_i^N |\Psi_i(\vec{\boldsymbol{r}})|^2. \quad (3.3.7)$$

The form of the exchange-correlation E_{xc}, energy functional is not known. Therefore, approximations are made so that DFT can be used for physical systems [58]. The above equations provide a theoretically exact method to compute the ground-state energy of an interacting system, by giving the form of E_{xc}. Unfortunately, the form of the E_{xc} is unknown and its exact value has been calculated for only a few very simple systems, such as H and He and therefore has to be approximated.

A self-consistent iterative procedure would start from an initial electron density that can be used to calculate the Kohn-Sham potential. Then, through solution of equation (3.3.6), and use of the relation in equation (3.3.7) we can obtain a new electron density. If the initial and new densities are identical, then the ground state density has been found. Otherwise one must select a new trial density through minimization of the total energy and continue to repeat the iterative procedure.

3.4 Density Functional Theory methods

3.4.1 Making DFT practical: Approximations

As mentioned earlier the major problem with DFT is that the exact functionals for exchange and correlation are not known except for the free electron gas. However, approximations exist which allows the calculation of certain physical quantities to be done quite accurately. It is vitally important to search the literature for calculations on similar materials and properties. Three different approximations will be discussed under this study, namely the Local density approximation (LDA), Generalized gradient approximation (GGA) and the Hybrid functionals [59].

3.4.2 Local Density Approximation (LDA)

The LDA is determined solely based on the properties of the electron density with an assumption that, for a molecule with many electrons in a gaseous state, the density is uniform throughout the molecule. The LDA is mostly accurate and generally gives very good results for systems with slowly varying charge densities.

$$E_{xc}^{LDA} = \int \in_{xc} [n(\boldsymbol{r})] n(\boldsymbol{r}) d\boldsymbol{r}, \tag{3.4.1}$$

where $\in_{xc}$ is the exchange-correlation energy of a homogeneous electron gas of density *n.*

The exchange-correlation potential corresponding to E_{xc}^{LDA} is given by:

$$v_{xc}^{LDA}(\boldsymbol{r}) = \frac{\delta E_{xc}^{LDA}}{\delta n(\boldsymbol{r})} = \in_{xc} [n(\boldsymbol{r})] + n(\boldsymbol{r}) \frac{\partial_{xc}[n(\boldsymbol{r})]}{\partial n(\boldsymbol{r})}. \tag{3.4.2}$$

The exchange-correlation energy is then divided into exchange and correlation components and the exchange component is elementary, leading to different numerous approximations for the correlation component [60][61].

$$\in_{xc} = \in_x + \in_c . \tag{3.4.3}$$

Expression for exchange can be solved using:

$$\in_x = C \int n^{\frac{4}{3}}(\boldsymbol{r}) d\boldsymbol{r} . \tag{3.4.4}$$

3.4.3 Generalized Gradient Approximation (GGA)

The success of LDA led to more improved approximation in the form of GGA. Any real system has a spatial varying charge density and GGA includes information on the rate of variation in the functional as shown below.

$$E_{xc}^{GGA} = \int d^3 f[n(\boldsymbol{r})], \nabla n(\boldsymbol{r}). \tag{3.4.5}$$

Current common GGA's and LDA seem to have reliable results for all types of bonds and fail for van der Waals interactions. Numerous other GGA functionals have been developed to describe these weak interactions and can be classified into two types: functionals that contain empirical parameters whose values have been fitted to reproduce experiments or more accurate calculations, such as B88 and LYP. The second type corresponds to functionals with no empirically determined parameters, such as PBE, B86, PW91 [62].

3.4.4 Hybrid functionals

These are a class of approximations to the exchange-correlation energy functional in DFT that incorporate a portion of exact exchange from Hartree-Fock theory with exchange and correlation from other *ab initio*. The exact exchange is mixed with DFT approximations, resulting in improved accuracy and corrects qualitative features. One

of the most commonly used versions is B3LYP (Becke, 3-parameter, Lee-Yang-Parr) [63]. B3LYP functional employs three parameters a_0, a_C, a_X to control the mixing of the Hartree-Fock (HF) exchange and density functional exchange and correlation. Given by the following expression:

$$E_{xc}^{B3LYP} = E_{xc}^{LDA} + a_0(E_x^{HF} - E_x^{LDA}) + a_x(E_x^{GGA} - E_x^{LDA}) + a_c(E_c^{GGA} - E_c^{LDA}). \quad (3.4.6)$$

Where the empirical values a_0 = 0.2, a_x = 0.72, and a_c = 0.81. E_x^{GGA} and E_c^{GGA} are the generalized gradient approximations: the Becke 88 exchange functional and the correlation functional of LYP for B3LYP, and E_c^{LDA} is the Vosko, Wilk, and Nusair (VWN*)* local-density approximation to the correlation functional. Other hybrids available are B1PW91, B1LYP, B1B95, mPW1PW91 and PBE1PBE [64].

3.5 Exchange-correlation energy functionals

Every component of Kohn-Sham DFT energy can be computed exactly except for the exchange-correlation component. The total energy of for example, a closed shell system is given by the following expression:

$$E[n] = T_s[n] + V[n] + U[n] + E_{xc}[n], \quad (3.5.1)$$

where $T_s[\mathrm{n}]$, $V[\mathrm{n}]$, and $U[\mathrm{n}]$ are the kinetic, nuclear-electron attraction (Coulombic) and electron-electron (Coulomb) interaction energy terms respectively. Substituting into equation (3.5.1) gives:

$$E[n] = -\frac{\hbar^2}{2m}\sum_i^N \int d^3\boldsymbol{r}\phi_i^*(r)\,\nabla^2\phi_i(\boldsymbol{r}) + \int d\boldsymbol{r}V_{ext}(\boldsymbol{r})n(\boldsymbol{r}) + \frac{1}{2}\int d\boldsymbol{r}\int d\boldsymbol{r}'\,\frac{n(\boldsymbol{r})n(\boldsymbol{r}')}{|\boldsymbol{r}-\boldsymbol{r}'|} + E_{xc}[n]\,. \quad (3.5.2)$$

The 1st term on the right-hand side is expressed in terms of the single-particle orbitals $\phi_i(\boldsymbol{r})$, of a non-interacting system with density *n*, and it depends on a full set of occupied orbitals. The last term of equation (3.5.1), $E_{xc}[n]$ is the exchange correlation energy which incorporates everything else that is not exactly defined. The exchange-correlation energy E_{xc}, can be split into two components as illustrated below in the following form:

$$E_{xc}[n] = E_x[n] + E_c[n] \,, \tag{3.5.3}$$

where $E_x[n]$ is the exchange energy functional that is exactly defined and $E_c[n]$ is the correlation energy functional that will be approximated. The exchange-correlation energy can therefore be written as,

$$E_{xc}[n] = \frac{1}{2}\int\int n(\boldsymbol{r})\frac{n_{xc}(\boldsymbol{r},\boldsymbol{r'})}{|\boldsymbol{r}-\boldsymbol{r'}|}\, d\boldsymbol{r}d\boldsymbol{r'}. \tag{3.5.4}$$

Is the Coulombic interaction between an electron at position ***r***, and the value of its exchange-correlation hole n_{xc} ***(r, r')*** at ***r'***. Hole charge at ***r'*** is not static but depends on the current position of electron ***r***. The exchange term can be written explicitly in terms of the single-particle orbitals as,

$$E_x[\{\phi_i[n]\}] = \frac{q^2}{2}\sum_{jk}\int d^3\boldsymbol{r}\int d^3\boldsymbol{r'}\frac{\phi_j^*(r)\phi_k^*(\boldsymbol{r'})\phi_j(\boldsymbol{r'})\phi_k(\boldsymbol{r})}{|\boldsymbol{r}-\boldsymbol{r'}|}\,. \tag{3.5.5}$$

The exchange-correlation density n_{xc} ***(r,r')***, at ***r'*** can also be sub-divided into exchange and correlation parts as.

$$n_{xc}(\boldsymbol{r},\boldsymbol{r'}) = n_x(\boldsymbol{r},\boldsymbol{r'}) + n_c(\boldsymbol{r},\boldsymbol{r'}) \,, \tag{3.5.6}$$

Using equation (3.5.4) we can re-write the exchange and correlation functionals as:

$$E_x[n] = \frac{1}{2}\int\int n(\boldsymbol{r})\frac{n_x(\boldsymbol{r},\boldsymbol{r'})}{|\boldsymbol{r}-\boldsymbol{r'}|}\, d\boldsymbol{r}d\boldsymbol{r'}\,. \tag{3.5.7}$$

$$E_c[n] = \frac{1}{2}\int\int n(\boldsymbol{r})\frac{n_c(\boldsymbol{r},\boldsymbol{r}')}{|\boldsymbol{r}-\boldsymbol{r}'|}\,d\boldsymbol{r}d\boldsymbol{r}' \ . \qquad (3.5.8)$$

The correlation becomes the energy lowering obtained in a real system due to mutual avoidance of the interacting electrons. The correlation energy can thus be estimated since it constitutes a fraction of the total energy functional. However, it can have an important contribution to many systems of physical and chemical interest. Different methods used to explicitly calculate this component will be used during this study [65][66][67].

3.6 Van der Waals interactions (vdW)

In physical chemistry the term vdW comprises all probable forces between molecules such as between two permanent dipoles (Keesom force), a permanent dipole and a corresponding induced dipole (Debye force), and two induced dipoles (London dispersion force). In condensed matter, material physics, chemistry and biology, London dispersion forces are referred to as the vdW forces. They are weak forces but are crucial for cohesion of layered materials [68].

3.6.1 Extensions of (semi)local DFT methods

By construction, LDA and GGA disregard the long-range non-local correlations that give rise to the vdW forces but there are possibilities to add it in a pragmatic manner. Therefore, the need to search for an approximate E_{xc} functional that includes vdW forces. The exchange part alone can yield anything from severe over binding to severe over repulsion depending on the choice of the functional. This method of adding an inter-atomic potential to the total DFT energy has been projected in various forms, but the most prominent were introduced by Grimmer, Tkatchenko and Scheffler (TS) as

well as Becke-Johnson (BJ) [69]. The total energy of a system can be expressed in a way that incorporates the vdW interactions as shown below.

$$E_{DFT-disp} = E_{KS-DFT} + E_{disp}, \tag{3.6.1}$$

where $E_{DFT-disp}$ is the self-consistent Kohn-Sham energy and E_{disp} is the dispersion correction. In the DFT-D2 [70] method by Grimme, the potential is written as:

$$E_{disp} = -S_6 \sum_{i<j} \frac{C_6^{ij}}{r_{ij}^6} \frac{1}{1+e^{-d(r_{ij}/s_R R_{ij}-1)}}, \tag{3.6.2}$$

where $\boldsymbol{r_{ij}}$ is the distance between i and j atoms, S_6 is a fitted scaling parameter that is dependent on the DFT functional used, C_6^{ij} is a coefficient that defines the strength of inter atomic interaction. $R_{ij} = R_i + R_j$ combine the tabulated empirical vdW radii R_i, which are used with constants, d and s_R to determine the behaviour of the damping function.

DFT-D2 method is numerically efficient and produces accurate binding energies especially when combined with some of the double hybrid functionals instead of GGA. However, this method has some disadvantages such as lacking flexibility as well as electron distribution dependence. These disadvantages can be addressed by the DFT-D3, TS and BJ methods. The DFT-D3 method takes into account the chemical environment of each atom by assigning a coordination number [70].

In the DFT-D3 correction method the dispersion correction is,

$$E_{disp} = -\frac{1}{2}\sum_{i=1}^{N_{at}}\sum_{j=1}^{N_{at}} {\sum_L}' \left(f_{d,6}(r_{ij,L}) \frac{C_{6ij}}{r_{ij,L}^6} + f_{d,8}(r_{ij,L}) \frac{C_{8ij}}{r_{ij,L}^8} \right). \tag{3.6.3}$$

In the DFT-D3 correction method, unlike in the method DFT-D2, the dispersion coefficients C_{6ij}, are geometry-dependent as they are adjusted on the basis of local geometry (coordination number) around atoms i and j.

The expression for dispersion energy within the method of TS [71] is formally identical to that of the DFT-D2 method with the difference being that the dispersion coefficients and damping function are charge density dependent. The TS method is therefore able to take into account variations in vdW contributions of atoms due to their local chemical environment.

Polarizability (α) and dispersion coefficients of an atom in a molecule or a solid are calculated from their free-atomic values using the following relations [72] :

$$\alpha_i = v_i \alpha_i^{free}, \tag{3.6.4}$$

$$C_{6ii} = v_i^2 C_{6ii}^{free}, \tag{3.6.5}$$

v_i is the ratio of effective volume occupied by the atom in solid divided by the molecular environment to volume of free non-interacting atom.

The combination rule that describes the strength of the dipole-dipole dispersion interaction between different atomic species is given by:

$$C_{6ij} = \frac{C_{6ii} C_{6jj}}{\left[\frac{\alpha_j}{\alpha_i} C_{6ii} + \frac{\alpha_i}{\alpha_j} C_{6jj}\right]}. \tag{3.6.6}$$

The strength of atomic interactions within themselves is given by C_{6ii} and C_{6jj} whereas, C_{6ij} gives the interaction between the atoms i and j [73].

The optPBE [74][75] functional is one example of the vdW-DF approach which requires no external input but seeks to treat dispersion interactions directly by using the electron density. The optPBE seeks to overcome the problems of the original vdW-DF that produced too large molecular binding distances [76]. The exchange-correlation energy is given by:

$$E_{xc} = E_x^{GGA} + E_c^{LDA} + E_c^{nl}. \tag{3.6.7}$$

where ${E_x}^{GGA}$ and ${E_c}^{LDA}$ are the exchange and correlation energies for given GGA and LDA functionals respectively. Dispersion is included using nonlocal correlation energy E_c^{nl}, calculated in the form,

$$E_c^{nl} = \iint dr_1 dr_2 n(r_1)\varphi(r_1, r_2)n(r_2). \tag{3.6.8}$$

where, as before $n(\boldsymbol{r})$ is the electron density and φ is an integration kernel.

PBEsol [77] functional is intended to improve on PBE for equilibrium properties such as bond lengths and lattice parameters for solid state and surface systems. It is constructed on a gradient expansion of the exchange energy and a final fit of the exchange-correlation energy to that of surface jellium.

Heyd, Scuseria and Ernzerhof (HSE) [78] proposed to replace the long-range part of the semilocal density functional. This is equivalent to taking a semilocal functional and hybridizing the short-range part of the exchange as shown in equation (3.6.9) below.

$${E_{xc}}^{HSE06} = 0.25{E_x}^{HF,SR}(\omega) + 0.75{E_x}^{PBE,SR} + {E_X}^{PBE,LR} + {E_C}^{PBE}. \tag{3.6.9}$$

Where, ${E_x}^{HF,SR}$, ${E_x}^{PBE,SR}$ and ${E_X}^{PBE,LR}$ are the short-range Hartree-Fock exchange, short-range PBE exchange and long-range PBE exchange respectively. The mixing parameter for HSE06 is 25% and it improves the bandgaps in semiconductors [79].

The modified Becke-Johnson potential (mBJ) [80] has also been proven to improve the bandgap description. The MBJ potential is given by:

$${v_x}^{mBJ}(r) = c{v_x}^{BR} + (3c - 2)\frac{1}{\pi}\sqrt{\frac{5}{12}}\sqrt{\frac{2t(r)}{n(r)}}. \tag{3.6.10}$$

Where, c is a system-dependent parameter, with $c = 1$ corresponding to the Becke-Roussel (BR) potential ${v_x}^{BR}(r)$ which was originally proposed to mimic the Slater potential, the Coulomb potential corresponding to the exact exchange hole. With $t(r)$ representing the kinetic energy density [81][82].

3.7 Phonons

A phonon is a collective excitation of a set of atoms in condensed matter. When an atom in a crystal is displaced from its equilibrium position, the forces on all atoms in the crystal rise. Phonons determine the crystal temperature. Knowledge of phonon characteristics are required to describe mechanical, acoustic, dynamical, spectroscopic and thermodynamic properties of crystals at finite temperature [83]. First principles phonon calculations with a finite displacement method involve analysis of the forces associated with a systematic set of displacements providing a series of phonon frequencies [84]. In the supercell method, finite displacement calculations are carried out in the supercell. Calculation of harmonic force constants are conducted as follows:

$$\Phi_{ij}(M,N) = \frac{\partial^2 V}{\partial u_i(M)\partial u_j(N)} \cong -\frac{F_i(M)}{u_j(N)} \tag{3.7.1}$$

where V is the potential energy, $u_j(N)$ is the displacement of atom N and $F_i(M)$ is the force on atom M.

3.8 Many Body Pertubation Theory (MBPT)

DFT represents an independent and alternative approach to an inhomogeneous electron gas problem [85]. MBPT offers a useful framework for the calculation of electronic excitations (response to an external perturbation). The response of the material is essential for the interpretation of many experimental results or for the design of technological devices. These excitations probes into many real life problems ranging from the design of more efficient solar cells, defect creation in nuclear waste, deformation of molecules upon absorption of radiation in cancer research to photosynthesis [86]. In order to study electronic excitations spectrum of a solid, photoemission experiments are performed where photon with an energy $\hbar\omega$ are used

as projectiles to knock electrons out a solid. Measuring the kinetic energy of the photoemitted electrons along a certain direction *k*, and using the conservation of energy and momentum, the excitation spectrum *E(k)*, can be calculated using:

$$\hbar\omega = K.E + E(k) \tag{3.8.1}$$

The experiment then measures the excitation spectrum of the solid with the presence of a hole. An inverse photoemission experiment uses electrons as probes to measure the unoccupied density of states with an additional electron.

The difference in energy between the ground and excited states of an N particle system can be measured by measuring the energy of the photon absorbed by the system. This energy difference is called optical or neutral gap and is given by:

$$\Delta = E_{total}^{gs}(N) - E_{total}^{exc}(N) \tag{3.8.2}$$

where $E_{total}^{gs}(N)$ is the ground state energy and $E_{total}^{exc}(N)$ the excited state energy of an N-particle system. If ionization takes place during a photoemission experiment, the absorbed photon can gain enough energy to leave the system. The difference between the initial $E_{total}(N)$, and the escaped photon energy $E_{total}(N-1)$, can be used to determine the ionization potential by:

$$I = E_{total}(N-1) - E_{total}(N) \tag{3.8.3}$$

Electron affinity can also be determined from the inverse photoemission experiment as follows:

$$A = E_{total}(N) - E_{total}(N+1) \tag{3.8.4}$$

The difference between the ionization potential and electron affinity gives us the fundamental gap of the material which is also related to the chemical hardness and energy orbital difference of the system [87].

When dealing with interacting molecular orbitals, the two that interact are commonly the highest energy occupied molecular orbital (HOMO) of one molecule and the lowest energy unoccupied molecular orbital (LUMO) of the other molecule. These orbitals are the pair that lie closest in energy of any pair of orbitals in the two molecules, which allows them to interact most strongly. The difference in energy between these orbitals is the fundamental gap.

3.9 Green function

The Green's-function allows us to solve the problems of calculating excitation, ionization and ground state energies, transition matrix elements, absorption coefficients, and dynamical polarizabilities. Additionally, self-consistent perturbation theories can be formulated in terms of the Green's function [88].

Through photoemission experiments photons with an energy (ħω) can be used to eject electrons. The excitation spectrum *E(k)*, of the solid can be obtained through equation (3.8.1). According to Hedin and Lundqvist 1969 [89], for sudden approximation of the photoemitted or probing electron, the spectrum is directly related to the one-particle Green function defined as:

$$iG(x,x') = \langle N\left|T\left[\hat{\psi}(x)\hat{\psi}^{\dagger}(x')\right]\right|N\rangle \tag{3.9.1}$$

for $t > t'$ (electron), i.e. probability that an electron added at x' will propagate to x.

$$iG(x,x') = \langle N\left|\hat{\psi}(x)\hat{\psi}^{\dagger}(x')\right|N\rangle \tag{3.9.2}$$

for $t' > t$ (hole) , ie, probability that a hole created at x will propagate to x'.

$$iG(x,x') = \langle -N\left|\hat{\psi}(x)\hat{\psi}^{\dagger}(x')\right|N\rangle \tag{3.9.3}$$

where, $|N\rangle$ is the exact N-electron ground state, $\hat{\psi}$ is a field operator in the Heisenberg representation which annihilates an electron at $x = (\boldsymbol{r}, t)$ and t is the time ordering operator. Expressing the Heisenberg equation of motion using the field operator, $\hat{\psi}$:

$$i\frac{\partial\hat{\psi}(x)}{\partial t} = \left[\hat{\psi}(x), \hat{H}\right], \tag{3.9.4}$$

the Hamiltonian, $\hat{H}$ is given by,

$$\hat{H} = \int d^3r\hat{\psi}^\dagger(x)h_0(x)\hat{\psi}(x) + \frac{1}{2}\int d^3rd^3r'\hat{\psi}^\dagger(x)\hat{\psi}^\dagger(x')v(r-r'), \tag{3.9.5}$$

where $v(r-r')$ is the bare Coulomb interaction. The equation of motion for the Green function becomes:

$$\left[i\frac{\partial}{\partial t} - h_0(x)\right]G(x,x') - \int dx''M(x,x'')G(x'',x') = \delta(x-x'), \tag{3.9.6}$$

h_0 is the summation of the kinetic energy and local external potential. The Hartree potential plus self-energy operator, *M* is given by:

$$\int dx_1M(x,x_1)G(x_1,x') = -i\int d^3r_1v(r-r_1)\times$$
$$\langle N\left|T\left[\hat{\psi}^\dagger(r_1,t)\hat{\psi}(r_1,t)\hat{\psi}^\dagger(r,t)\hat{\psi}^\dagger(r',t')\right]\right|N\rangle. \tag{3.9.7}$$

3.10 Self-energy

Self-energy Σ, is the energy that a particle has as a result of changes that it itself causes in its environment. It represents the contribution to the particle's energy, or effective mass, due to interactions between the particle and its system. The perturbation theory starts from what is known in order to evaluate what is not known, with the hope that the difference between the two is small. Assuming that G_0 corresponds to the Hamiltonian h_0, all that is unknown is placed in:

$$\Sigma = G_0^{-1} - G^{-1}\,, \tag{3.10.1}$$

which is the definition of self-energy. Therefore,

$$\left[i\frac{\partial}{\partial t} - h_0\right] G - \int \Sigma G = 1. \tag{3.10.2}$$

will be compared with,

$$\left[i\frac{\partial}{\partial t} - h_0\right] G + i\int \mathrm{v} G_2 = 1. \tag{3.10.3}$$

Applying the trick due to Schwinger (1951) [90], a small external potential $U(3)$, is introduced that will be made equal to zero at the end. Variations of $G_1$with respect to *U* are then calculated. The self-energy,

$$\Sigma(1,2) = -i\int d3d4v(1^{\dagger},3)G(1,4)\frac{\delta G^{-1}(4,2)}{\delta U(3)}. \tag{3.10.4}$$

The vertex function is then expressed as:

$$\Gamma(1,2,3) = \frac{\delta G^{-1}(1,2)}{\delta U(3)}. \tag{3.10.5}$$

The Dyson equation becomes,

$$G^{-1}(1,2) = G_0^{-1}(1,2) - U(1)\delta(1,2) - \Sigma(1,2). \tag{3.10.6}$$

Through the Dyson equation we can therefore simplify using the analogy that the Green function G_0, corresponds to self-energy $\Sigma = 0$ obtaining:

$$G = G_0 + G_0\Sigma G. \tag{3.10.7}$$

The first term $G_0(1, 2)$ is a direct propagation from points 1 to 2 without exchange-correlation interaction. Σ contains all the possible exchange-correlation interactions with the system that an electron can have when moving from point 1 to 2. G_0 also corresponds to $H_0 = H^{Hartree} + V^{xc}$, hence equation (3.10.7) can be expressed as:

$$G = G_0 + G_0\Delta\Sigma G \tag{3.10.8}$$

where, $\Delta\Sigma = \Sigma - V^{xc}$ and V^{xc} represents some local and energy-independent exchange-correlation potential.

Multiplying equation (3.10.7) on the left by the inverse $G_0^{-1}$of the operator G_0 and on the right by G^{-1} yields equation (3.10.1) [91][92].

3.11 Polarization and response function

The ability of a material to form instantaneous dipoles is a measure of its polarizability. Polarizabilities determine the dynamical response of a bound system to external fields providing an understanding into a molecule's internal structure [93].

The macroscopic dielectric tensor couples the electric field in a material to an applied external field as shown below:

$$E = \epsilon^{-1} E_{ext}. \tag{3.11.1}$$

where ϵ is the dielectric tensor and E is the electric field. Total potential of a system can be expressed as sums of the external potential V_{ext}, that arises from perturbation caused by a photon and the induced potential V_{ind}. We can have two formulations:

$$V_{tot} = \epsilon^{-1} V_{ext}, \tag{3.11.2}$$

and

$$V_{tot} = V_{ext} + V_{ind}, \tag{3.11.3}$$

The induced potential produced by the induced change in the charge density ρ_{ind}, is given by:

$$\delta V_{ind} = v\delta\rho_{ind}, \tag{3.11.4}$$

where $v = \frac{4\pi e^2}{q^2}$ is the Coulomb kernel. From equation (3.10.2) and (3.10.3), the dielectric function can be expressed as:

$$\epsilon = \frac{\delta(V_{tot} - V_{ind})}{\delta V_{tot}}, \tag{3.11.5}$$

which can be simplified to:

$$\epsilon = 1 - \frac{v\delta\rho_{ind}}{\delta V_{tot}} \tag{3.11.6}$$

The inverse dielectric function can be also expressed as:

$$\epsilon^{-1} = 1 + \frac{v\delta\rho_{ind}}{\delta V_{ext}}, \tag{3.11.7}$$

In weak external fields,

$$\rho_{ind} = \chi V_{ext}, \tag{3.11.8}$$

where χ is the reducible polarizability and:

$$\rho_{ind} = PV_{tot}, \tag{3.11.9}$$

where P is the irreducible polarizability, which gives the change in the charge density due to a change in total field.

A relationship between the reducible polarizability and irreducible polarizability can therefore be established from the above equations which has a form of the Dyson equation as:

$$\epsilon^{-1} = 1 + v\chi. \tag{3.11.10}$$

$$\epsilon = 1 - vP. \tag{3.11.11}$$

$$\chi = P + Pv\chi. \tag{3.11.12}$$

Through equations (3.11.10) and (3.11.11) the dielectric function can be calculated if the response of the system to a change in the external or total potential is known [94].

3.12 Hedin's equations

In 1965 *Lars Hedin* [95] derived a closed set of equations for the propagator *G*, the proper self-energy Σ, the effective potential *W*, the polarization Π, and the dressed vertex Γ , the irreducible polarizability χ, and bare Coulomb potential V.

$$G(1,2) = G_0(1,2) + \int d34 G_0(1,3)\Sigma(3,4)G(4,2). \quad (3.12.1)$$

$$\Sigma(1,2) = i \int d(34) G(1,3)\mathrm{W}(1,4)\Gamma(4,2,3). \quad (3.12.2)$$

$$\Gamma(1,2,3) = \delta(1,2)\delta(1,3) + \int d(4567) \frac{\delta\Sigma(1,2)}{\delta G(4,5)} G(4,6)G(7,5)\Gamma(6,7,3). \quad (3.12.3)$$

$$W(1,2) = V(1,2) + \int d(34) V(1,3)P(3,4)W(4,2). \quad (3.12.4)$$

$$\chi(12) = -i \int d(34) G(23)G(42)\Gamma(341) \quad (3.12.5)$$

3.13 GW approximation

Green's function theory and the quasiparticle concept constitute an elegant alternative to DFT to solve the many-body problem. The GW approximation is derived systematically from many-body perturbation theory. It is an extension of the Hartree-Fock approximation for self-energy by replacing the bare Coulomb potential V, with the dynamically screened potential W, [96]. GW approximation calculates the self-energy of a many-body system of electrons.

The GW method can be understood in terms of the eigenvalue equation as shown below:

$$(T + V_{ext} + V_h)\phi_{nk}(r) + \int dr\Sigma(r, r', \omega = E_{nk})\phi_{nk}(r') = E_{nk}\phi_{nk}(r) \quad (3.13.1)$$

where T is the kinetic energy V_{ext}, the external potential of the nuclei V_h, the Hartree potential E_{nk}, the quasiparticle energies with orbitals ϕ_{nk}, and n and k being the band and k-point indices respectively. In comparison to DFT, the exchange-correlation potential is replaced by the many-body self-energy Σ, and should be obtained together with the Green's function, the irreducible polarizability χ, the screened Coulomb interaction W, and the irreducible vertex function Γ, in a self-consistent procedure using equations (3.12.1) to (3.12.5). The equations (3.12.1) to (3.12.5) are exact and provide an alternative to the Schrödinger equation for the many-body system problem. However, for real systems approximations are essential.

Disregarding self-energy term in equation (3.12.3) yields the GW approximation in a way that equations (3.12.5) and (3.12.2) are reduced to:

$$P(12) = -iG(12)G(21^{\dagger}) \tag{3.13.2}$$

and

$$\Sigma(12) = iG(12^{\dagger})W(12). \tag{3.13.3}$$

For comparison, the Hartree-Fock self-energy and GW self-energy can be expressed as:

$$\Sigma(1,2) = iG(1,2)V(1^{\dagger},2) \text{ and } \Sigma(1,2) = iG(1,2)V(1^{\dagger},2) \tag{3.13.4}$$

respectively where the Coulomb interaction is replaced by the screened Coulomb interaction. The V and W can be expressed as:

$$V(1,2) = \frac{1}{r_1 - r_2}\delta(t_1 - t_2) \tag{3.13.5}$$

$$W(1,2) = \int dr_3 \frac{1}{|r_1 - r_3|} \in^{-1} (r_3, r_2, t_1 - t_2) \tag{3.13.6}$$

W is dynamic and shorter ranged, whilst V is static. GW self-energy can also be expressed as:

$$\Sigma_{GW}(w) = iGW = iGV + iG[W - V] = \Sigma_x + \Sigma_c(\omega) \tag{3.13.7}$$

where $W - V = W^c$ is the difference between the screened and bare Coulomb interactions. Further expressing the real part of W^c as asum of its components, the screened exchange (SEX) and Coulomb-hole (COH) we get [97][98][99]:

$$\Sigma = \Sigma_{SEX} + \Sigma_{COH} \tag{3.13.8}$$

$$\Sigma_{SEX(r,\,r',\omega)} = -\sum_n^{occ} \psi_n(r)\,\psi_n{}^*(r') ReW(r, r', \omega - \in_n) \tag{3.13.9}$$

and

$$\Sigma_{COH(r,\,r',\omega)} = -\sum_n^{all} \psi_n(r)\,\psi_n{}^*(r') \int_0^\infty d\omega' \frac{ImW(r,r',\omega')}{w-\in_n-\omega'} \tag{3.13.10}$$

In summary the implementation of the GW method is illustrated as shown in figure 3.1 below.

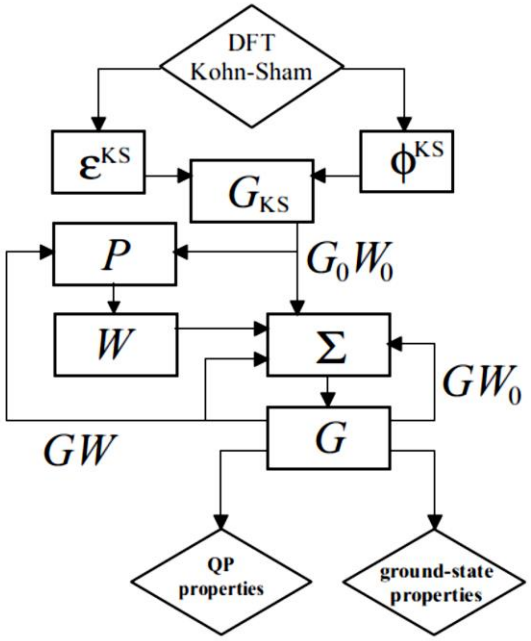

Figure 3.1: Flow diagram showing the practical implementation of the GW method. The partial self-consistent GW_0 updates the self-energy operator $\boldsymbol{\Sigma}$, and the self-consistent GW updates the screened Coulomb potential W [100].

3.14 Bethe-Salpeter Equation (BSE)

Appropriate description of the electron-electron correlation and electron-hole interaction is highly required to investigate the electronic and optical properties of materials. These properties can be well described through the solution of the BSE. The BSE describes the bound states of a two-body (particles) quantum field theoretical system in a relativistically covariant formalism. The BSE is the third and final step of a three-stage computation, DFT, GW and BSE, whose target is to determine the optical properties of material systems. The procedures determine the optical response function, which is the frequency dependent dielectric function including excitonic effects on top of standard DFT calculations, hybrid functionals or the GW. It gives an appropriate description of the absorption and energy-loss spectra which correctly describes important excitonic effects [101].

The four-point reducible polarizability is the key quantity:

$$L(1,2,3,4) = L_0(1,2,3,4) - G_2(1,2,3,4) \tag{3.14.1}$$

where G_2, describes the propagation of the two particles and L_0, is the disconnected part consisting of the two one-particle Green's function and is given by:

$$L_0 = i\mathrm{G}(1,3)\mathrm{G}(4,2). \tag{3.14.2}$$

L satisfies a Dyson-like equation therefore the BSE takes the form:

$$L(1,2,3,4) = L_0(1,2,3,4) + \int d5678 L_0(1,2,5\,6)\,[v(5,7)\delta(5,6)\delta(7,8) + \chi(5,6,7,8)]L(7,8,3,4) \tag{3.14.3}$$

Where χ is the standard approximation for interaction given by:

$$\chi = \frac{i\delta\Sigma(5,6)}{\delta G(7,8)} \tag{3.14.4}$$

In practice, BSE can be solved through diagonalizing a two particle excitonic Hamiltonian which gives information on the excitonic eigenstates and eigenvalues [102]. For the BSE, it is favorable to restrict the number of bands when solving the BSE equations due to the fact that the computational costs grow very steeply with the number of occupied and virtual bands used. To solve equation (3.14.3) we have to approximate the many-body interaction kernel Ξ. The standard approximation consists in using the GW self-energy of equation (3.13.7). Therefore the solution of the BSE corresponds to the inclusion of vertex corrections in P through a second iteration of Hedin's cycle of equations [103].

3.15 Optical absorption of semiconductors

The absorption coefficient α, is defined as a measure that defines the capability of light of a specific wavelength to penetrate a material before being absorbed. It can be calculated from optical transmission data. The transmission coefficient T, can be determined by:

$$T = \frac{I}{I_0} \tag{3.15.1}$$

where I_0 and I are the intensities of monochromatic light before and after transmission through a material of thickness x, respectively. T can further be determined after considering numerous reflections.

$$T = \frac{(1-R)^2 \exp(-\alpha x)}{1-R^2 \exp(-2\alpha x)} \tag{3.15.2}$$

where R, is the coefficient of reflection. The imaginary component of the index of refraction can then be determined as:

$$k = \frac{\lambda \alpha}{4\pi} \tag{3.15.3}$$

The real part of the index of refraction n, is significantly larger than the imaginary part k, close to the band edge. Therefore, the reflection coefficient can be expressed as:

$$R = \frac{(n-1)}{(n-1)^2}\,. \tag{3.15.4}$$

Absorption coefficients of direct and indirect band semiconductors are calculated differently [104]. The direct band absorption coefficient is calculated as follows:

$$\alpha = A(E - E_g)^{1/2} \tag{3.15.5}$$

where *A*, is a constant which is material specific, *E* is photon energy and E_g is the bandgap energy. Applying the parabolic approximation the absorption coefficient of indirect semiconductors becomes [105]:

$$\alpha = \alpha_a + \alpha_e \tag{3.15.6}$$

where α_a and α_e are the absorption coefficients involving the absorption and emission of a phonon respectively calculated as:

$$\alpha_a = C(E - E_g + E_p)^2 \text{ where } E > E_g - E_p \tag{3.15.7}$$

$$\alpha_e = D(E - E_g + E_p)^2 \text{ where } E > E_g + E_p \tag{3.15.8}$$

C and *D* are material and temperature-dependent constants.

3.15.1 Relation of Complex Dielectric Function to Observables

The absorption coefficient of a material was described in the previous section and can be obtained through manipulation of equation (3.15.3). Using the relationship between the velocity, frequency and wavelength of light ($c = f\lambda$) [104], equation (3.15.3) can be re-written as:

$$\alpha = \frac{4\pi kf}{c} \tag{3.15.9}$$

The dielectric function is a measure of the degree of resistance that is encountered when forming an electric field in a specific medium. The response of materials to external electric fields is dependent on the frequency of the field. This frequency dependence echoes the fact that materials polarization does not change instantly due to an applied electric. This phenomenon results in the dielectric function being treated as a complex function due to the phase difference [106].

The complex dielectric function can then be divided into two parts, the real part ($\in'$) and imaginary part ($\in''$) as:

$$\in = \in' + \in'' \tag{3.15.10}$$

The real and imaginary parts of the dielectric function are related to the extinction coefficient *k*, and index of refraction *n*, through the following equations [107]:

$$\in' = n^2 - k^2 \tag{3.15.11}$$

and

$$\in'' = 2nk \tag{3.15.12}$$

Optical constants such as absorption coefficient, extinction coefficient, refractive index and reflectivity of the materials will then be computed and analysed from the real and imaginary dielectric function [108]. The analysis will therefore determine if the materials are suitable to be used in optics, photonics, image sensors, infrared detectors, energy conversion as well as displays and LEDs, just to mention a few.

3.15.2 Macroscopic and microscopic frequency dependent dielectric function

The total macroscopic electric field follows the periodicity of the external perturbation, nevertheless the microscopic total electric field additionally exhibits rapid vibrations on the primitive cell scale. The dielectric function can be written as:

$$E(\boldsymbol{r},\omega) = \int d^3\boldsymbol{r}' \in_{mac}^{-1} (\boldsymbol{r},-\boldsymbol{r}',\omega)E_{ext}(\boldsymbol{r}',\omega), \tag{3.15.13}$$

where E and E_{ext} are the total and external macroscopic electric fields respectively and $\in_{mac}$ is the macroscopic dielectric function [104]. The microscopic total electric field, $e(\boldsymbol{r},t)$ can be expressed as:

$$e(\boldsymbol{r},\omega) = \int d^3\boldsymbol{r}' \in^{-1} (\boldsymbol{r},\boldsymbol{r}',\omega)E_{ext}(\boldsymbol{r}',\omega). \tag{3.15.14}$$

The macroscopic dielectric function only depends on position difference. Transferring equation (3.15.13) to momentum space yields:

$$E(q,\omega) = \in_{mac}^{-1} (q,\omega)E_{ext}(q,\omega). \tag{3.15.15}$$

The microscopic dielectric function is only invariant under translation by a lattice vector *R*:

$$\in (r,r',\omega) = \int \frac{d^3q'}{(2\pi)^3}\frac{d^3q''}{(2\pi)^3} e^{iq'r}\epsilon(q',q'',\omega)e^{-iq''r'} =$$

$$\int \frac{d^3q'}{(2\pi)^3}\frac{d^3q''}{(2\pi)^3} e^{iq'(r+R)}\epsilon(q',q'',\omega)e^{-iq''(r'+R)}, \tag{3.15.16}$$

yielding,

$$\in (\boldsymbol{r},\boldsymbol{r}',\omega) = \epsilon(\boldsymbol{r}+R,\boldsymbol{r}'+R,\omega). \tag{3.15.17}$$

The difference between q' and q'' is a reciprocal lattice vector. The relationship between the macroscopic total and external field can then be established leading to a relation between the macroscopic and microscopic dielectric functions as [109]:

$$\in_{mac}^{-1} (q,\omega) = \in_{00}^{-1} (q,\omega), \tag{3.15.18}$$

implying that:

$$\in_{00}(q,\omega) = [\in_{mac}^{-1}(q,\omega)]^{-1}, \tag{3.15.19}$$

Slow varying external fields cause rapid vibrations on the macroscopic scale, the resultant effect on the macroscopic dielectric function are called local field effects. For materials that are also homogeneous on the microscopic scale, for example the homogeneous electron gas, no local field effects are present leading to:

$$\in_{mac}(q,\omega) = \in_{00}(q,\omega). \tag{3.15.20}$$

where local fields are neglected.

3.16 Optical transitions

There are two types of optical transitions namely interband transition and intraband transition. Interband transition is an electronic transition between different electronic bands while the intraband transition is a transition between electronic states within the same band.

3.16.1 Inter-band transitions

We can have direct and indirect interband transitions. In transitions of the electrons, the energy and the momentum are conserved. Consequently, phonons do not take part in direct transitions due to the fact that the wave vector k, of the phonons is much larger than that of the photons. However, phonons transitions are involved in the indirect transitions. Therefore, the transition probabilities of the direct transitions are much higher than those of indirect transitions.

Interband transitions contribution to the dielectric function can be split into direct and indirect transitions as follows [110]:

$$\in_{inter}(\omega) = \in_{inter(1)}(\omega) + i \in_{inter(2)}(\omega), \quad (3.16.1)$$

where $\in_{inter(1)}(\omega)$ is the real part and $\in_{inter(2)}(\omega)$ is the imaginary part obtained from band structure calculation. The imaginary quantity can be evaluated through direct electronic transition between occupied and unoccupied electronic states by:

$$\in_{inter(2)}(\omega) = \frac{8\pi^2 e^2}{m^2\omega^2 V}\sum_{c,v}\sum_{k}|c, \mathrm{k}\langle\hat{\mathrm{e}}\cdot\mathrm{p}\rangle v, \mathrm{k}|^2 \times \delta[E_c(\mathrm{k}) - E_v(\mathrm{k}) - \omega\hbar] \quad (3.16.2)$$

where *c* and *v* are the conduction and valence states respectively. |*n*, *k* > are the full-potential linearized augmented plane–wave (FLAPW) eigenstates, p is the momentum operator and $\hat{e}$ is the external field vector [111]. The real part is attained from the Kramers-Kronig transformation that connects the real and imaginary parts of any complex function that is analytic in the upper half-plane as follows [112]:

$$\in_{inter(1)}(\omega) = 1 + \frac{2}{\pi}P\int_0^{\infty}\frac{\in_{inter(2)}(\omega'')\omega'}{\omega'^2-\omega^2+i\eta}d\omega' \quad (3.16.3)$$

where *P* is the principal value of the integral and is a small complex shift used to smoothen the spectrum. Once the dielectric function is computed, all other observables can then be obtained.

3.16.2 Intra-band transitions

Electrons are excited to higher energy states within the same band. These transitions are only in metals and sometimes in highly doped semiconductors. Conversely, the intra-band dielectric function is also obtained as follows:

$$\in_{intra}(\omega) = \in_{intra(1)}(\omega) + i \in_{intra(2)}(\omega). \quad (3.16.4)$$

The real and imaginary parts of the dielectric constants as described by the Drude free-electron theory are:

$$\in_{intra(1)}(\omega) = 1 - \frac{\omega_p^2\tau(\omega)^2}{1+\omega^2\tau(\omega)^2}, \quad (3.16.5)$$

and

$$\in_{intra(2)}(\omega) = \frac{\omega_p^2 \tau(\omega)^2}{\omega(1+\omega^2\tau(\omega)^2)}\ , \tag{3.16.6}$$

where $\tau(\omega)$ is the relaxation time and ω_p is the plasma frequency. The relaxation time can be obtained from the ratio of the above two equations as:

$$\tau(\omega) = \frac{1- \in_{intra(1)}(\omega)}{\in_{intra(2)}(\omega)\omega} \tag{3.16.7}$$

The plasma frequency ω_p, is given by:

$$\omega_p = \sqrt{\frac{4\pi N e^2}{m}} \tag{3.16.8}$$

where m is the effective optical mass, N is the density of conduction electrons and e is the elementary charge [113][114].

3.17 Thermal transport

The thermal transport of dielectric solids can be determined by means of the Boltzmann transport equation (BTE) regarding its distribution of phonons subjected to a thermal gradient. The equation employs the particle-like nature of phonons to model heat transfer at small scales. Subsequent to solving the equation, the thermal conductivity is obtained. The equation arises by considering a probability distribution for the position and momentum of a typical particle [115]. The general form of the BTE takes the form:

$$\frac{\partial f}{\partial t} + \overrightarrow{v_g}\nabla f + \frac{\partial k}{\partial t}\nabla_k f = \left(\frac{\partial f}{\partial t}\right)_{collisions}, \tag{3.17.1}$$

where $f(\overrightarrow{r}, t, \overrightarrow{k})$ is the phonon distribution function representing the number of phonons at position $\overrightarrow{\boldsymbol{r}}$, at time t, with a wave vector $\overrightarrow{k}$, and polarization p, per unit

solid angle per unit wave number interval per unit volume. $\overrightarrow{v_g}$ is the phonon group velocity. The term on the right-hand side of equation (3.17.1) represents the change in phonon distribution due to phonon collisions. When these collisions (elastic or inelastic) are very large, the kinetic theory can be used to characterize these collisions in terms of effective scattering or relaxation times. Thus, the collision term can be expressed in terms of the relaxation time approximation as shown below.

$$\left(\frac{\partial f}{\partial t}\right)_{collisions} = -\frac{f-f_0}{\tau_{eff}}, \tag{3.17.2}$$

where τ_{eff} is the relaxation time of the phonons and f_0, is the equilibrium phonon distribution given by the Bose-Einstein distribution as:

$$f_0 = \frac{1}{e^{\left(\frac{\hbar\omega}{kT}\right)}-1}. \tag{3.17.3}$$

Transforming the phonon distribution function into a phonon energy density yields:

$$e''_\omega = \hbar\omega D(\omega) f, \tag{3.17.4}$$

where $\hbar$ and ω are the modified Planck's constant and phonon frequency respectively. $D(\omega)$ is the phonon density of states function. The BTE now takes the form:

$$\frac{\partial e''_\omega}{\partial t} + \vec{s} v_g \nabla e''_\omega = \frac{e^0_\omega - e''_\omega}{\tau_{eff}} \tag{3.17.5}$$

where e''_ω is the phonon energy density with frequency ω, at position $\overrightarrow{\boldsymbol{r}}$, at time t, per unit volume, per unit time, per unit frequency, per unit interval and $\vec{s}$ represents the unit direction vector propagation.

4 Computational Details

All computations during this study were done using the VASP code [116] which is based on DFT and solves the Kohn-Sham equations using the projector augmented wave (PAW) [117] method. The projector augmented wave method is an all-electron method for efficient *ab initio* molecular dynamics simulations with full wave functions [118]. The method is a generalization of the pseudopotential and linear augmented-plane-wave methods, allowing density functional theory calculations to be performed with better computational accuracy and efficiency [119].

The four files, INCAR, POSCAR, POTCAR and KPOINTS are the central input files in the working directory for VASP execution. The starting input data were extracted from the Materials Project [120]. LDA and GGA approximations to the exchange-correlation energy were used as previously discussed in chapter 3. Grimme DFT-D2, DFT-D3, Tkatchenko-Scheffler (PBE+TS), PBEsol and the optB86b-vdW dispersion corrections were used to account for the long range van der Waals forces between layers [121].

Pymatgen [122] was used to automatically generate KPOINTS with grid density = 1000 / atom. The POTCAR files use an energy cut-off of 520 eV from Materials project for the plane wave basis which was used for the bulk calculations. The global break condition for the electronic self-consistence convergence was set at 1×10^{-8} eV in order to improve accuracy.

For structural minimization, interatomic forces were minimized using a conjugate gradient method. Elastic constants were computed using two ways in *ab initio* methods namely the energy-strain approach and the stress-strain approach [123].

For the phonon calculations, supercell and finite displacement approaches were used with $4 \times 4 \times 4$ supercell of the conventional unit cell through the PHONOPY code [124].

For optical properties, a three-stage computational process was implemented. The first stage was a DFT calculation which enabled us to obtain the electronic structures of the systems which was then used as input for the second stage, the GW calculation. At the GW stage, the Kohn-Sham exchange correlation potential was then replaced by the electron self-energy. The self-consistent GW_0 calculation was conducted keeping the screened Coulomb fixed at its DFT value, computing only the Green's function. This is also illustrated in Figure 3.1, the flow diagram showing the practical implementation of the GW method. The third stage was the BSE calculation where the optical property observables such as the absorption coefficient, reflectivity, refractive index, extinction coefficient and loss factor were determined. The BSE dielectric matrix was calculated based on the GW input data and the optical properties from the BSE dielectric matrix. Lastly, lattice thermal transport properties were determined by means of the Boltzmann transport equation (BTE) regarding its distribution of phonons subjected to a thermal gradient. This was done using a single-mode relaxation time approximation in the linearized phonon Boltzmann equation from first-principles anharmonic lattice dynamics calculations as implemented in the PHONO3PY package [124][125].

4.1 Work flow

VASP was central to all the computations of this study. As earlier stated in the previous section, the four files, INCAR, POSCAR, POTCAR and KPOINTS were the central input files in the working directory.

The INCAR file, which is the central input file of VASP controlled all the calculations. The KPOINTS file containing the k-point coordinates and mesh size for creating the k-point grid and POSCAR file containing lattice geometry and the ionic positions were obtained through materials project database. The POTCAR file containing the pseudopotentials for all the atomic species used in the calculations were generated from the POSCARS through pymatgen [116].

First step in working with materials is to relax the structures. This was done through uniform scaling of the structures resulting in thirteen volumes which were added when necessary. At each volume, atoms were allowed to relax to positions where they had lowest energies. LDA, Grimme DFT-D2, DFT-D3, Tkatchenko-Scheffler, PBEsol and the optB86b-vdW dispersion corrections were used to account for the long range van der Waals forces and the electronic ground state data (energy and volume) was fitted into the third order Birch-Murnaghan equation of state [126]. For each dispersion correction, cohesive energy, formation energy, cell volume and lattice constants were obtained. The parameters for the most stable polymorph were then used to compute and simulate mechanical, dynamic, band structures, optical and thermal properties of materials under study.

Elastic constants were analyzed through ELATE [127], an online tensor analysis tool. From the analysis, mechanical properties such as bulk, Young's and shear moduli, Poisson's ratio according to the three averaging schemes (Voigt, Reuss, and Hill) were obtained. The conditions of mechanical stability of unstressed crystalline structures were also verified using the Born stability criterion [128]. Dynamic stability (only hard modes or both hard and soft modes) was ascertained through the PHONOPY code as earlier stated. The MBJ and HSE06 hybrid functionals were used to improve the accuracy of the electronic band structure calculations. GW and BSE calculations were later conducted. Lastly the thermal transport properties were determined as stated in section 4. The same supercell as for the phonon dispersion and a mesh of 24×24×12 was used at 300 K. 1058 unique displacements were generated through PHONO3PY package and all triplet displacements in the supercell were included in the lattice thermal conductivity calculations.

4.2 Equation of state (EOS)

An equation of state (EOS), of a system describes how the volume or density of a material system varies as a function of pressure and temperature. The relationship between the pressure and the corresponding change in volume provides important information regarding the compression of solids under the effect of pressure and is obtained by fitting experimental data into the 3rd order Birch–Murnaghan EOS. The Birch-Murnaghan's EOS is based on finite strain theory using the Eulerian strain [126][129]. It is given by:

$$P(V) = \frac{3B_0}{2}\left[\left(\frac{V_0}{V}\right)^{\frac{7}{3}} - \left(\frac{V_0}{V}\right)^{\frac{5}{3}}\right]\left\{1 + \frac{3}{4}(B_0' - 4)\left[\left(\frac{V_0}{V}\right)^{\frac{2}{3}} - 1\right]\right\}. \quad (4.3.1)$$

where P is the pressure, V_0 is the reference volume, V is the deformed volume, B_0 and B_0' are the bulk modulus and its derivative with respect to pressure respectively. The bulk modulus and its derivative are obtained from fits to experimental data and are defined as:

$$B_0 = -V\left(\frac{\partial P}{\partial V}\right)_{P=0} \quad (4.3.2)$$

and

$$B_0' = -V\left(\frac{\partial B}{\partial P}\right)_{P=0}. \quad (4.3.3)$$

B_0 is proportional to the curvature of the EOS at the equilibrium volume together with its derivative are higher order derivatives of the energy function. The expression for the equation of state is then attained through expanding the free energy f, in terms of reference and equilibrium volume in the form of a series as:

$$f = \frac{1}{2}\left[\left(\frac{V_0}{V}\right)^{-\frac{2}{3}} - 1\right]. \quad (4.3.4)$$

Expressing energy as a function of volume, the internal energy *E(V)*, is found by integration of equation (4.3.1) with respect to volume giving us the Birch-Murnaghan's EOS as:

$$E(V) = E_0 + \frac{9V_0B_0}{16}\left\{\left[\left(\frac{V_0}{V}\right)^{\frac{2}{3}} - 1\right]^3 B_0' + \left[\left(\frac{V_0}{V}\right)^{\frac{2}{3}} - 1\right]^2 \left[6 - 4\left(\frac{V_0}{V}\right)^{\frac{2}{3}}\right]\right\}. \qquad (4.3.5)$$

where E_0 is the equilibrium volume of the system.

4.3 Cohesive and formation energy

4.3.1 Cohesive energy

It is the energy that must be supplied to a solid to separate it into its constituents neutral free atoms at rest and at infinite separation with the same electronic configurations and therefore a measure of the inter-molecular energy for a substance [130]. Considering a unit cell with N atoms, the bulk cohesive energy per unit cell is given by:

$$E_{coh}(\infty) = \frac{E_{tot}(\infty) - \sum_N E_{iso}}{N}, \qquad (4.4.1)$$

where E_{tot} is the total energy of the compound, E_{iso} is the energy of an isolated atom and (∞) refers to bulk. Equation (4.4.1) can be modified for applications on nanoscale (r) size material [131] as:

$$E_{coh}^{LDA,GGA}(r) = \frac{E_{tot}^{LDA,GGA}(r) - \sum_N E_{iso}}{N}. \qquad (4.4.2)$$

4.3.2 Formation energy

The breaking and formation of bonds during a chemical reaction cause energy change. The heat absorbed or released from a system under constant pressure is known as enthalpy of the reaction. The formation energies are given by:

$$E_F = \sum E_{coh}(products) - E_{coh}(reactants). \quad (4.4.3)$$

Considering that all compounds of this study have the form MX_2, equation (4.4.3) can now be formulated as:

$$E_F(MX_2) = E_{coh}(MX_2) - \left[\frac{E_{coh}(M) + 2E_{coh}(X)}{3}\right]. \quad (4.4.4)$$

A negative result of equation (4.4.4) implies that the compound under study is stable against decomposition into its constituent atoms [132].

4.4 Elastic constants

Stress produces strain, but the amount of strain produced depends on the compound itself. Different types of stresses and their corresponding strains within the elastic limit are related and are referred to as elastic constants. Elastic properties provide valuable information about the binding characteristic between adjacent atomic planes. Anisotropic characters of binding and structural stability are usually defined by the elastic constants C_{ij}. These constants are related to the Young's modulus, Bulk modulus, shear modulus and Poisson's ratio which play crucial role in determining the strength of the materials [133]. Elastic constants can be computed using two methods in *ab initio*, the energy strain and stress-strain approach.

4.4.1 Energy-strain

Theoretically, the elastic constants are defined by means of a Taylor expansion of the total energy $E(V, \delta)$, for the system with respect to a small strain δ, of the lattice. The elastic behavior of a lattice is described by its matrix of second-order elastic constants given as:

$$C_{ij} = \frac{1}{V_0}\left(\frac{\partial^2 E}{\partial \varepsilon_i \partial \varepsilon_j}\right) \quad (4.5.1)$$

where E is the energy of the system, V_0 is the volume of an unstrained and ε represents a strain. For an arbitrary homogeneous deformation by an infinitesimal strain, the energy of the crystal is expressed as:

$$E = E_0 + \frac{1}{2} V_0 \sum_{i,j=1}^{6} C_{ij} \varepsilon_i \varepsilon_j + O(\varepsilon^3) \quad (4.5.2)$$

A crystalline structure is considered to be mechanically stable in the absence of an external load and in the harmonic approximation if the elastic energy given by equation (4.5.2) is always positive. This is known as the Born elastic stability criterion [134].

4.4.2 Stress-strain

Hooke's law, states that within the elastic limits the stress is proportional to the strain. The stress-strain approach relies on the feature of VASP to directly calculate the stress tensor. Once the stress tensor components can be computed by an *ab initio* method it implies that the elastic constants matrix can also be directly derived. As opposed to the previous energy-strain approach, several magnitudes of strain have to be calculated to obtain the elastic constant from an analytic fit to the total energy data. In the stress-strain approach only one evaluation is in principle sufficient enough to attain the same information. The elastic stiffness tensor *C*, relates the stress tensor σ, and the strain ε, by Hooke's law given as [135]:

$$\sigma_{ij} = C_{ijkl} \varepsilon_{kl} \quad (4.5.3)$$

where *(i, j, k, l = x, y, z)*. This is the approach which was implemented during this study.

The calculated elastic constants were analyzed by feeding the stiffness matrix into ELATE, an online tensor analysis tool as earlier stated in section 4.1. Mechanical properties such as bulk, Young's and shear moduli, Poisson's ratio, according to the three averaging schemes (Voigt, Reuss, and Hill) and eigenvalues of the stiffness matrix were obtained. The conditions of mechanical stability of unstressed crystalline structures were also verified using the Born stability criterion for trigonal systems.

4.5 Phonons

When an atom in a crystal is displaced from its equilibrium position, the forces on all atoms in the crystal will rise. Analysis of the forces associated with a systematic set of displacements provides a series of phonon frequencies. Phonon plays essential roles in dynamical behaviors and thermal properties of materials. Dynamical stability of a material is essential since minimizing the energy of a structure does not guarantee stability [136]. In the harmonic approximation all phonons need to have real and positive frequencies in order to ascertain dynamical stability. Phonon calculations can be done either through the linear response or finite displacement methods.
Linear response provides an analytical way of computing the second derivative of the total energy with respect to a given perturbation. The force constants matrix depends on the ground state electron charge density and on its linear response to a distortion of atomic positions. This implies that the second order change in energy depends on the first order change in the electron density [137].

In this study the phonon calculations, supercell and finite displacement approaches were used. Translational invariance implies that the number of separate calculations required to do the computation is at most three times the number of atoms in the primitive cell. However, for most materials, symmetry relations can be used to reduce this number considerably [138]. $4 \times 4 \times 4$ supercells of the conventional unit cell were used along high symmetry directions. The advantage of the finite displacement method over the linear response is that phonon anharmonicity can be investigated by increasing the amplitude of the displacements.

4.6 Optical properties

Optical processes such as absorption, reflection, refraction and transmission are observed in solids when they interact with electromagnetic radiation in the visible range. In this study optical processes at microscopic level are discussed. The dielectric

matrix is computed at the BSE stage and is used to derive the absorption coefficient $\alpha(\omega)$, refractive index (ω), reflectivity $R(\omega)$, extinction coefficient $k(\omega)$ and the energy loss spectrum $L(\omega)$ from the real $\in_1 (\omega)$ and imaginary $\in_2 (\omega)$ parts of the dielectric function. The real and imaginary parts of the dielectric function are connected according to the Kramer-Kronig relation [108] as given in the equations below.

The absorption coefficient is defined as a quantity that describes the ability of light of a particular wavelength to penetrate a material before being absorbed and is given by:

$$\alpha(\omega) = \sqrt{2(\omega)}\left[\sqrt{\in_1^2 (\omega) + \in_2^2 (\omega)} - \in_1 (\omega)\right]^{\frac{1}{2}} \tag{4.7.1}$$

Refractive index is defined as the ratio of the velocity of light in a vacuum to its velocity in a specified medium. It is denoted as follows:

$$n(\omega) = \left[\frac{\sqrt{\in_1^2(\omega)+\in_2^2(\omega)}+\in_1(\omega)}{2}\right]^{\frac{1}{2}} \tag{4.7.2}$$

Reflectivity is a degree of the ability of a surface to reflect radiation, equal to the reflectance of a layer of material adequately thick for the reflectance not to depend on the thickness of the material and is given by:

$$R(\omega) = \left[\frac{\sqrt{\in(\omega)-1}}{\sqrt{\in(\omega)+1}}\right]^2 \tag{4.7.3}$$

Extinction coefficient is a measure of the rate of attenuation of transmitted light through scattering and absorption of the electromagnetic radiation in the medium. It is expressed as:

$$k(\omega) = \left[\frac{\sqrt{\in_1^2(\omega)+\in_2^2(\omega)}-\in_1(\omega)}{2}\right]^{\frac{1}{2}} \tag{4.7.4}$$

Energy loss spectrum can be attributed to inelastic interactions that include phonon excitations, inter-band and intra-band transitions and plasmon excitations expressed by:

$$L(\omega) = \frac{\epsilon_2(\omega)}{\epsilon_1^2(\omega)+\epsilon_2^2(\omega)} \tag{4.7.5}$$

4.7 Tauc plots

A Tauc plot is used in the determination of the optical bandgap in semiconductors. The Tauc plot shows the quantity, $h\nu$ which is the energy of the light on the abscissa and the quantity $(\alpha h\nu)^{1/n}$ on the ordinate, where α is the absorption coefficient of the material. The determination of optical bandgap is attained through the Tauc's [139][140] equation shown below.

$$\alpha h\nu = A\left(h\nu - E_g\right)^n \tag{4.7.6}$$

where A is a constant, $h\nu$ is photon energy, E_g is the allowed energy gap, n denotes the nature of the transition, $n = \frac{1}{2}$ for allowed direct transition and n = 2 for allowed indirect transition. Thus, straight line segments in $(\alpha E)^2$ indicate direct gaps and straight line segments in $(\alpha E)^{1/2}$ indicate indirect gaps. Bandgaps are then calculated from the Tauc plots by fitting a line through the linear portion of the band edge region which indicates the onset of absorption. Extrapolating the linear region to the abscissa yields the energy of the optical bandgap of the material.

4.8 Thermal properties

Boltzmann Transport Equation is an effective tool for analyzing transport phenomena within systems that contain density as well as temperature gradients. The equation, which was discussed in section 3.17, is applied to analyze the general currents within

a system, the transport coefficients and the relationships between them. Lattice thermal transport can be precisely calculated through solving the linearized Boltzmann transport equation (BTE) with the phonon-phonon interaction strength obtained using first principles calculations [141].

The thermal transport properties allow us to determine if the systems under study are suitable to be used in solar cell designs as well as in opto-electronics just to name but a few. The desired properties to be computed as functions of temperature are the lattice thermal conductivity, constant volume heat capacity C_v, Helmholtz free energy F, and entropy S, for materials to be considered suitable for solar cells. Materials with a high thermal conductivity are widely used in thermoelectric applications.

5 Results and discussion

In this chapter we present the results of numerical investigations of the structural, mechanical, dynamical, electronic, optical and thermal properties of the layered TMDs, PtS_2, $PtSe_2$, and $PtTe_2$. Density Functional Theory offers the most efficient option for Computational Materials Science, but has the drawback that there are a multitude of approximate exchange-correlation energy functionals available. None of the approximations is always optimal and it is not always obvious which approximation to use for a given compound. In this study seven different approximate exchange-correlation functionals were explored. The local density approximation LDA, has a sound theoretical basis and is a reliable first approximation to explore. The semilocal, generalised gradient approximations (GGA), PBE and PBEsol [142], are also based on sound theoretical arguments and have a minimal number of parameters that are fitted to data. Unfortunately the local and semilocal approximations do not take long range interactions into account. In layered systems this may be problematic since the inter-layer interactions can be dominated by long range van der Waals type forces. Here, four approximations to van der Waals forces were explored. The Grimme DFT-D2, DFT-D3 [76][143], Tkatchenko-Scheffler (DFT-TS) [143] and optB86b-vdW were added to the PBE exchange-correlation approximation. The optB86b-vdW [76][74] uses a different approach which is a non-local correlation functional that approximately takes long range interactions into account. The calculated structural, mechanical and dynamical results depended on the vdW correction, which is included as a correction to the electronic energy calculated with PBE. The DFT-TS approximation gave the most stable polymorph for all the three systems under study which had equilibrium volumes data most comparable to available experimental data. Further studies on electronic, optical and thermal properties were then determined. Starting from the wavefunction and energies of the Kohn-Sham equations, the quasiparticle (QP) GW and BSE calculations were performed.

5.1 Platinum disulfide (PtS_2)

PtS_2 has one experimentally observed polymorph, a trigonal crystal structure belonging to the space group, $P\bar{3}m1$. The structures of these compounds under study have been established experimentally by powder as well as single crystal x-ray diffraction methods [144].

5.1.1 Equation of state (EOS) for PtS_2

The study of PtS_2 was conducted with the seven exchange-correlation functionals discussed in the introduction, namely LDA, PBE, PBEsol, Grimme DFT-D2, DFT-D3, Tkatchenko-Scheffler (DFT-TS) and optB86b-vdW. A range of equilibrium volumes were obtained using the different functionals. The energy versus volume EOS for PtS_2 obtained using different functionals are given below in Figures 5.1 to 5.7.

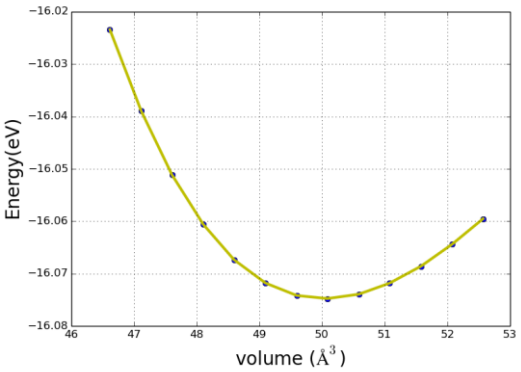

Figure 0.1: LDA

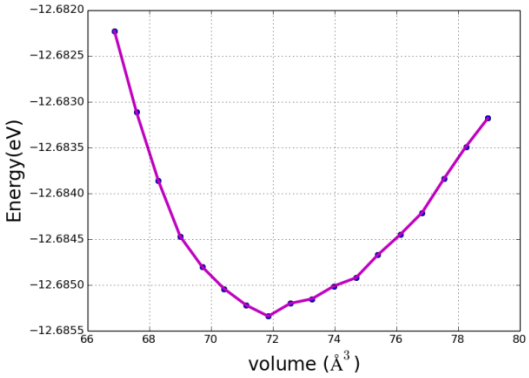

Figure 0.2: PBE

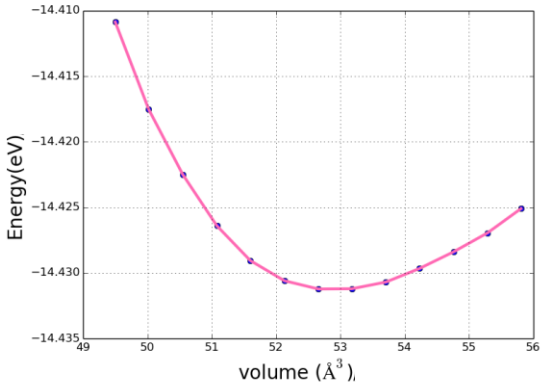

Figure 0.3: PBEsol

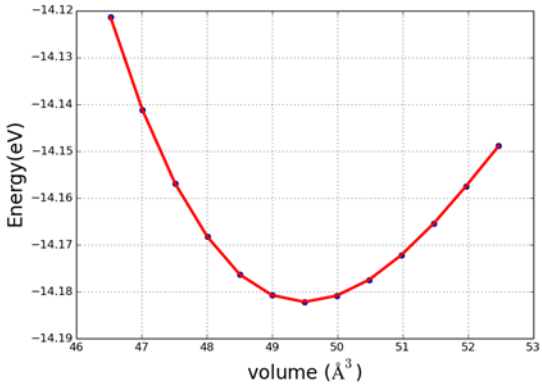

Figure 0.4: PBE+D2

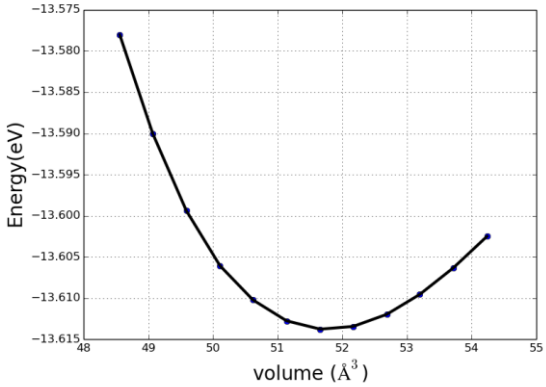

Figure 0.5: PBE+D3

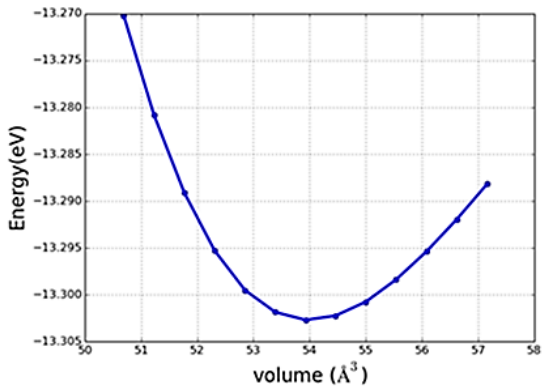

Figure 0.6: PBE+TS

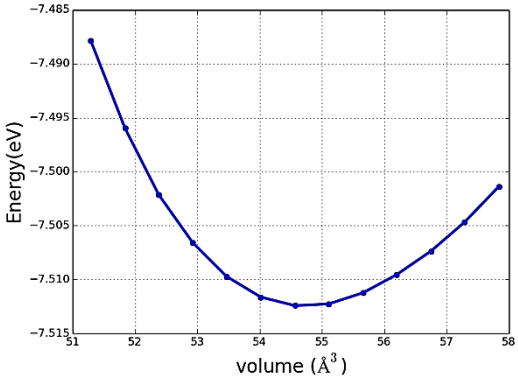

Figure 0.7: optB68b

The EOS for PBE and PBEsol have relatively small percentage change in energy over the range of volumes included in the study as illustrated in Figures 5.2 and 5.3

respectively. This is a direct consequence of the lack of long-range interaction included in the semilocal GGA approximations. When the layers of the compound are sufficiently far apart, the binding energy comes almost exclusively from intra-layer interactions with a minimal contribution from inter-layer interactions. Changing the volume results in very small changes in the energy since the intra-layer binding energy is almost invarient under changes in the inter-layer spacing. Including vdW corrections introduces a stronger dependence of the energy on the inter-layer spacing.

5.1.2 Structural and energetic properties of PtS_2

Geometry optimization gives the equilibrium lattice parameters and relaxed internal parameters. The results for this study are given in table 5.1. The obtained results were compared with experimental results in order to ascertain the exchange-correlation functional that had the least deviation from experimental equilibrium volume results. The calculated volumes of the system were also compared to other theoretical values obtained from the literature.

Table 0.1: The equilibrium structural and energetic properties for PtS_2 calculated using various exchange-correlation functionals. The experimental structural properties are also shown for comparison

Functional	$a = b$(Å)	c(Å)	V_0(Å)^3	E_{coh} (eV/atom)	E_{form} (eV/atom)
LDA	3.566	4.548	50.042	-5.358	-0.471
PBE	3.573	6.504	71.908	-4.228	-0.365
PBE+D2	3.619	4.361	49.502	-4.728	-0.865
PBE+D3	3.604	4.602	51.742	-4.537	-0.674
PBE+TS	3.603	4.874	54.596	-4.434	-0.571
PBEsol	3.571	4.796	52,918	-4.810	-0.947
OptB86b	3.566	4.988	54.971	-2.502	-0.401
Exp[145]	3.543	5.038	54.769	-	-
Exp[146]	3,543	5.039	54.782	-	-
Exp[147]	3.51	5.03	53.67	-	-
Exp[148]	3.5432	5.0388	54.783	-	-

Equilibrium volumes obtained for LDA, PBEsol, Grimme DFT-D2, DFT-D3, PBE+TS and PBEsol were underestimated while optB86b-vdW and PBE overestimated the volume compared to the reported experimental values as illustrated in Table 5.1. LDA, PBEsol, Grimme DFT-D2, DFT-D3, and PBE-TS underestimated the experimental equilibrium volume by 8.6%, 3.4%, 9.6%, 5.5% and 0.3% respectively. PBE and optB86b overestimated by 31.3% and 3.7% respectively. Hence PBE+TS gave the smallest percentage deviation of volume from the available experimental data. The optB86b-vdW functional gave lattice parameters which were more comparable to the experimental data but is computationally more demanding.

The compound is energetically stable due to the negative cohesive and formation energies implying that they are stable against decomposition into their constituent atoms and constituent solid components. The range of results for different exchange-

correlation approximations and vdW corrections highlight a problem in applied DFT where there is no systematic way to improve the exchange-correlation approximations. The exact exchange-correlation includes long range interaction. Including vdW interactions in addition to semilocal exchange-correlation approximations is an attempt to address this problem.

5.1.3 Mechanical properties of PtS_2

Table 0.2: Calculated values of independent elastic coefficients for PtS_2

Functional	C_{11} (GPa)	C_{12}(GPa)	C_{13}(GPa)	C_{33}(GPa)	C_{44}(GPa)
LDA	243.48	70.25	31.65	40.68	48.40
PBE	137.32	37.21	2.35	1.92	0.66
PBE+D2	297.54	83.82	46.73	82.28	67.49
PBE+D3	233.43	64.87	28.42	37.66	44.68
PBE+TS	199.85	56.01	22.82	26.11	28.58
PBEsol	220.49	63.13	22.37	17.05	35.94
optB86b	209.74	63.87	30.03	28.13	34.65

The calculated results satisfied the Born stability criteria for hexagonal and trigonal systems, $C_{11} > |\boldsymbol{C_{12}}|$; $2\boldsymbol{C_{13}^2} < C_{33}(C_{11} + C_{12})$; $C_{44} > 0$; $C_{66} > 0$ and $C_{66} = (C_{11} - C_{12})/2$ [134].

From the obtained independent elastic coefficients, we further computed its bulk modulus (*K*), Young's modulus (*E*), shear modulus (*G*), Poisson's ratio (*v*) as well as Pugh ratio (*K/G*) as provided in Table 5.3 to Table 5.9 below.

Table 0.3: The LDA calculated, bulk, Young's, shear modulus and Poisson's ratio for PtS_2

Averaging scheme	Bulk (*K*) (GPa)	Young's (*E*) (GPa)	Shear (*G*) (GPa)	Poisson's ratio (*v*)	*K/ G*
Voigt	88.31	152.60	62.95	0.2120	1.40
Reuss	40.08	89.53	39.70	0.1277	1.01
Hill	64.19	121.57	51.33	0.1844	1.25

Table 0.4: The PBE calculated, bulk, Young's, shear modulus and Poisson's ratio for PtS_2

Averaging scheme	Bulk (*K*) (GPa)	Young's (*E*) (GPa)	Shear (*G*) (GPa)	Poisson's ratio (*v*)	*K/ G*
Voigt	40.04	63.96	25.92	0.2338	1.54
Reuss	1.92	3.16	1.29	0.2252	1.49
Hill	20.98	33.56	13.60	0.2334	1.54

Table 0.5: The PBE+D2 calculated, bulk, Young's, shear modulus and Poisson's ratio for PtS_2

Averaging scheme	Bulk (*K*) (GPa)	Young's (*E*) (GPa)	Shear (*G*) (GPa)	Poisson's ratio (*v*)	*K/ G*
Voigt	114.66	198.07	81.71	0.2121	1.40
Reuss	75.24	145.09	61.55	0.1786	1.22
Hill	94.95	171.71	71.63	0.1986	1.33

Table 0.6: The PBE+D3 calculated, bulk, Young's, shear modulus and Poisson's ratio for PtS_2

Averaging scheme	Bulk (*K*) (GPa)	Young's (*E*) (GPa)	Shear (*G*) (GPa)	Poisson's ratio (*v*)	*K/ G*
Voigt	83.10	145.57	60.25	0.2081	1.38
Reuss	37.00	83.66	37.25	0.1232	0.99
Hill	60.05	115.10	48.75	0.1806	1.23

Table 0.7: The PBE+TS calculated, bulk, Young's, shear modulus and Poisson's ratio for PtS_2

Averaging scheme	Bulk (*K*) (GPa)	Young's (*E*) (GPa)	Shear (*G*) (GPa)	Poisson's ratio (*v*)	*K/ G*
Voigt	69.90	116.04	47.43	0.2233	1.47
Reuss	26.01	60.07	26.94	0.1151	0.97
Hill	47.96	88.64	37.18	0.1920	1.29

Table 0.8: The PBEsol calculated, bulk, Young's, shear modulus and Poisson's ratio for PtS_2

Averaging scheme	Bulk (*K*) (GPa)	Young's (*E*) (GPa)	Shear (*G*) (GPa)	Poisson's ratio (*v*)	*K/ G*
Voigt	74.86	129.53	53.45	0.2116	1.40
Reuss	16.80	48.03	23.46	0.0235	0.72
Hill	45.83	90.16	38.46	0.1722	1.19

Table 0.9: The optB86b calculated, bulk, Young's, shear modulus and Poisson's ratio for PtS_2

Averaging scheme	Bulk (*K*) (GPa)	Young's (*E*) (GPa)	Shear (*G*) (GPa)	Poisson's ratio (*v*)	*K*/ *G*
Voigt	77.27	123.45	50.03	0.2337	1.54
Reuss	28.10	62.70	27.79	0.1281	1.01
Hill	52.69	93.67	38.91	0.2037	1.35

The Bulk, shear, Young's moduli and Poisson's ratios were calculated through ELATE [127], a tool for analysis of second-order elastic stiffness tensors. The Voigt-Reuss-Hill approximation, a useful scheme by which anisotropic single crystal elastic constants are converted into isotropic polycrystalline elastic moduli was used for checking accuracy of the calculated *K*, *E*, *G* and *v* values [127].

Pugh proposed that if the *K/G* value is less than the critical 1.75 [150] value, then the material is considered brittle, otherwise it is considered ductile. Ductile materials deform a significant amount before fracture occurs (relatively small Young's modulus). Brittle materials, on the other hand deform elastically prior to fracture by the catastrophic propagation of a crack (relatively large Young's modulus). The apparent fracture toughness of brittle materials can be greatly enhanced via surface-deposited thin films which are under residual and can therefore be used in a variety of technological applications. PtS_2 is a brittle material due to the fact that the *K/G* ratios for all functionals and all averaging schemes were less than 1.75.

3D visualization of the spatial dependence of the Young's modulus illustrates anisotropy within the system as shown in Figure 5.8 below.

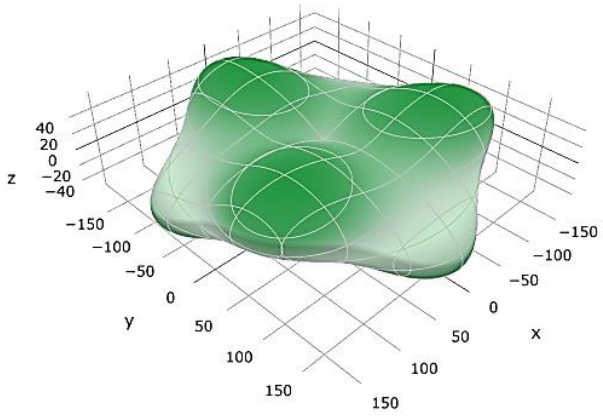

Figure 0.8: Visualization of the spatial dependence of the Young's modulus

The material can withstand changes in length under lengthwise tension or compression in the in-plane (x and y directions) more than out-of-plane (z direction) showing anisotropy within the material. This is also consistent with the understanding that the intra-layer bonding is stronger than the inter-layer bonding.

5.1.4 Dynamical properties of PtS_2

PBE+TS gave the smallest percentage deviation of volume compared to the available experimental data than all the other functionals used in this study. Therefore, phonon studies were conducted using this functional.

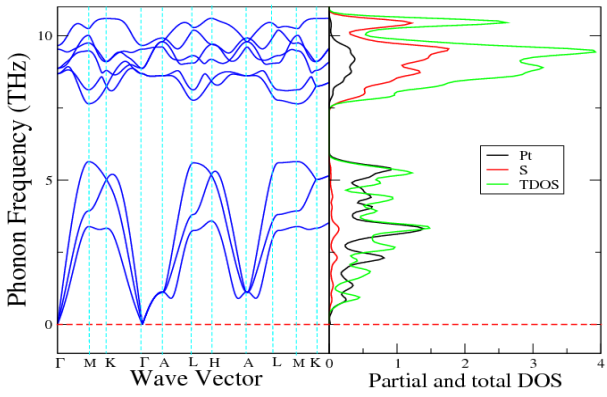

Figure 0.9: PtS_2 Phonon bands, PDOS and TDOS

The phonon frequencies are in the range of 0-12 THz. It is clear that PtS_2 is dynamically stable due to presence of only positive modes of vibrations in the phonon spectra as illustrated in Figure 5.9. The primitive cell of PtS_2 comprises of three atoms, therefore eight independent vibrational modes can be found with three being acoustic modes and the remaining correspond to optical modes. From the partial phonon density of states, the primary element contributing to the acoustic phonon modes is platinum.

5.1.5 Electronic band structure of PtS_2 from DFT, GW and BSE calculations

The results presented above show that PtS_2 is energetically, mechanically and dynamically stable. The lattice parameters as determined by DFT-TS gave a volume closest to the experimental values and were therefore used for the electronic and optical studies. Bandgaps were calculated using the lattice parameters from the relevant different approximations for the sake of comparison. DFT concerns only ground state properties, therefore computing bandgap needs at least an electron in the conduction band, which is an exited state. It is therefore imperative to go beyond DFT for more accurate bandgap approximations [151]. In this study bandgaps were calculated using DFT-PBE, HSE06, MBJ and GW methods.

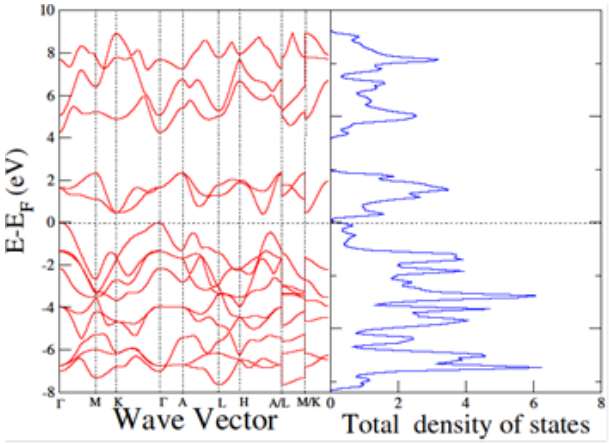

Figure 0.10: PtS_2 electronic band structure and density of states calculated using PBE+TS exchange-correlation functional

PtS_2 band structure was calculated using the PBE+TS approximation lattice parameters. The VBM is located at the Γ point and the CBM is between the H and A/L high symmetry points of the Brillouin zone. Non-occurrence of electronic bands and the Fermi level shown in the band structure and DOS plots in Fig 5.10 illustrates that PtS_2 is an indirect bandgap semiconductor with an approximate fundamental bandgap of approximately 0.54 eV.

Table 0.10: Calculated fundamental bandgaps of bulk PtS_2 using different approximations

Functional	E_g (eV)
LDA	0.2626
PBE	1.5772
PBE+D2	0.1386
PBE+D3	0.2850
PBE+TS	0.5418
PBEsol	0.5119
OptB86b	0.5159
MBJ	0.7591
HSE06	1.1306
Exp[147]	0.95
Exp[152]	0.87
Exp[153]	0.64
Exp[154]	1.2

In general DFT underestimates bandgaps [155] as observed in Table 5.10 above as compared to the experimental bandgaps. HSE hybrid gives much more accurate lattice constants and bandgaps than any standard semilocal functionals including LDA and PBE [59]. From the results LDA, PBE+D2 and PBE+D3 values as illustrated in Table 5.10 underestimates the theoretical bandgap of approximately 0.87 eV [152] obtained through PBE+vdW calculation. The MBJ and HSE functionals overestimated with a

smaller deviation from experimental results. The GW (fundamental) and BSE (optical) bandgaps are more precise. This is due to the fact that the GW and BSE calculations are formally approximations of the fundamental and optical gaps.

DFT, GW and BSE gaps were determined using the Tauc plot for comparison. The Tauc plot is a method that is widely used for the determination of the experimental bandgap from measurements of the dielectric response. The transition type and energy was assessed by fitting the optical absorption spectrum to Tauc models as illustrated in figure 5.11 below. The edge of the absorption is obtained by linear extrapolation of $(h\omega\alpha)^2$ to zero absorption [156].

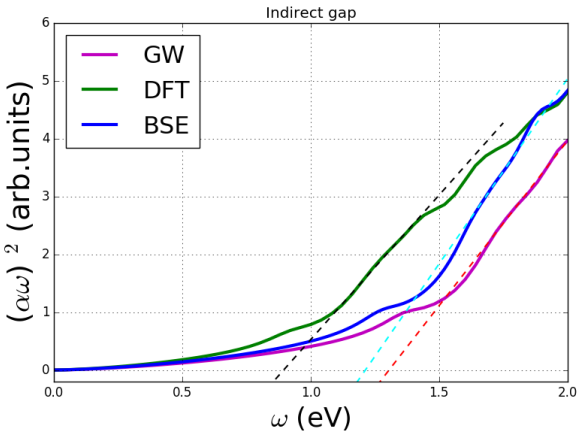

Figure 5.11: PtS_2 DFT, GW and BSE Tauc in-plane bandgaps

From Figure 5.11, the results illustrate that DFT underestimates bandgaps, therefore it is essential to go beyond standard KS DFT methods to predict correctly both bandgaps and optical absorption spectra. Therefore, GW calculation which aims at obtaining accurate quasiparticle energy levels through electron-electron interactions was conducted. The electron-hole excitations were then calculated by solving the BSE which was preceded by the GW and IPA approximations. This then enabled the calculation of the optical absorption spectra [157]. The BSE bandgap is smaller than GW gap due to the fact that in the BSE calculation (attractive) interactions between electrons and holes are included. The obtained approximate indirect in-plane and out-of-plane bandgaps from the Tauc plots are shown below in Table 5.11. The out-of-

plane bandgaps shows a different trend. This anomaly behaviour could have emanated from the fact that the calculation of the tensor elements for the dielectric matrix for the DFT and GW in the approximation we use involves the same products of (DFT) eigen functions when calculating the oscillator strengths. In comparison with BSE, a product of four (DFT) eigen functions contributes to the oscillator strength.

Table 5.111 PtS_2 bandgaps obtained from Tauc fit

Approximation	In-plane (*xy*-plane) E_g (eV)	Out-of-plane (|| *z*-axis) E_g (eV)
DFT	0.89	0.24
GW	1.30	0.24
BSE	1.21	0.20

From Table 5.11, the out-of-plane optical edge absorption strength at 0.20 eV is much smaller than the in-plane optical edge at 1.21 eV. For in-plane, when the photon energy is 1.21 eV, the relative value of alpha is 0.8509. For out-of-plane, when photon energy is 0.2 eV, the relative value of alpha is 0.0314. Therefore, the ratio of the relative absorption

Values is 27:1 for the in-plane to out-of-plane. Hence based on the magnitude of these ratios, we conclude that there is a high chance of observing the absorption spectra for the in-plane than out-of-plane. This probably highlights why the experimental mesurements fail to accurately detect the minimum absorption edge. The experimental value of optical gap of about 1.1 eV [134] is close to what we obtained for in-plane through Tauc fit which strongly supports our estimation.

5.1.6 Optical properties of PtS_2

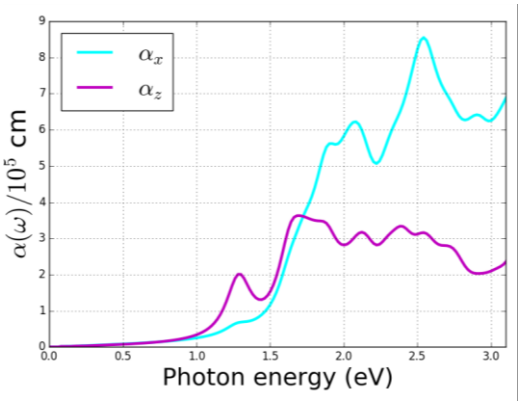

Figure 0.11: PtS_2 absorption coefficient

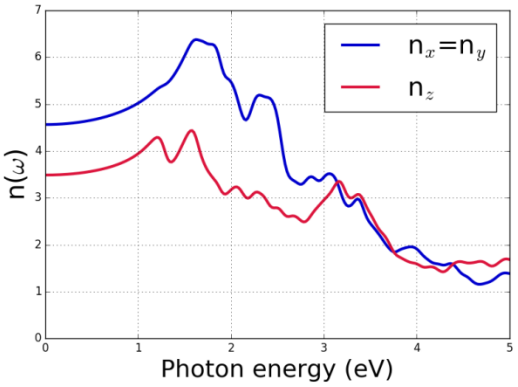

Figure 0.12: PtS_2 refractive index

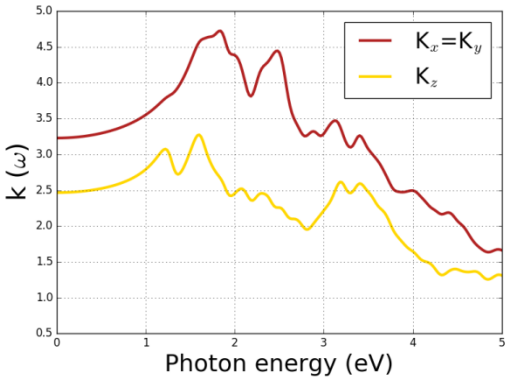

Figure 0.13: PtS_2 extinction coefficient

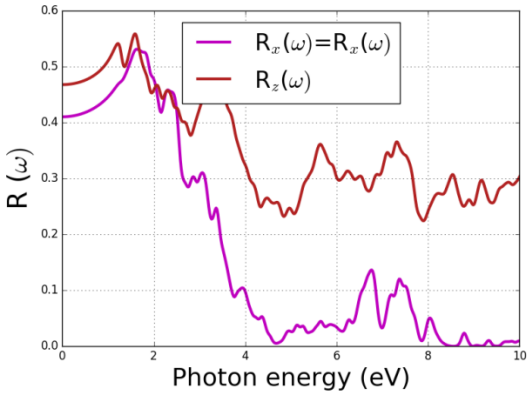

Figure 0.14: PtS_2 reflectivity

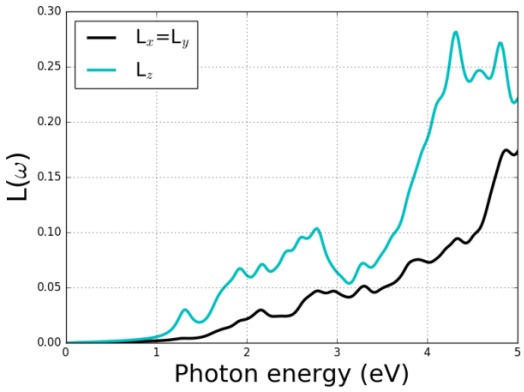

Figure 0.15: PtS_2 energy loss Figure

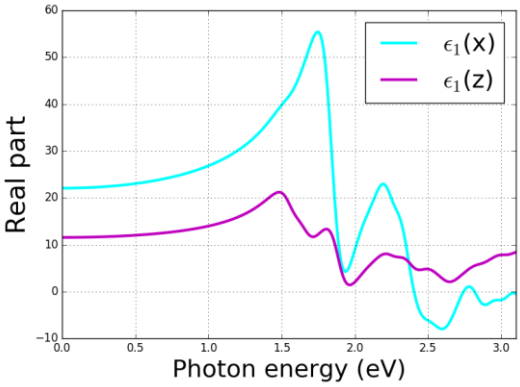

0.16: PtS_2 real dielectric response function

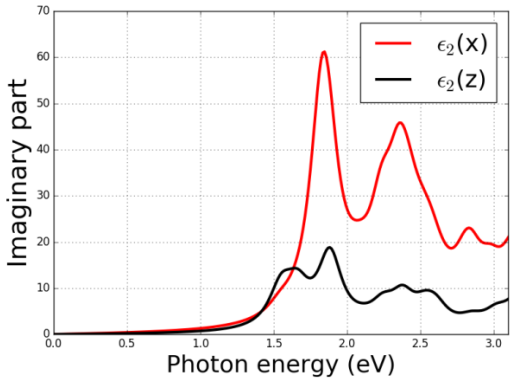

Figure 0.17: PtS_2 imaginary dielectric response function

The BSE dielectric matrix was calculated using GW input data. The calculations were carried out with more focus on the visible range of 1.6 eV-3.1 eV of the electromagnetic spectrum which covers the energy of visible light and incoming photons in the solar radiation. The plot of the absorption coefficient against energy as shown in Figure 5.12 gives a clear picture of the photon energies which are most likely to be absorbed by PtS_2. Decent absorption for photon energies above 1.6 eV was observed. Both in-plane and out-of-plane absorption depicts anisotropy and peaks occurred within the visible range with the in-plane absorption peak at around 2.5 eV and out-of-plane at 1.6 eV.

Maximum refraction, extinction and reflectivity all occur at approximately 1.8 eV for both in and out-of- plane as illustrated in Figures 5.13, 5.14 and 5.15 respectively. Interband transitions illustrated through peaks in reflectivity span the visible and ultraviolet regions. This suggests that light directed to PtS_2 will appear red out-of-plane and green in-plane in colour. Reflectivity, refractive index and extinction coefficient generally shows that in-plane exceeds out-of-plane within the visible region depicting optical anisotropy. Minimum energy losses are observed within the visible range as shown in Figure 5.16. The imaginary part of dielectric function is linked with the energy loss and thus it is responsible for the absorption as seen when comparing Figure 5.12 and Figure 5.18, both in-plane maximum peaks occur at approximately 1.8

eV. In-plane real dielectric response is more than the out-of-plane between 0 eV and 2.4 eV with out-of-plane greater than the in-plane onwards.

5.1.7 Thermal properties of PtS_2

The DFT-TS approximation was also used for the thermal conductivity calculations for the three compounds under this study, PtS_2, $PtSe_2$ and $PtTe_2$ due to reasons stated earlier. Once the phonon frequencies over Brillouin zone are known, the energy of the phonon system can be determined. Using the thermodynamic relations, a number of thermal properties, such as constant volume heat capacity C_v, Helmholtz free energy F, and entropy S, can be computed as functions of temperature [124].

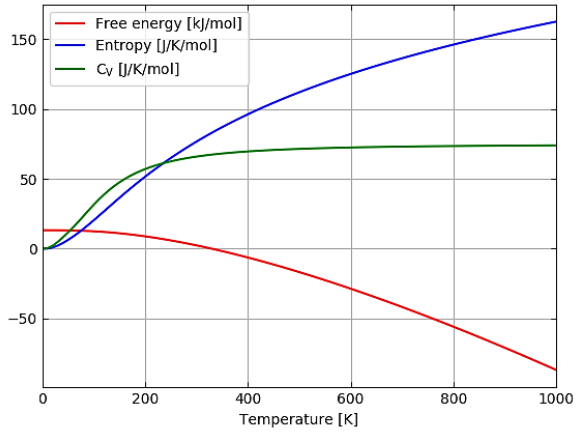

Figure 0.18: PtS_2 temperature dependence of free energy, entropy and C_v

Atoms in a crystal vibrate about their equilibrium positions generating thermal energy. The generated thermal energy increases with an increase in temperature giving the thermal properties of the material. From Figure 5.19 the specific heat C_v, increases with temperature until it reaches a constant value of approximately 72 kJ(mol)$^{-1}$. This value is known as the Dulong-Petit limit [158]. The predicted Helmholtz free energy, specific heat capacity and entropy at 300 K from Figure 5.19 were around 2.3 kJ(mol)$^{-1}$, 65.9 J(K mol)$^{-1}$, and 76.7 J(K mol)$^{-1}$ respectively. The degree of disorder (entropy)

increases with an increase in temperature whilst the capacity of a system to do work (free energy) decreases with an increase in temperature.

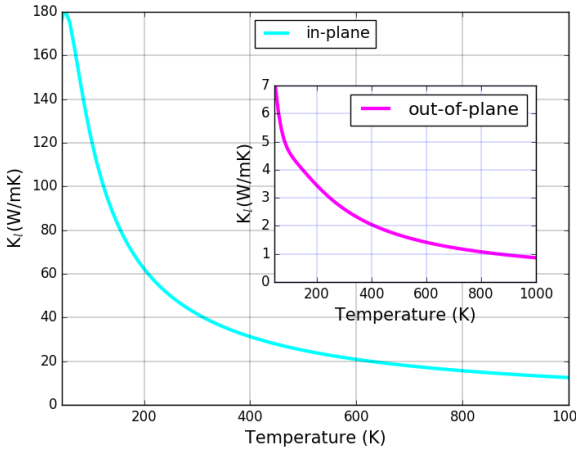

Figure 0.19: PtS_2 lattice thermal conductivity as a function of temperature

From Figure 5.20 it can be observed that both the in-plane and out-of-plane thermal conductivity decreases as temperature increases. The in-plane thermal conductivity is much higher than the out of plane depicting material anisotropy. At 300 K, the projected in-plane and out of plane K_l values are 41.6 W/mK and 2.6 W/mK respectively.

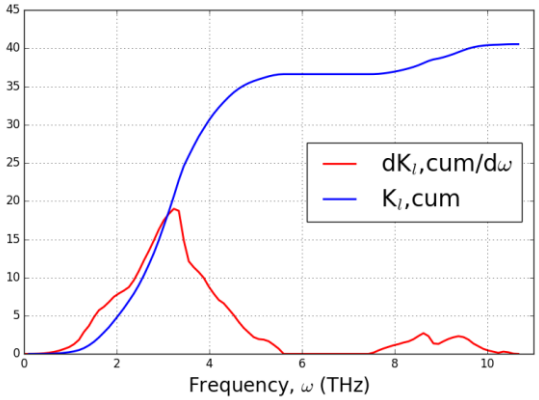

Figure 0.20: PtS_2 in-plane cumulative lattice thermal conductivity and derivative density at 300 K as a function of frequency

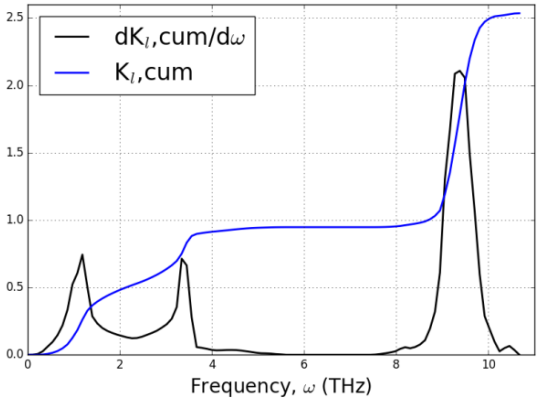

Figure 0.21: PtS_2 out-of-plane cumulative lattice thermal conductivity and derivative density at 300 K as a function of frequency

The in-plane and out-of-plane thermal conductivities with derivative density of states as functions of frequency at 300 K also depicts anisotropy within the material as shown in Figures 5.21 and 5.22. The in-plane cumulative lattice thermal conductivity cum K_l, and its derivative dK_l, corroborate that the main contributor to K_l is acoustic phonon modes due to the fact that there is a significant increase of both of them as frequency increases until the acoustic cut off limit of approximately 5.8 THz. The out-of-plane cum K_l and its derivative dK_l shows that both acoustic and optical modes contribute significantly to K_l. This is unusual because the acoustic phonons are low frequency acoustic branches in which atoms are in phase. While the optical phonons are high frequency branches with atoms out of phase. This is true for the in-plane lattice thermal conductivity, but not for the out-of-plane thermal conductivity. Optical phonons prove to be ineffective as heat transporters due to their low group velocities. However, they interact with the acoustic phonons which are main contributors of the thermal conductivity.

5.2 Platinum diselenide ($PtSe_2$)

The Bravais lattice is hexagonal with a trigonal crystal structure belonging to the space group, $P\bar{3}m1$. As in the case of PtS_2, $PtSe_2$ has only one polymorph.

5.2.1 Equation of state (EOS) for $PtSe_2$

The study of $PtSe_2$ was also conducted with the seven different exhange-correlation functionals discussed in the introduction, namely LDA, PBE, PBEsol, Grimme DFT-D2, DFT-D3, Tkatchenko-Scheffler (DFT-TS) and optB86b-vdW. The energy versus volume EOS for $PtSe_2$ obtained using different functionals are given below.

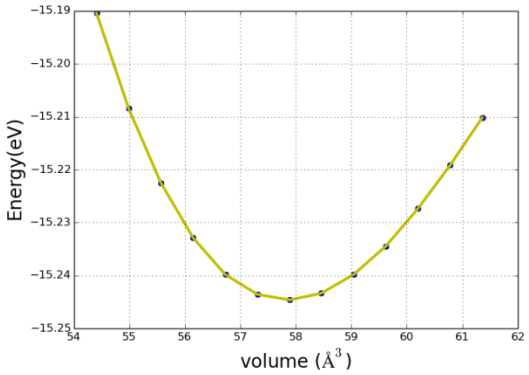

Figure 0.22: LDA

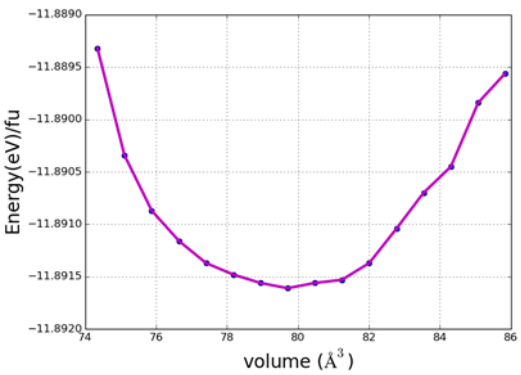

Figure 0.23: PBE

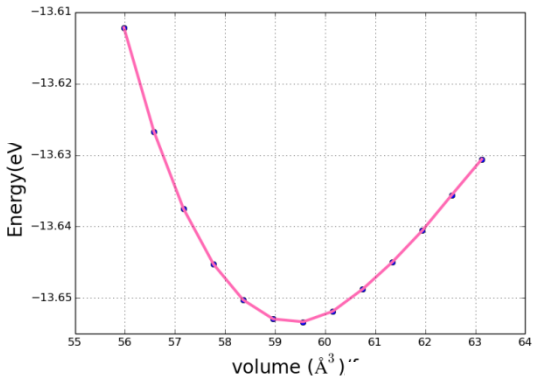

Figure 0.24: PBEsol

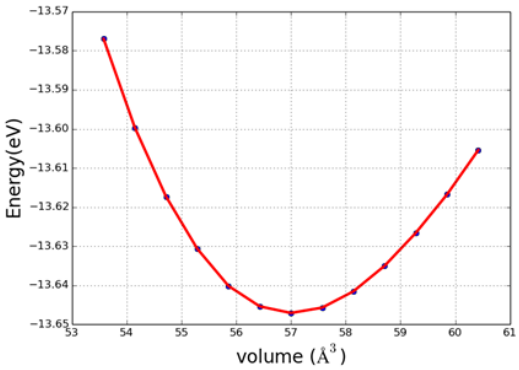

Figure 0.25: PBE+D2

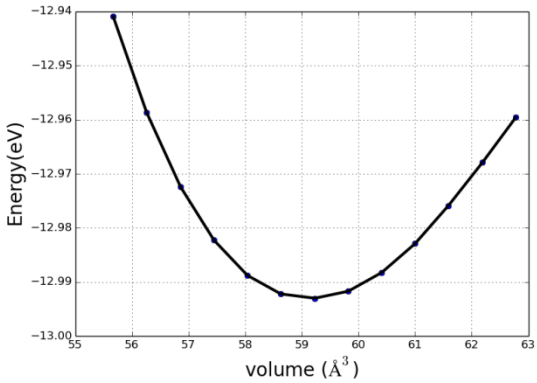

Figure 0.26: PBE+D3

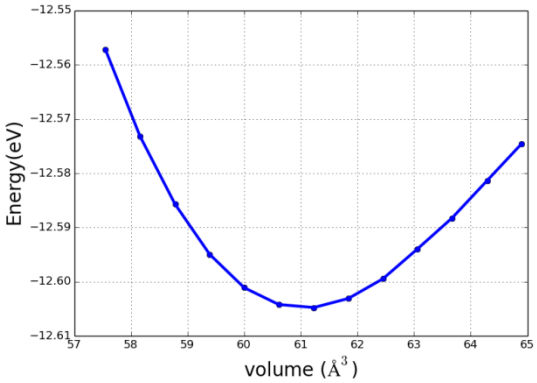

Figure 0.27: PBE+TS

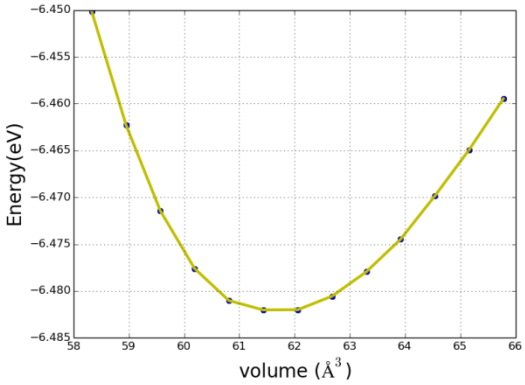

Figure 0.28: optB86b

Optimization at fixed volume set was done using the above different functionals in order to ascertain the one which correctly imitated the structural properties of $PtSe_2$ at equilibrium volume. The trend observed had PBE giving the highest and PBE+D2 the lowest value of equilibrium volume respectively. It is evident that PBE functional fails to account for the interlayer van der Waals dispersion forces.

5.2.2 Structural and energetic properties of $PtSe_2$

Table 0.12: The equilibrium structural and energetic properties for $PtSe_2$ calculated using various exchange-correlation functionals. The experimental structural properties are also shown for comparison

Functional	$a = b$(Å)	c(Å)	V_0(Å)^3	E_{coh} (eV/atom)	E_{form} (eV/atom)
LDA	3.747	4.769	57.986	-5.082	-0.479
PBE	3.750	6.481	79.052	-3.964	-0.395
PBE+D2	3.768	4.640	57.034	-4.728	-0.980
PBE+D3	3.784	4.767	59.112	-4.331	-0.762
PBE+TS	3.805	4.869	61.049	-4.022	-0.453
PBEsol	3.761	4.848	59.328	-4.550	-0.980
OptB86b	3.780	4.991	61.683	-2.161	-0.702
Exp[14]	3.728	5.081	61.15	-	-
Exp[159]	3.7278	5.0183	60.39	-	-
Exp[148]	3.7278	5.0813	61.152	-	-

PBE+TS functional reproduced the best results with accuracy within 1.1% of the available experimental results as illustrated in Table 5.12. PBE does not describe the dispersive van der Waals interactions, which gives more than 29% overestimation of the experimental equilibrium volume. Compared with the bare PBE, the PBE+vdW gives improved out-of-plane values of the lattice parameters because it corrects the out-of-plane lattice parameters to smaller values. The optB86b-vdW functional gave lattice parameters which were more comparable to the experimental data. Negative cohesive and formation energies imply that the compound is stable against decomposition into constituent atoms and constituent solid components.

5.2.3 Mechanical properties of $PtSe_2$

Table 0.13: Calculated values of independent elastic coefficients for $PtSe_2$

Functional	C_{11} (GPa)	C_{12}(GPa)	C_{13}(GPa)	C_{33}(GPa)	C_{44}(GPa)
LDA	205.58	66.15	43.24	66.45	44.89
PBE	115.75	31.33	2.15	0.15	1.53
PBE+D2	244.03	76.92	52.61	76.94	62.14
PBE+D3	190.63	59.06	35.59	53.08	40.82
PBE+TS	173.54	55.53	34.75	53.44	39.85
PBEsol	189.9	62.97	35.76	44.23	39.20
optB86b	177.01	57.83	34.19	37.08	34.16

The six eigenvalues of the elastic tensor were all positive indicating mechanical stability of the system for all functionals used. All the eigenvalues of all the compounds in this study are given in appendix A. As seen earlier for PtS_2, the calculated results for $PtSe_2$ also satisfied the Born stability criteria for mechanical stability for hexagonal and trigonal systems.

Table 0.14: The LDA calculated, bulk, Young's, shear modulus and Poisson's ratio for $PtSe_2$

Averaging scheme	Bulk (K) (GPa)	Young's (E) (GPa)	Shear (G) (GPa)	Poisson's ratio (v)	K/G
Voigt	86.98	133.33	53.57	0.2445	1.62
Reuss	61.80	96.53	38.93	0.2397	1.59
Hill	74.39	114.93	46.25	0.2425	1.61

Table 0.15: The PBE calculated, bulk, Young's, shear modulus and Poisson's ratio for $PtSe_2$

Averaging scheme	Bulk (*K*) (GPa)	Young's (*E*) (GPa)	Shear (*G*) (GPa)	Poisson's ratio (*v*)	*K/ G*
Voigt	33.66	54.43	22.12	0.2304	1.52
Reuss	0.09	0.41	0.28	-0.2707	0.32
Hill	16.87	27.51	11.20	0.2283	1.51

Table 0.16: The PBE+D2 calculated, bulk, Young's, shear modulus and Poisson's ratio for $PtSe_2$

Averaging scheme	Bulk (*K*) (GPa)	Young's (*E*) (GPa)	Shear (*G*) (GPa)	Poisson's ratio (*v*)	*K/ G*
Voigt	103.25	165.44	67.09	0.2330	1.54
Reuss	72.46	120.40	49.22	0.2231	1.47
Hill	87.86	142.93	58.16	0.2289	1.51

Table 0.17: The PBE+D3 calculated, bulk, Young's, shear modulus and Poisson's ratio for $PtSe_2$

Averaging scheme	Bulk (*K*) (GPa)	Young's (*E*) (GPa)	Shear (*G*) (GPa)	Poisson's ratio (*v*)	*K/ G*
Voigt	77.19	122.87	49.76	0.2347	1.55
Reuss	50.16	86.52	35.68	0.2125	1.41
Hill	63.68	104.73	42.72	0.2259	1.49

Table 0.18: The PBE+TS calculated, bulk, Young's, shear modulus and Poisson's ratio for $PtSe_2$

Averaging scheme	Bulk (*K*) (GPa)	Young's (*E*) (GPa)	Shear (*G*) (GPa)	Poisson's ratio (*v*)	*K/ G*
Voigt	72.29	107.45	42.90	0.2523	1.69
Reuss	49.89	77.49	31.22	0.2411	1.60
Hill	61.09	92.48	37.06	0.2477	1.65

Table 0.19: The PBEsol calculated, bulk, Young's, shear modulus and Poisson's ratio for $PtSe_2$

Averaging scheme	Bulk (*K*) (GPa)	Young's (*E*) (GPa)	Shear (*G*) (GPa)	Poisson's ratio (*v*)	*K/ G*
Voigt	77.00	118.56	47.67	0.2434	1.61
Reuss	43.51	77.43	32.17	0.2034	1.35
Hill	60.25	98.10	39.92	0.2286	1.51

Table 0.20: The optB86b calculated, bulk, Young's, shear modulus and Poisson's ratio for $PtSe_2$

Averaging scheme	Bulk (*K*) (GPa)	Young's (*E*) (GPa)	Shear (*G*) (GPa)	Poisson's ratio (*v*)	*K/ G*
Voigt	71.50	107.96	43.24	0.2483	1.65
Reuss	36.98	64.32	26.58	0.2101	1.39
Hill	54.24	86.23	34.91	0.2350	1.55

$PtSe_2$ is also a brittle material due to the fact that the *K/G* ratios for all functionals and all averaging schemes were less than 1.75.

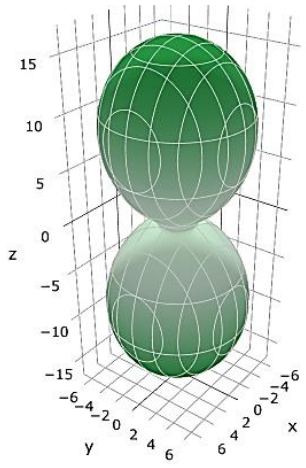

Figure 0.29: Linear compressibility of $PtSe_2$

The relative change in the volume of $PtSe_2$ produced by unit compressive or tensile stress acting uniformly over its surface also depicts anisotropy between the in-plane and out-of-plane as illustrated in Figure 5.30.

5.2.4 Dynamical properties of $PtSe_2$

Further dynamical stability studies were conducted using PBE+TS since it mimicked experimental volume of $PtSe_2$ with the best accuracy percentage when compared to other exchange-correlation functionals used during this study.

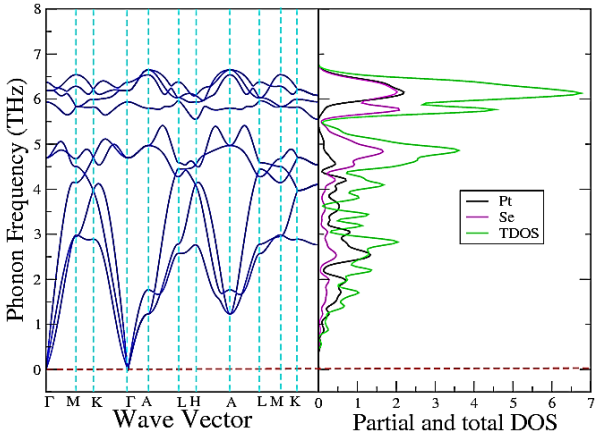

Figure 0.30: $PtSe_2$ Phonon bands, PDOS and TDOS

$PtSe_2$ is dynamically stable due to the existence of only positive modes of vibrations in the phonon bands and TDOS within the range of 0-7 THz as illustrated in Figure 5.3.1. Like PtS_2 the primitive cell of $PtSe_2$ also contains three atoms. Therefore, eight independent vibrational modes can be found in which three are acoustic and the remaining corresponding to optical modes. Compared to PtS_2 which has a significant energy gap between acoustic and optical branches which protects the vibration of acoustic modes from being scattered by optical phonon modes, $PtSe_2$ has a very small energy gap.

5.2.5 Electronic properties of $PtSe_2$ from DFT, GW and BSE calculations

The lattice parameters as determined by DFT-TS gave a volume closest to the experimental values and were therefore used for the electronic and optical studies. Bandgaps were calculated using the lattice parameters from the relevant different approximations. $PtSe_2$ is a semimetal with a slight indirect overlap of the conduction and valence bands. As earlier stated it is imperative to go beyond DFT for more accurate bandgap approximations [151]. In this study bandgaps were calculated using DFT-PBE, HSE06, MBJ, GW and BSE methods.

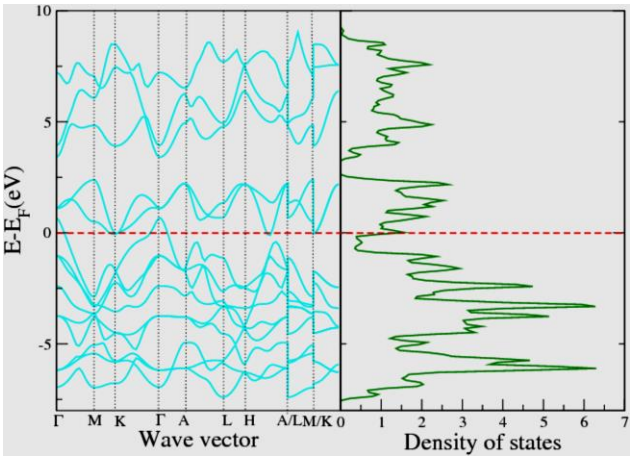

Figure 0.31: $PtSe_2$ electronic band structure and density of states calculated using PBE+TS exchange-correlation functional

$PtSe_2$ band structure was calculated using the PBE+TS approximation lattice parameters. Fig 5.32 illustrates that $PtSe_2$ has an overlap of the VBM and CBM. The VBM occurs at the Γ point and the CBM is located between the H and A/L points of the Brillouin zone. Bulk $PtSe_2$ has a finite number of energy bands crossing the Fermi level, indicating it is metallic with an indirect overlap of the conduction and valence bands consistent with previous theoretical and experimental studies [14][40].

Table 0.21: Calculated fundamental bandgaps of bulk $PtSe_2$ using different approximations

Functional	E_g (eV)
LDA	0.0000
PBE	0.0000
PBE+D2	0.0000
PBE+D3	0.0000
PBE+TS	0.0000
PBEsol	0.0000
OptB86b	0.0000
MBJ	0.0000
HSE06	0.0000
Exp[145]	0.10
Exp[108]	0.18

At DFT level the fundamental bandgap for bulk $PtSe_2$ is zero as illustrated in Table 5.21. This indicates that $PtSe_2$ is metallic at DFT level. As discussed earlier, generally DFT underestimates bandgaps while generalised DFT sometimes gives better results. The obtained approximate indirect in-plane and out-of-plane bandgaps from the Tauc fit are shown below in Table 5.22.

Table 5.22: $PtSe_2$ bandgaps obtained from Tauc fit

Approximation	In-plane (*xy*-plane)	Out-of-plane (‖ *z*-axis)
	E_g (eV)	E_g (eV)
DFT	0.15	0.30
GW	0.16	0.59
BSE	0.15	0.55

The in-plane and out-of-plane the minimum bandgaps changes as explained in section 5.1.5 as we move from DFT to GW and BSE. For in-plane, when the photon energy is 0.15 eV, the relative value of alpha is 0.047. For out-of-plane, when photon energy is 0.55 eV, the relative value of alpha is 0.3299. Therefore, the ratio of the relative absorption values is 1:7 for the in-plane to out-of-plane. Hence based on the magnitude of these ratios, we conclude that there is a high chance of observing the absorption spectra for the out-of-plane than in-plane.

5.2.6 Optical properties of $PtSe_2$

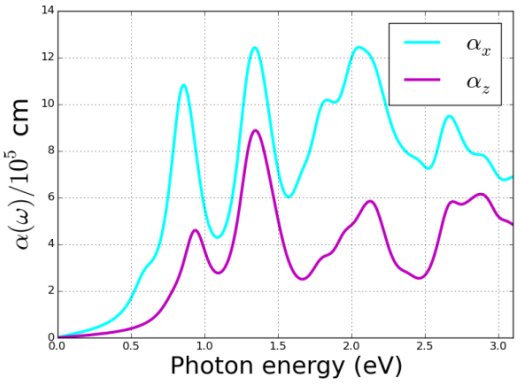

Figure 0.32: $PtSe_2$ absorption coefficient

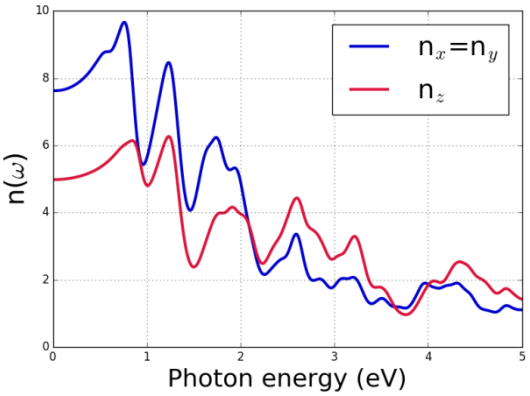

Figure 0.33: $PtSe_2$ refractive index

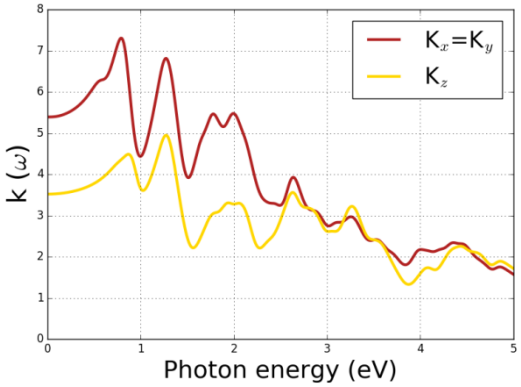

Figure 0.34: $PtSe_2$ extinction coefficient

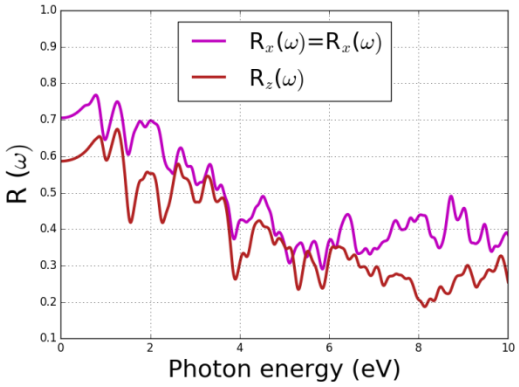

Figure 0.35: $PtSe_2$ reflectivity

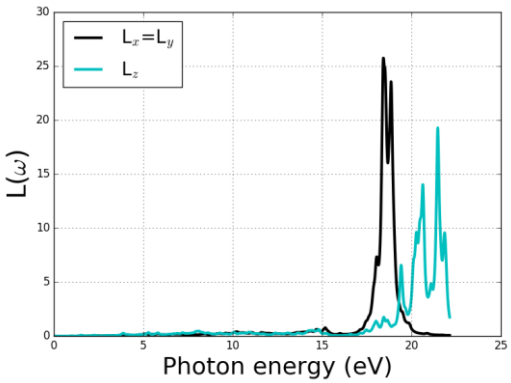

Figure 0.36: $PtSe_2$ loss factor

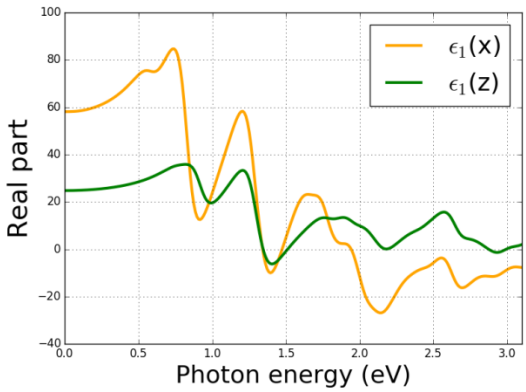

Figure 0.37: $PtSe_2$ real dielectric response function

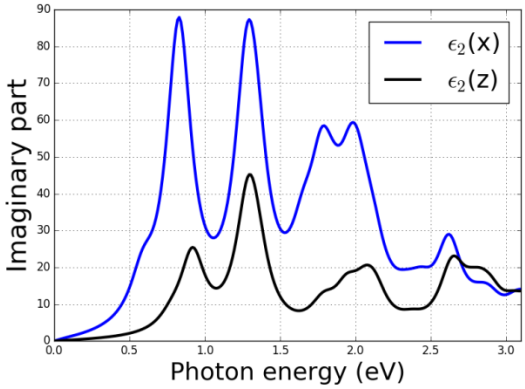

Figure 0.38: $PtSe_2$ imaginary dielectric response function

The BSE dielectric matrix was also calculated using GW input data. In-plane optical absorption supersedes out-of-plane absorption in the energy range, 1.6 eV-3 eV as shown in Figure 5.33. In-plane absorption peaks occur around 0.9 eV, 1.3 eV, 2.1 eV and 2.9 eV with out-of-plane peaks taking place within 0.1 eV range of the in-plane peaks. $PtSe_2$ will appear yellow within the visible range when photons are incident along the x-axis, y-axis and violet along the z-axis depicting optical anisotropy.

In-plane maximum refraction and extinction occurs approximately at the same energy of 0.8 eV and out-of-plane both occurring around 1.3 eV, which is outside the visible range as illustrated in Figures 5.34 and 5.35 respectively. Generally maximum reflectivity, extinction and refraction takes place at low photon energies (< 1eV). Optical energy loss peaks approximately 18 eV and 22 eV in-plane and out-of-plane respectively as shown in Figure 5.37 illustrating the occurrence of maximum plasma oscillation within the ultraviolet region. The electron energy loss function is also proportional to the inverse of dielectric function and corresponds to the collective excitations of electrons of system.

The material possesses optical anisotropy as illustrated in Figures 5.33 to 5.39 above. Both the real and imaginary dielectric response functions peaks range from approximately 0.75 eV to 2.6 eV as shown in Figures 5.38 and 5.39 respectively spanning the infrared and visible regions of the electromagnetic spectrum. Calculations of the imaginary part of the dielectric function of an anisotropic solid in

the region of a critical point are used to obtain the real part of the dielectric constant through Kramers-Kronig relations [160].

5.2.7 Thermal properties of $PtSe_2$

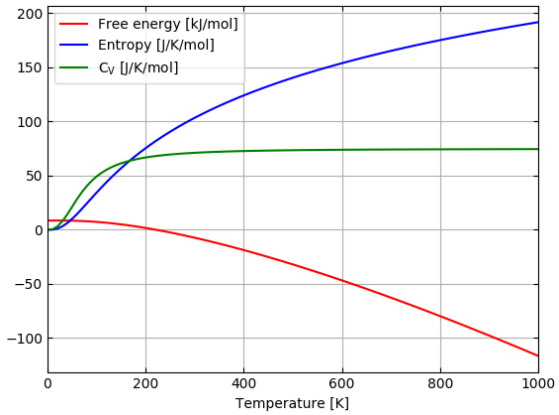

Figure 0.40: $PtSe_2$ Calculated temperature dependence of free energy, entropy and C_v

The projected Helmholtz free energy, specific heat capacity and entropy at 300 K were around -7.40 kJ(mol^{-1}), 71.06 J(mol K)$^{-1}$, and 103.36 J(mol K)$^{-1}$ respectively as shown in Figure 5.40. The Dulong-Petit limit reached at high temperature was about 74 J(mol K)$^{-1}$.

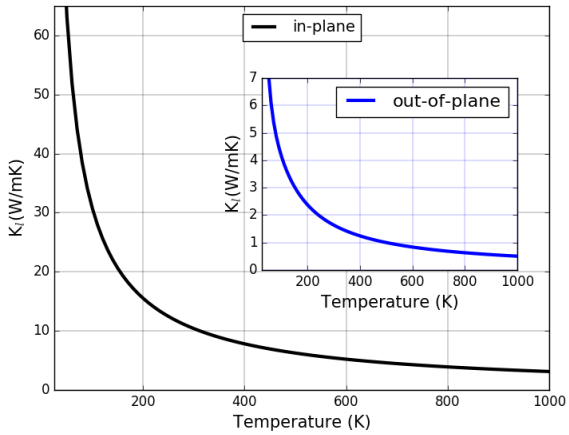

Figure 0.41: $PtSe_2$ lattice thermal conductivity as a function of temperature

From Figure 5.41 it can be observed that both the in-plane and out-of-plane thermal conductivity decreases as temperature increases. The in-plane thermal conductivity is greater than the out-of-plane illustrating anisotropy within the material. The in-plane and out-of-plane K_l values are 10.39 W/mK and 1.64 W/mK at 300 K respectively.

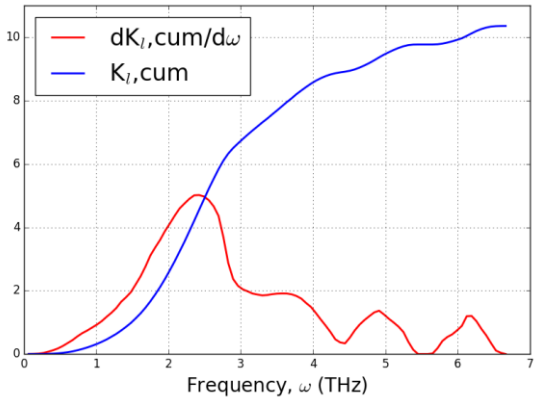

Figure 0.42: $PtSe_2$ in-plane cumulative lattice thermal conductivity and derivative density at 300 K as a function of frequency

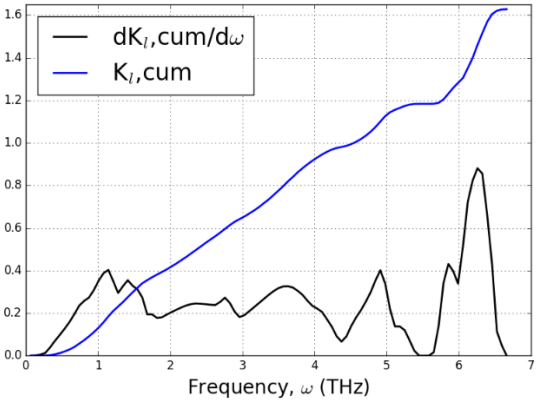

Figure 0.393: $PtSe_2$ out-of-plane cumulative lattice thermal conductivity and derivative density at 300 K as a function of frequency.

The in-plane and out-of-plane cumulative lattice thermal conductivities with derivative density of states as functions of frequency at 300 K also show anisotropy within the material as illustrated in Figure 5.41. The in-plane cumulative lattice thermal conductivity cum K_l, and its derivative dK_l, also support that the main contributor to K_l

is the acoustic phonon modes as shown in Figures 5.42 and 5.43. The out-of-plane cum K_l and its derivative dK_l shows that both acoustic and optical modes contribute towards the K_l.

5.3 Platinum ditelluride ($PtTe_2$)

$PtTe_2$, like the two previous systems has one polymorph, a trigonal crystal structure belonging to the space group, $P\bar{3}m1$.

5.3.1 Equation of state for Platinum ditelluride ($PtTe_2$)

The study of $PtTe_2$ was also conducted with the seven exhange-correlation functionals discussed in the introduction, namely LDA, PBE, PBEsol, Grimme DFT-D2, DFT-D3, Tkatchenko-Scheffler (DFT-TS) and optB86b-vdW. The energy versus volume EOS for $PtTe_2$ obtained using different functionals are given below.

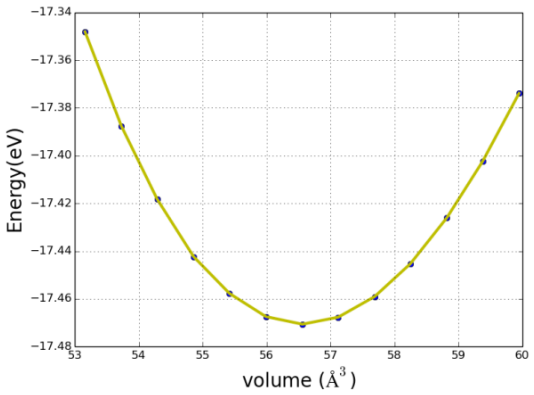

Figure 0.404: LDA

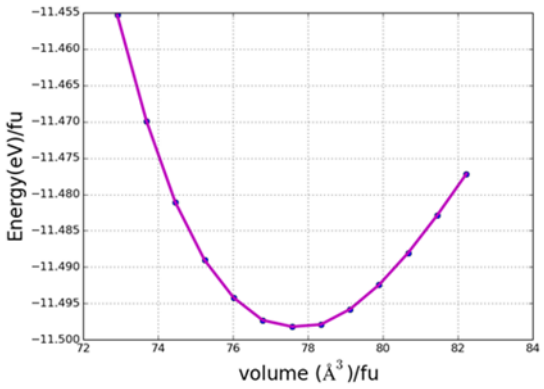

Figure 0.415: PBE

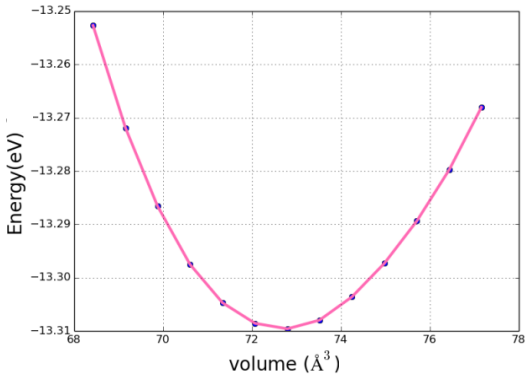

Figure 0.426: PBEsol

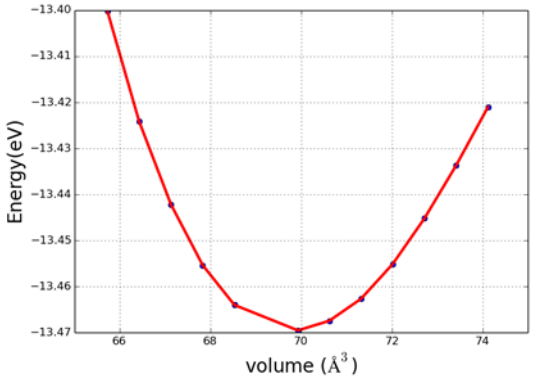

Figure 0.437: PBE+D2

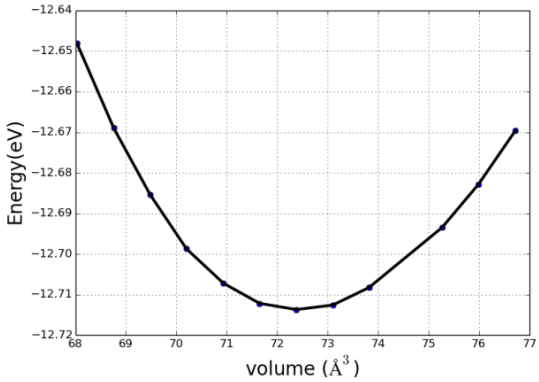

Figure 0.448: PBE+D3

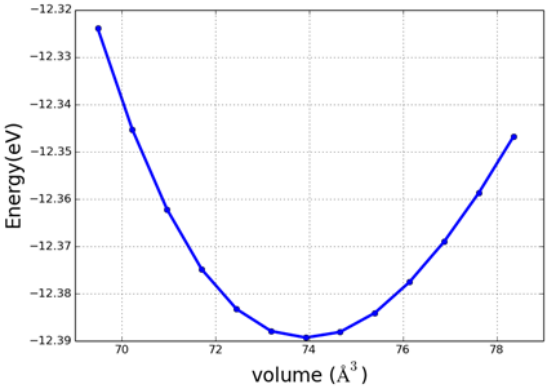

Figure 0.49: PBE+TS

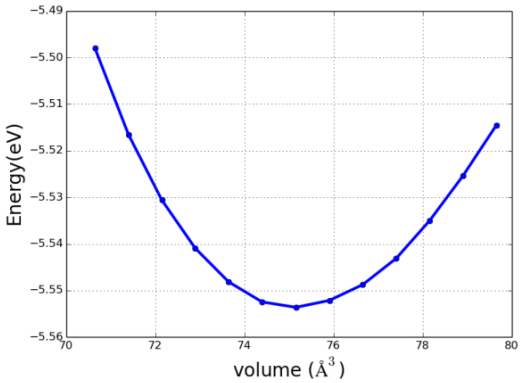

Figure 0.450: optB86b

The observed trend in equilibrium volume obtained for LDA, PBE+D2, PBE+D3, and PBEsol functionals were shifted towards the left of PBE+TS while for PBE and optB86b were shifted towards the right of PBE+TS as observed in Figures 5.44 to 5.50.

5.3.2 Structural and energetic properties of $PtTe_2$

Table 0.22: The equilibrium structural and energetic properties for $PtTe_2$ calculated using various exchange-correlation functionals. The experimental structural properties are also shown for comparison.

Functional	$a = b$(Å)	c(Å)	V_0(Å)^3	E_{coh} (eV/atom)	E_{form} (eV/atom)
LDA	3.850	4.411	56.622	-5.821	-1.319
PBE	4.091	5.360	77.641	-3.832	-0.396
PBE+D2	4.021	4.974	69.780	-4.487	-1.050
PBE+D3	4.072	5.048	72.428	-4.236	-0.799
PBE+TS	4.090	5.101	73.923	-4.128	-0.691
PBEsol	4.048	5.131	72.691	-4.430	-0.987
OptB86b	4.069	5.232	75.158	-1.852	-0.381
Exp[14]	4.026	5.222	73.302	-	-
Exp[159]	4.026	5.221	73.288	-	-
Exp[148]	4.0259	5.2209	73.283	-	-

It is still evident that PBE functional fails to account for the interlayer van der Waals dispersion forces as it overestimated the experimental equilibrium volume by 5.9% as shown in Table 5.22. LDA underestimated by the highest percentage of 22.8%. PBE+TS gave the smallest marginal experimental equilibrium volume error of 0.9%, therefore further electronic, optical and thermal property studies were conducted using PBE+TS exchange-correlation functional. The optB86b-vdW functional as previously observed gave lattice parameters which were more comparable to the experimental data. The negative formation energy also indicated energetic stability of the compound.

5.3.3 Mechanical properties of $PtTe_2$

Table 0.23: Calculated values of independent elastic coefficients for $PtTe_2$

Functional	C_{11}(GPa)	C_{12}(GPa)	C_{13}(GPa)	C_{33}(GPa)	C_{44}(GPa)
LDA	248.78	131.51	145.74	175.26	71.54
PBE	141.58	44.73	22.48	26.88	23.00
PBE+D2	194.11	58.34	51.84	77.72	63.27
PBE+D3	169.00	50.92	46.81	75.75	49.29
PBE+TS	167.17	48.45	39.31	66.19	42.80
PBEsol	164.72	57.55	39.25	61.07	42.68
optB86b	160.06	58.32	43.91	63.76	39.98

Analysis of the elastic tensor through ELATE gave positive eigenvalues indicating mechanical stability of the system for all the functionals used.

Table 0.24: The LDA calculated, bulk, Young's, shear modulus and Poisson's ratio for $PtTe_2$

Averaging scheme	Bulk (K) (GPa)	Young's (E) (GPa)	Shear (G) (GPa)	Poisson's ratio (v)	K/G
Voigt	168.76	153.69	57.00	0.3482	2.96
Reuss	163.47	83.16	29.38	0.4152	5.56
Hill	166.11	119.23	43.19	0.3804	3.84

Table 0.25: The PBE calculated, bulk, Young's, shear modulus and Poisson's ratio for $PtTe_2$

Averaging scheme	Bulk (*K*) (GPa)	Young's (*E*) (GPa)	Shear (*G*) (GPa)	Poisson's ratio (*v*)	*K/ G*
Voigt	54.38	83.53	33.58	0.2440	1.62
Reuss	26.62	51.12	21.66	0.1800	0.52
Hill	40.50	67.51	27.62	0.2222	1.47

Table 0.26: The PBE+D2 calculated, bulk, Young's, shear modulus and Poisson's ratio for $PtTe_2$

Averaging scheme	Bulk (*K*) (GPa)	Young's (*E*) (GPa)	Shear (*G*) (GPa)	Poisson's ratio (*v*)	*K/ G*
Voigt	87.78	144.90	59.15	0.2249	1.48
Reuss	71.04	104.40	41.59	0.2551	1.71
Hill	79.41	124.74	50.37	0.2382	1.58

Table 0.27: The PBE+D3 calculated, bulk, Young's, shear modulus and Poisson's ratio for $PtTe_2$

Averaging scheme	Bulk (*K*) (GPa)	Young's (*E*) (GPa)	Shear (*G*) (GPa)	Poisson's ratio (*v*)	*K/ G*
Voigt	78.10	122.54	49.47	0.2385	1.58
Reuss	66.66	95.62	37.92	0.2609	1.76
Hill	72.38	109.12	43.70	0.2487	1.66

Table 0.28: The PBE+TS calculated, bulk, Young's, shear modulus and Poisson's ratio for $PtTe_2$

Averaging scheme	Bulk (*K*) (GPa)	Young's (*E*) (GPa)	Shear (*G*) (GPa)	Poisson's ratio (*v*)	*K/ G*
Voigt	72.74	116.47	47.23	0.2331	1.54
Reuss	58.61	89.52	35.94	0.2454	1.63
Hill	65.68	103.01	41.58	0.2386	1.58

Table 0.29: The PBEsol calculated, bulk, Young's, shear modulus and Poisson's ratio for $PtTe_2$

Averaging scheme	Bulk (*K*) (GPa)	Young's (*E*) (GPa)	Shear (*G*) (GPa)	Poisson's ratio (*v*)	*K/ G*
Voigt	73.62	111.64	44.75	0.2473	1.65
Reuss	55.99	87.39	35.24	0.2398	1.59
Hill	64.81	99.52	40.00	0.2441	1.62

Table 0.30: The optB86b calculated, bulk, Young's, shear modulus and Poisson's ratio for $PtTe_2$

Averaging scheme	Bulk (K) (GPa)	Young's (E) (GPa)	Shear (G) (GPa)	Poisson's ratio(*v*)	K/ G
Voigt	75.13	106.25	42.02	0.2643	1.79
Reuss	59.13	83.13	32.84	0.2657	1.80
Hill	67.13	94.69	37.43	0.2649	1.79

The *K/G* ratios for the different exchange-correlation functionals range between 0.52 and 5.56 using the Voigt, Reuss and Hill averaging schemes. Being isostructural it probably highlights the fact that $PtTe_2$ is a mechanically anisotropic ductile material.

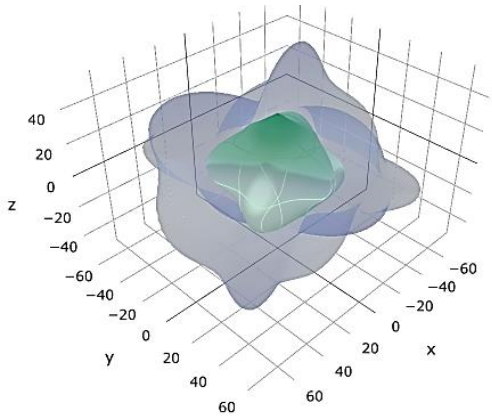

Figure 0.461: $PtTe_2$ shear modulus

The material's response to shear stress shown in Figure 5.51 shows in-plane and out-of-plane anisotropy.

5.3.4 Dynamical properties of $PtTe_2$

Dynamical properties of $PtTe_2$ were done using the PBE+TS exchange-correlation functional.

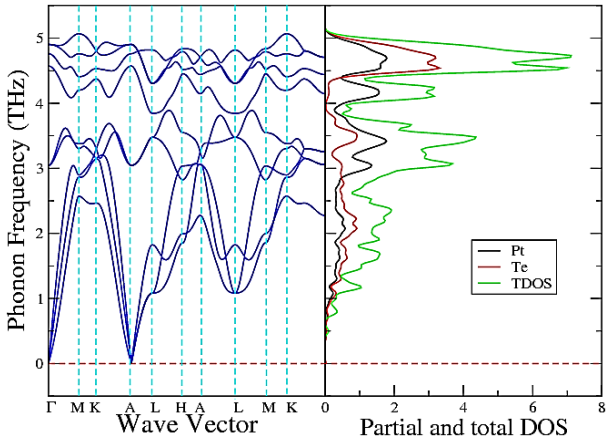

Figure 0.472: $PtTe_2$ phonon bands, PDOS and TDOS

$PtTe_2$ is dynamically stable due to the existence of only positive phonon modes of vibrations in the phonon bands and TDOS within the range of 0-5 THz as shown in

Figure 5.52 above. Like the two previous compounds under investigation, $PtTe_2$ primitive cell contains three atoms and eight independent vibrational modes can be observed in which three are acoustic and the remaining representing optical modes. Compared to the two previous materials $PtTe_2$ has an overlap between the acoustic and optical branches.

5.3.5 Electronic properties of $PtTe_2$ from DFT, GW and BSE calculations

The lattice parameters as determined by DFT-TS gave a volume closest to the experimental values and were also used for the electronic and optical studies. Bandgaps were calculated using the lattice parameters from the relevant different approximations for comparison. Same as in the bandgap calculations for PtS_2 and $PtSe_2$ bandgaps for $PtTe_2$ were calculated using DFT-PBE, HSE06, MBJ and GW methods are shown in Table 5.31 below.

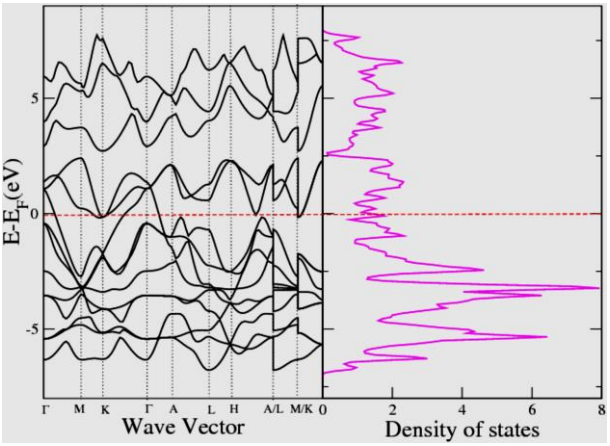

Figure 0.483: $PtTe_2$ electronic band structure and density of states calculated using PBE+TS exchange-correlation functional

$PtTe_2$ band structure was calculated using the PBE+TS approximation lattice parameters as well. Fig 5.53 illustrates that $PtTe_2$ has an overlap of the VBM and CBM located at the M and K high symmetry points in the Brillouin zone respectively. Bulk

$PtTe_2$ has a number of energy bands crossing the Fermi level indicating its metallic properties.

Table 0.31: Calculated fundamental bandgaps of bulk $PtTe_2$ using different approximations

Functional	E_g (eV)
LDA	0.0000
PBE	0.0000
PBE+D2	0.0000
PBE+D3	0.0000
PBE+TS	0.0000
PBEsol	0.0000
OptB86b	0.0000
MBJ	0.0000
HSE06	0.0000
Exp[154]	Metallic

The DFT based calculations gave zero fundamental bandgaps at DFT level illustrating that the compound is metallic as illustrated in Table 5.31. This reflects a problem with DFT approximations in that the presence or absence of a bandgap is not reliably identified [139][161]. Below are the bandgap results obtained from the Tauc fit.

Table 322: $PtTe_2$ bandgaps obtained from Tauc fit

Approximation	In-plane (*xy*-plane) E_g (eV)	Out-of-plane (|| *z*-axis) E_g (eV)
DFT	0.16	0.76
GW	0.42	0.30
BSE	0.19	0.34

The explanation for the above trends in the in-plane and out-of-plane bandgaps was previously discussed in section 5.1.5.

From Table 5.32, the out-of-plane optical edge absorption strength at 0.34 eV is bigger than the in-plane optical edge at 0.19 eV. For in-plane, when the photon energy is 0.19 eV, the relative value of alpha is 0.4345. For out-of-plane, when photon energy is 0.34 eV, the relative value of alpha is 0.2949.

Therefore, the ratio of the relative absorption values is 1.5:1 for the in-plane to out-of-plane. Hence based on the magnitude of these ratios, we conclude that there is a slightly higher chance of observing the absorption spectra for the in-plane than out-of-plane.

5.3.6 Optical properties of $PtTe_2$

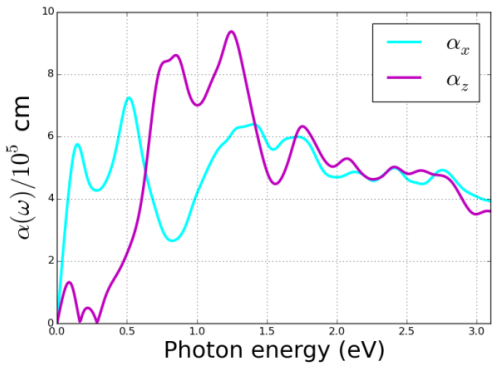

Figure 0.494: $PtTe_2$ absorption coefficient

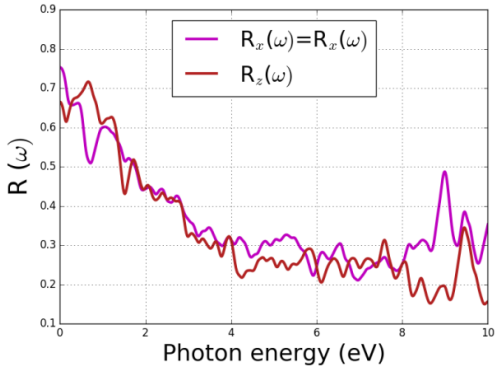

Figure 0.505: $PtTe_2$ reflectivity

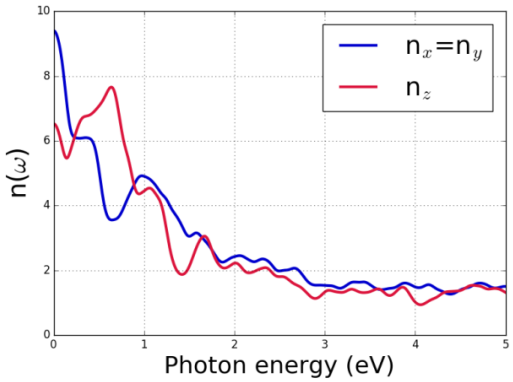

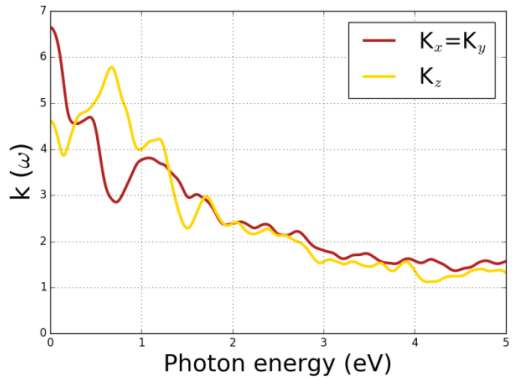

Figure 0.516: $PtTe_2$ refractive index

Figure 0.527: $PtTe_2$ extinction coefficient

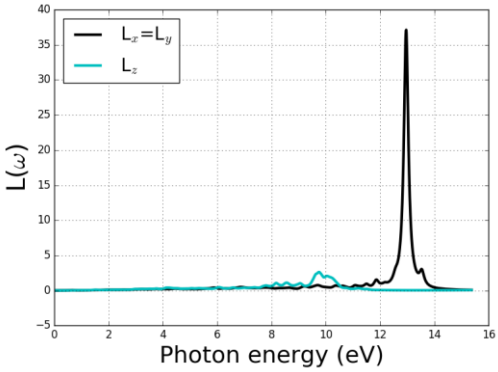

Figure 0.538: $PtTe_2$ loss factor

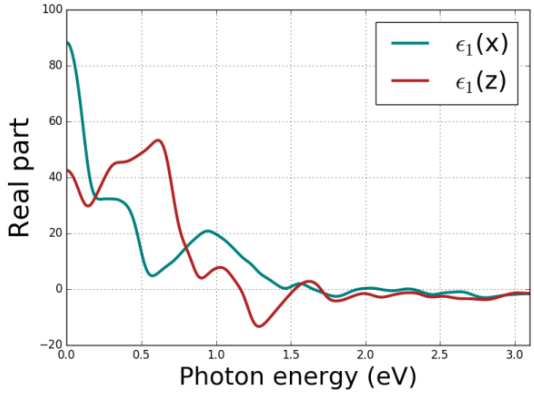

Figure 0.59: $PtTe_2$ real dielectric response function

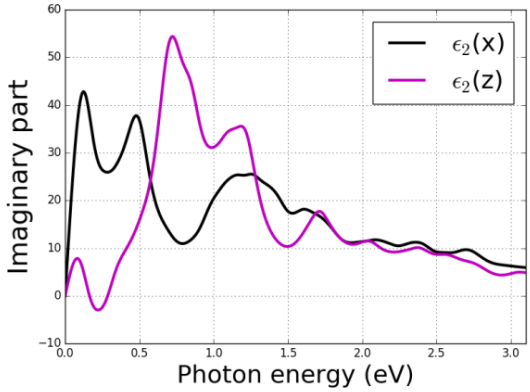

Figure 0.540: $PtTe_2$ imaginary dielectric response function

As in the previous materials the BSE dielectric matrix was calculated using GW input data. In-plane and out-of-plane maximum absorption within the visible range peaks at 1.7 eV and 1.75 eV respectively with out-of-plane absorption slightly superseding the in-plane absorption as shown in Figure 5.54. Maximum in-plane and out-of-plane absorption occurs at 0.5 eV and 1.2 eV respectively. The absorption spectrum depicts optical anisotropy and light directed to $PtTe_2$ will appear red in colour within the visible range.

The general trend shows that reflectivity, refraction index and extinction coefficient in Figures 5.55 to 5.57 have maximum values within the infrared region and decreases across the visible range though there are significant peaks up to the ultraviolet region illustrating the presents of interband transitions.

Figure 5.58 illustrates no energy loss within the visible region with max in-plane and out-of-plane losses occurring within the ultraviolet region at approximately 13 eV and 9.5 eV respectively reflecting the characteristic associated with plasma oscillation at that specific plasma frequency [160]. Real and imaginary dielectric response activity is more noticeable within the infrared region as illustrated in Figures 5.59 and 5.60.

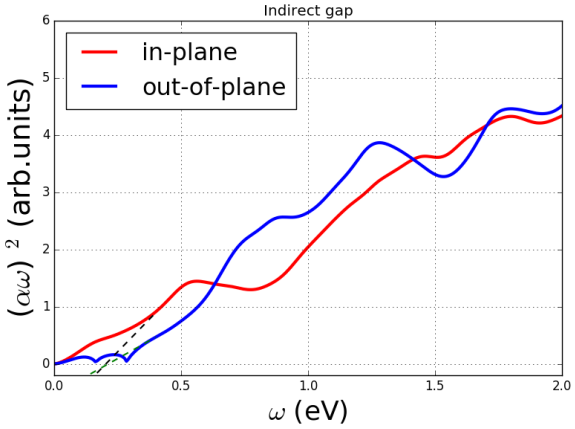

Figure 0.551: $PtTe_2$ optical bandgap

In-plane and out-of-plane absorption band edges were obtained as 0.2033 eV and 0.2127 eV respectively as illustrated in Figure 5.61. In-plane and out-of-plane optical

bandgaps have a marginal shift in the absorption edge of 0.0088 eV. However, the slight difference in the absorption edges as function of incident light polarization depicts optical anisotropy.

5.3.7 Thermal properties of $PtTe_2$

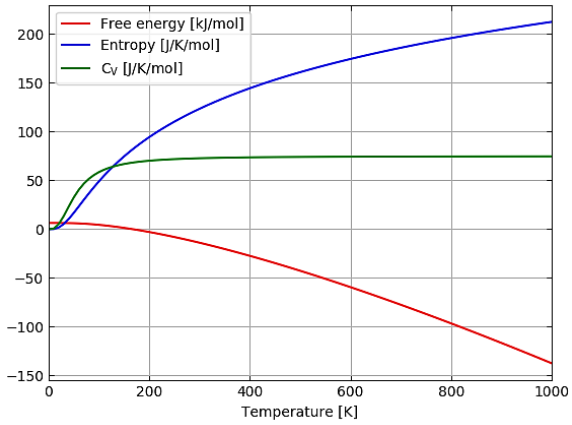

Figure 0.562: $PtTe_2$ calculated temperature dependence of free energy, entropy and C_v.

From Fig 5.62 the specific heat, C_v increases with temperature until it reaches the Dulong-Petit limit at around 74 J(mol K)$^{-1}$. The predicted Helmholtz free energy, specific heat capacity and entropy at 300 K from Figure 5.62 were around -13.93 kJ(mol)$^{-1}$, 72.69 J(mol K)$^{-1}$, and 123.42 J(mol K)$^{-1}$ respectively.

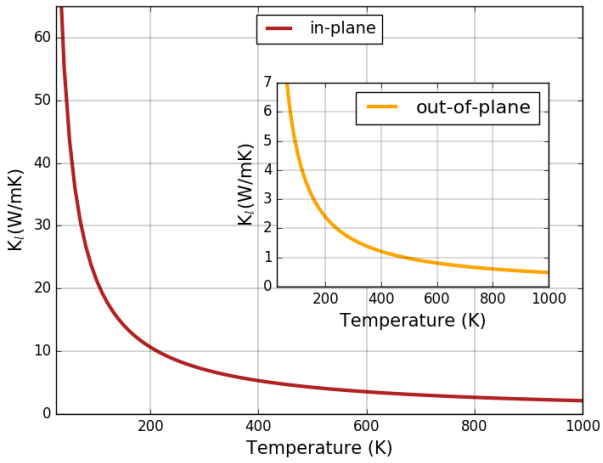

Figure 0.573: $PtTe_2$ lattice thermal conductivity as a function of temperature

Both the in-plane and out-of-plane thermal conductivity also show anisotropy within the material as illustrated in Figure 5.63. The in-plane thermal conductivity is much higher than the out of plane with values of 7.09 W/mK and 1.61 W/mK at 300 K respectively.

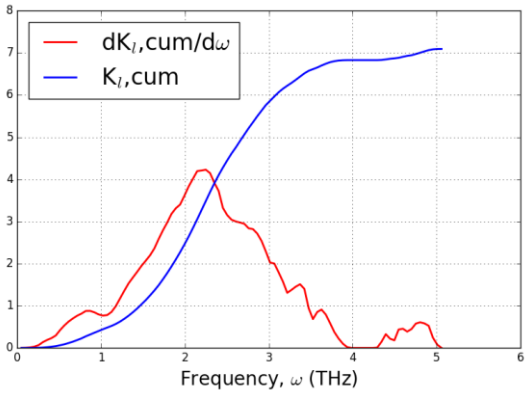

Figure 0.584: $PtTe_2$ in-plane cumulative lattice thermal conductivity and derivative density at 300 K as a function of frequency

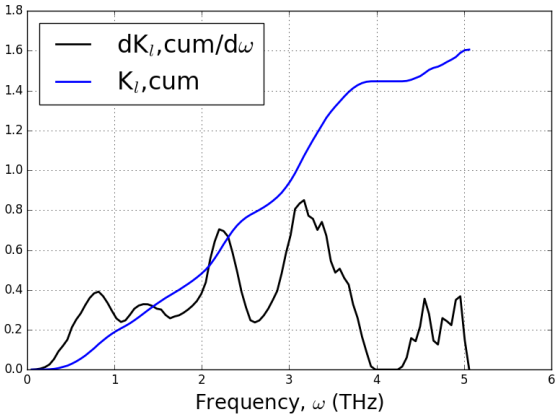

Figure 0.595: $PtTe_2$ out-of-plane cumulative lattice thermal conductivity and derivative density at 300 K as a function of frequency

The in-plane and out-of-plane cumulative thermal conductivities with derivative density of states as functions of frequency at 300 K also show anisotropy as with the

previous two materials. The in-plane cumulative lattice thermal conductivity cum K_l, and its derivative dK_l, also support that the main contributor to K_l is the acoustic phonon modes as shown in Figures 5.64 and 5.65. The out-of-plane cum K_l and its derivative dK_l shows that both acoustic and optical modes contribute towards the K_l.

6 Conclusion and recommendations

6.1 Conclusion

All calculations were done using first principles theory approaches based on DFT. The range of results for different exchange-correlation approximations and vdW corrections highlight a problem in applied DFT. Including vdW interactions in addition to semilocal exchange-correlation approximations is an attempt to address this problem. From the different exchange-correlation functionals used, PBE+TS gave equilibrium volume results that are in good agreement with available experimental results for all systems. In PtS_2, $PtSe_2$ and $PtTe_2$, the PBE+TS functional gave an equilibrium volume deviation of 0,3%, 1,1% and 0,9% respectively.

The compounds were all energetically stable due to the negative cohesive and formation energies implying that they are stable against decomposition into their constituent atoms and constituent solid components. Elastic constants calculations confirmed mechanical stability. The compounds also satisfied their respective Born stability conditions for mechanical stability for trigonal systems. Young's modulus, bulk modulus, shear modulus, and Poisson's ratio were calculated and gave *K/G* ratios of less than 1.75 for PtS_2 and $PtSe_2$, implying that they are anisotropic brittle materials. On the other hand, $PtTe_2$ has been shown to be an anisotropic ductile material.

Phonon dispersion curves gave all positive modes of vibration throughout the Brillouin zones of the systems entailing dynamical stability. PtS_2 had a significant gap of approximately 2 THz between the acoustic and optical branches with Pt being the primary element contributing towards acoustic phonons. $PtSe_2$ had an extremely small

gap and there was an overlap between the acoustic and optical branches in $PtTe_2$. PtS_2, $PtSe_2$ and $PtTe_2$ were found to be semiconducting, semi-metallic and metallic respectively as observed by the occurrence or non-occurrence of energy bands at the Fermi level. The GW (fundamental) and BSE (optical) bandgaps gave more precise results compared to available experimental data.

Excitonic effects play a very significant role in optical properties. Therefore, a suitable description of the electron-electron correlation and electron-hole interaction is extremely required to investigate the electronic and optical properties [102][162]. First-principles GW plus BSE calculations were performed to study the QP band structures and optical spectra of the systems. The calculations were carried out with more focus on the visible range of 1.6 eV-3.1 eV of the electromagnetic spectrum which covers the energy of visible light and incoming photons in the solar radiation. All systems studied were observed to be optically anisotropic within the infrared, visible and ultraviolet ranges of the electromagnetic spectrum.

PtS_2 has an absorption edge at 1.21 eV which is near an optimum value of around 1.4 eV for maximum solar energy conversion required for a single solar cell, therefore can be considered for photovoltaic applications. Since Pt is the dominant contributor to acoustic modes for all compounds, the frequency ranges for the acoustic modes are 0-6 THz, 0-5.4 THz and 0-3.8 THz for PtS_2, $PtSe_2$ and $PtTe_2$ respectively. As the volume increases from S, Se to Te the frequency dispersion of acoustic modes decreases due to the fact that force constants decrease as volume increase. The bulk moduli increase from 47.96 GPa, 61.09 GPa to 65.68 GPa as volume increases from S, Se to Te respectively.

PtS_2, $PtSe_2$ and $PtTe_2$ compounds are highly anisotropic with the in-plane thermal conductivities being much higher than the out-of-plane. At the room temperature, 300 K the in-plane lattice thermal conductivities for PtS_2, $PtSe_2$ and $PtTe_2$ are 41.6 W/mK, 10.39 W/mK and 7.09 W/mK respectively while the out-of-plane are 2.60 W/mK, 1.64 W/mK and 1.61 W/mK respectively. The out-of-plane thermal conductivities confirm that further investigation of PtSe2 and PtTe2 as thermoelectric materials is necessary.

The larger phonon bandgap observed in PtS_2 is favourable to produce larger thermal conductivity compared to the other two compounds due to the reduced acoustical and optical phonon inter-scattering.

Low lattice thermal conductivity is required for efficient thermoelectric devices therefore the lower out-of-plane thermal conductivities for all structures imply that these materials can further be investigated to ascertain their suitability for thermoelectric applications.

6.2 Recommendations

Structural, electronic and optical properties of TMDs have been studied extensively using *ab initio* methods. However, the following recommendations emanating from the current study can be further explored beyond the scope of this study.

How will strain engineering affect the band gap of the monolayer transition metal dichalcogenides?

How will their optical spectra and thermal properties behave when the bulk crystals are thinned down to monolayers as well?

References

[1] J. Li, X. Cheng, A. Shashurin, and M. Keidar, “Review of Electrochemical Capacitors Based on Carbon Nanotubes and Graphene,” *Graphene*, vol. 01, no. 01, pp. 1–13, 2012.

[2] Z. Liu, “Graphene-From basic science to useful technology,” *Natl. Sci. Rev.*, vol. 2, no. 1, p. 16, 2015.

[3] A. K. Geim and K. S. Novoselov "The rise of graphene." *Nat Mater*., vol. 6, no.3, pp. 183-191, 2007.

[4] D. Munz, T. Fett, “Ceramics / Mechanical Properties, Failure Behaviour," *Materials Selection Springer Series in Materials Science*., vol. 171, p. 333, 2012.

[5] S. K. Tripathi and P. B. Barman, “Influence of composition on the optical band gap in A-$Ge_{20}Se_{80-X}In_X$ thin films,” *Chalcogenide Lett.*, vol. 3, no. 12, pp. 121–124, 2006.

[6] M. Hirtz, S. A. Varey, H. Fuchs, and A. Vijayaraghavan, “Attoliter chemistry for nano-scale functionalization of graphene,” *ACS Appl. Mater. Interfaces*, vol. 8, no. 49. pp. 33371-33376, 2016.

[7] R. Heyrovska, “The Coulombic Nature of the van der Waals Bond Connecting Conducting Graphene Layers in Graphite ,” *SciRes*, vol.5, no. 2, pp. 35–38, 2016.

[8] J. N. Fuchs and G. O. Goerbig, “Introduction to the physical properties of graphene,” *Lecture notes*, 2008.

[9] R. Dong and I. Kuljanishvili, “Review Article: Progress in fabrication of transition metal dichalcogenides heterostructure systems,” *J. Vac. Sci. Technol. B, Nanotechnol. Microelectron. Mater. Process. Meas. Phenom.*, vol. 35, no. 3,

p. 030803, 2017.

[10] W. Choi, N. Choudhary, G. H. Han, J. Park, D. Akinwande, and Y. H. Lee, “Recent development of two-dimensional transition metal dichalcogenides and their applications,” *Mater. Today*, vol. 20, no. 3, pp. 116–130, 2017.

[11] G. K. Ahluwalia, "Applications of Chalcogenides: S, Se, and Te," *Springer*, 2016.

[12] D. Jariwala, V. K. Sangwan, L. J. Lauhon, T. J. Marks, and M. C. Hersam, “Emerging device applications for semiconducting two-dimensional transition metal dichalcogenides,” *ACS Nano*, vol. 8, no. 2, pp. 1102–1120, 2014.

[13] B. Radisavljevic, A. Radenovic, J. Brivio, V. Giacometti, and A. Kis, “Single-layer MoS2 transistors,” *Nat. Nanotechnol.*, vol. 6, no. 3, pp. 147–150, 2011.

[14] Z. Huang, W. Zhang, W. Zhang, and Y. Li “Band gap engineering of PtSe2,” *Nano Research*., vol. 7, no. 12, 2016.

[15] C. Trudeau, “Inkjet-Printing of Methylammonium Lead Trihalide Perovskite as Active Layers for Optoelectronic Devices,” *MRS Adv. © 2018 Mater. Res. Soc.*, pp. 2–6, 2018.

[16] G.-B. Liu, D. Xiao, Y. Yao, X. Xu, and W. Yao, “Electronic structures and theoretical modelling of two-dimensional group-VIB transition metal dichalcogenides,” *Chem. Soc. Rev.*, vol. 44, no. 9, pp. 2643–2663, 2015.

[17] D. Voiry and M. Chhowalla, “Phase engineering of transition metal dichalcogenides,” *Chem. Soc. Rev.*, vol. 44, pp. 2702-2712, 2015.

[18] W. Zhao, R. M. Ribeiro, and G. Eda, “Electronic Structure and Optical Signatures of Semiconducting Transition Metal Dichalcogenide Nanosheets,”*Acc.Chem.Res.*, vo.l 48 , no. 1, pp. 1–30, 2014.

[19] H. Zeng and X. Cui, “An optical spectroscopic study on two-dimensional

group-VI transition metal dichalcogenides," *Chem. Soc. Rev.*, vol. 44, no. 9, pp. 2629–2642, 2015.

[20] S. A. Khan and A. Reshak, "First principle study of electronic sturucture, chemical bonding, and optical properties of 5-azido-1H-tetrazole," *Int. J. Electrochem. Sci*, vol. 8, pp 9459-9473, 2013.

[21] E. Torun, H. Sahin, S. Cahangirov, A. Rubio, and F. M. Peeters, "Anisotropic electronic, mechanical, and optical properties of monolayer WTe2," *J. Appl. Phys.*, vol. 119, no. 7, pp. 1–7, 2016.

[22] C. Muratore, V. Varshney, J. J. Gengler, J. J. Hu, J. E. Bultman, "Cross-plane thermal properties of transition metal dichalcogenides," *Appl. Phys. Lett*, vol. 081604, pp. 0–4, 2013.

[23] P. Turmezei, "Chalcogenide Materials for Solar Energy Conversion," *Acta Polytechnica Hungarica*, vol. 1, no. 2, pp. 13–16, 2004.

[24] Arramel, A. Castellanos-Gomez, and B. J. van Wees, "Band Gap Opening of Graphene by Noncovalent π-π Interaction with Porphyrins," *Graphene*, vol. 02, no. 03, pp. 102–108, 2013.

[25] M. Lemme, S. Rodriguez, M. Rudner, and E. Alarcon, "Potential Applications for Graphene Devices in Nanoelectronics." *NanoSpain*, 2012.

[26] F. Schäffel, "The Atomic Structure of Graphene and Its Few-layer Counterparts," in *Graphene*, pp. 5–59, 2013.

[27] M. Molas, L. National, and C. Magn, "Optical properties of atomically thin transition metal dichalcogenides : Observations and puzzles," N*anophotonics*, vol. 6, no. 6, 2016.

[28] M. Bernardi, C. Ataca, M. Palummo, and J. C. Grossman, "Optical and Electronic Properties of Two-Dimensional Layered Materials," *Nanophotonics*, vol. 6, no. 2, pp. 479–493, 2017.

[29] J. A Reyes-Retana, F. Cervantes-Sodi, “Spin-orbital effects in metal-dichalcogenide semiconducting monolayers,” *Scientific Reports*, no. 6:24093 pp. 1–10, 2016.

[30] M. Kirkengen, J. Bergli, and Y. M. Galperin, “Direct generation of charge carriers in c-Si solar cells due to embedded nanoparticles,” *J. Appl. Phys.*, vol. 102, no. 9, pp. 1–12, 2007.

[31] M. H. Saleh, M. M. A.-G. Jafar, B. N. Bulos, and T. M. F. Al-Daraghmeh, “Determination of Optical Properties of Undoped Amorphous Selenium (a-Se) Films by Dielectric Modeling of Their Normal-Incidence Transmittance Spectra,” *Appl. Phys. Res.*, vol. 6, no. 6, pp. 10–44, 2014.

[32] A. Pospischil and T. Mueller, “Optoelectronic Devices Based on Atomically Thin Transition Metal Dichalcogenides,” *Appl. Sci.*, vol. 6, no. 3, p. 78, 2016.

[33] X. Gu and R. Yanga, “Phonon transport in single-layer transition metal dichalcogenides : A first-principles study,” *Appl. Phys.* Lett, vol. 105, no. 13, 2014.

[34] S. D. Guo, “Biaxial strain tuned thermoelectric properties in monolayer $PtSe_2$,” *J. Mater. Chem. C*, vol. 4, no. 39, pp. 9366–9374, 2016.

[35] Z. Zhang, Y. Xie, Y. Ouyang, and Y. Chen, “A systematic investigation of thermal conductivities of transition metal dichalcogenides,” *International Journal of Heat and Mass Transfer*, vol. 108, pp. 1–17, 2016.

[36] N. Peimyoo, J. Shang, W. Yang, Y. Wang, C. Cong, and T. Yu, “Thermal conductivity determination of suspended mono- and bilayer WS_2 by Raman spectroscopy,” *Nano Res.*, vol. 8, no. 4, pp. 1210–1221, 2015.

[37] M. Yan, H. Huang, K. Zhang, E. Wang, W. Yao, K. Deng, G. Wan, H. Zhang, M. Arita, H. Yang, Z. Sun, H. Yao, Y. Wu, S. Fan, W. Duan and S. Zhou, “Lorentz-violating type-II Dirac fermions in transition metal dichalcogenide

$PtTe_2$," *Nature Communications*, pp. 1–12, 2016.

[38] M. Saito *et al.*, "The Structure of Amorphous Platinum Disulfide as Studied by Anomalous X-ray Scattering," *Zeitschrift für Naturforsch. A*, vol. 49, no. 11, 1994.

[39] Y. Zhao *et al.*, "Extraordinarily Strong Interlayer Interaction in 2D Layered PtS2," *Adv. Mater.*, vol. 28, no. 12, pp. 2399–2407, 2016.

[40] L. Oakes, R. Carter, T. Hanken, A. P. Cohn, K. Share, B. Schmidt and C. L. Pinta, "Interface strain in vertically stacked two-dimensional heterostructured carbon-MoS_2 nanosheets controls electrochemical reactivity," *Nature Communications*, vol. 7, no. 11796, 2016.

[41] X. C. Pan *et al.*, "Pressure-driven dome-shaped superconductivity and electronic structural evolution in tungsten ditelluride," *Nat. Commun.*, vol. 6, pp. 3–8, 2015.

[42] C. Yim, V. Passi, M. C. Lemme, G. S. Duesberg, C. Ó. Coileáin, E. Pallechi, D. Fadil, and N. McEvoy, "Electrical characterization of structured platinum diselenide devices," *cond-mat.mtrl-sci*, arXiv:1707.06824, 2017.

[43] N. Zibouche, A. Kuc, P. Miró, and T. Heine, "Noble-Metal Chalcogenide Nanotubes," *Inorganics*, vol. 2, no. 4, pp. 556–564, 2014.

[44] Q. H. Wang, K. Kalantar-Zadeh, A. Kis, J. N. Coleman, and M. S. Strano, "Electronics and optoelectronics of two-dimensional transition metal dichalcogenides," *Nat Nano*, vol. 7, no. 11, pp. 699–712, Nov. 2012.

[45] F. Zeng, W-B. Zhang, B-Y. Tang, "The electronic structure and elastic property of monolayer and bilayer transition metal dichalcogenides MX_2," *Chin. Phys.* B, vol. 24, no. 9, 2015.

[46] Y. Li, K. N. Duerloo, K. Wauson, and E. J. Reed, "electrostatic gating," *Nat. Commun.*, pp. 1–8, 2016.

[47] M. T. Dove, “An introduction to atomistic simulation methods,” *Semin. la SEM*, vol. 4, pp. 7–37, 2008.

[48] Y. Inoue, M. Kitano, S. Matsuishi, M. Hara, and H. Hosono, Y. Yamazaki, F. Hayashi, S. Kanbara, T. Yokoyama, S. W Kim, “Ammonia synthesis using a stable electride as an electron donor and reversible hydrogen store," *Nat Chem.*, vol. 4, no. 11, 2012.

[49] G. Bao, G. Hu, and D. Liu, “Numerical solution of the kohn-sham equation by finite element methods with an adaptive mesh redistribution technique,” *J. Sci. Comput.*, vol. 55, no. 2, pp. 372–391, 2013.

[50] N. M. Harrison, “An Introduction to Density Functional Theory,” *Technology*, vol. 2, no. 1, pp. 1–26, 1995.

[51] D. Zhou, “An Introduction of Density Functional Theory and its Application,” *Physics.Drexel.Edu*, 2007.

[52] Y. Iwata *et al.*, “The Thomas-Fermi-von Weizscker theory of atoms and molecules,” *J. Nucl. Sci. Technol.*, vol. 41, no. 3, pp. 1–20, 2004.

[53] T. H. E. H. Theorem, “Lecture VII : The Hohenberg-Kohn theorem and the Kohn-Sham equations,” *Pnas*, vol. 1964, no. 1, pp. 1–8, 1964.

[54] T. Hohenberg, “Hohenberg – Kohn theorem Proof of the Hohenberg – Kohn theorem,” vol. 864, 1964.

[55] T. Hohenberg-kohn, “CHEM6085 : Density Functional Theory Lecture 4 Density instead of the wavefunction Functions and functionals.”

[56] Martin, “Richard M. Martin-Electronic Structure. Basic Theory and Practical Methods," Cambridge University Press, vol. 1, 2008.

[57] T. Vehoff, “Density functional theory (DFT),” *J. Club Cover. those Methods Which are Now Used as a “Black Box,”* p. 8, 2008.

[58] R. van Leeuwen, O. Gritsenko, E. J. Baerends “Step structure in the atomic Kohn-Sham potential,” *Zeitschrift für Physik D Atoms, Molecules and Clusters*, vol. 33, no. 4, pp 229–238, 1995.

[59] V. N. Staroverov, “Density-Functional Approximations for Exchange and Correlation,” *A Matter Density Explor. Electron Density Concept Chem. Biol. Mater. Sci.*, pp. 125–156, 2012.

[60] S. Clark, “Local Density Approximation,” 2003.

[61] C. Skylaris, “CHEM6085 : Density Functional Theory Lecture 9 Exchange-correlation functionals Kohn-Sham energy expression,” *Univ. Southampt.*

[62] C. D. Sherrill, “Introduction to Density Functional Theory.”

[63] J. P. Perdew, M. Ernzerhof, and K. Burke, “Rationale for mixing exact exchange with density functional approximations,” *J. Chem. Phys.*, vol. 105, no. 22, pp. 9982–9985, 1996.

[64] B. Santra, “Density-Functional Theory Exchange-Correlation Functionals for Hydrogen Bonds in Water,” *Von der Fak. II Math. und Naturwissenschaften der Tech. Univ. Berlin zur Erlangung des Akad. Grades Dr. RERUM Nat.*, p. 152, 2010.

[65] J. P. Perdew and A. Zunger, “Self-interaction correction to density-functional approximations for many-electron systems,” *Phys. Rev. B*, vol. 23, no. 10, pp. 5048–5079, 1981.

[66] R. Jones, “Introduction to Density Functional Theory and Exchange-Correlation Energy Functionals,” *Comput. Nanosci.*, vol. 31, pp. 45–70, 2006.

[67] I. Tavernelli, B. F. E. Curchod, and U. Rothlisberger, “Nonadiabatic ab initio molecular dynamics using linear-response time-dependent density functional theory,” *Central European Journal of Physics*, vol. 11, no. 9, pp. 059–1065, 2013.

[68] J. Hermann, R. A. DiStasio Jr, and A. Tkatchenko, “First-Principles Models for van der Waals Interactions in Molecules and Materials: Concepts, Theory, and Applications,” *Chem. Rev*., vol. 117, no. 6, pp 4714–4758, 2017.

[69] P. L. Silvestrelli, A. Ambrosetti, "Van Der Waals-Corrected Density Functional Theory Simulation of Adsorption Processes on Noble-Metal Surfaces: Xe on Ag(111), Au(111), and Cu(111)," *Journal of Low Temperature Physics*, vol. 185, pp. 1-2, 2016.

[70] N. Marom *et al.*, “Dispersion interactions with density-functional theory: Benchmarking semiempirical and interatomic pairwise corrected density functionals,” *J. Chem. Theory Comput.*, vol. 7, no. 12, pp. 3944–3951, 2011.

[71] T. Bučko, S. Lebègue, J. Hafner, and J. G. Ángyán, “Tkatchenko-Scheffler van der Waals correction method with and without self-consistent screening applied to solids,” *Phys. Rev. B*, no 87, vol. 064110, 2013.

[72] J. Park, B. D. Yu, and S. Hong, “Van der Waals density-functional theory study for bulk solids with BCC, FCC, and diamond structures,” *Current Applied Physics*, vil. 15, no. 8, 2015.

[73] S. Ling, “van der Waals corrected DFT,” *4th CP2K Tutorial*, 2015.

[74] J. Klimeš, D. R. Bowler, and A. Michaelides, “Van der Waals density functionals applied to solids,” *Physical Review B*, vol. 83 , no. 19, 2011.

[75] J. Klimeš, D. R. Bowler and A. Michaelides, “Chemical accuracy for the van der Waals density functional,” *Condensed Matter*, vol. 22, no. 2, 2009.

[76] J. B. A. Davis, F. Baletto, and R. L. Johnston, “The Eff ect of Dispersion Correction on the Adsorption of CO on Metallic Nanoparticles,” *J. Phys. Chem. A*, vol. 119, no. 37, pp. 9703-9709, 2015.

[77] A. V Terentjev, L. A. Constantin, and J. M. Pitarke, “Dispersion-corrected PBEsol exchange-correlation functional,” *Physical review B* 98, vol. 214108,

pp. 1–12, 2018.

[78] J. E. Moussa, P. A. Schultz, and J. R. Chelikowsky, “Analysis of the Heyd-Scuseria-Ernzerhof density functional parameter space,” *J. Chem. Phys.* vol. 136, no. 20, 2012.

[79] J. Heyd and G. E. Scuseria, “Efficient hybrid density functional calculations in solids : Assessment of the Heyd – Scuseria – Ernzerhof screened Coulomb hybrid functional,” *J. Chem. Phys.* vol. 121, no. 3, 2004.

[80] D. P. Rai, M. P. Ghimire, and R. K. Thapa, “A DFT study of BeX (X = S , Se , Te) semiconductor : modified Becke Johnson (mBJ) potential,” *Physics and technology of semiconductors*, vol. 2, pp. 1447–1457, 2014.

[81] K. Choudhary, Q. Zhang, A. C. E. Reid, S. Chowdhury, and N. Van Nguyen, “Computational screening of high-performance optoelectronic materials using OptB88vdW and TB-mBJ formalisms,” *Scientific Data,* vol. 5, no. 180082 2018.

[82] D. J. Singh, “Electronic Structure Calculations with the Tran-Blaha Modified Becke-Johnson Density Functional,” *Phys. Rev. B*, vol. 82, no. 205102, 2010.

[83] K. Parlinski, “Phonons calculated from first-principles,” *Tous les numéros*, vol. 12, pp. 161–166, 2011.

[84] A. Togo and I. Tanaka, “First principles phonon calculations in materials science,” *Scr. Mater.*, vol. 108, pp. 1–5, 2015.

[85] R. M. Dreizler and E. K. U. Gross, “Many-Body Perturbation Theory,” in *Density Functional Theory: An Approach to the Quantum Many-Body Problem*, Berlin, Heidelberg: Springer Berlin Heidelberg, 1990, pp. 138–172.

[86] F. Bruneval, F. Sottile, V. Olevano, D. Sole, and R. Tor, “Many-body perturbation theory using the density-functional concept,” *Phys. Rev.B*, vol 46, no. 13051, 1992.

[87] S. Scherer, “Introduction to Chiral Perturbation Theory,” *Advances in Nuclear Physics*, vol. 27 pp 277-538 no. January, 2003.

[88] G. Onida, L. Reining, A. Rubio, “Electronic excitations : density-functional versus many-body Green’s-function approaches,” *Rev.Mod.Phys.*, vol. 74, pp. 601-659, 2002.

[89] L. Hedin, B. I. Lundqvist, and S. Lundqvist, “Local exchange-correlation potentials,” *Solid State Commun.*, vol. 9, no. 9, pp. 537–541, 1971.

[90] K. A. Milton, “Julian Schwinger (1918-1994),” pp. 1–21, 2006.

[91] P. Lamarque, “Universities of Leeds , Sheffield and York,” *Online*, vol. 135, 2008.

[92] F. Aryasetiawan and O. Gunnarsson, “The GW method,” *Rep. Prog. Phys.*, vol. 61, no, 237, 1998.

[93] Q. De Wang, H. Y. Wu, K. X. Fu, and X. Y. Li, “Continuum model for electronic polarization based on a novel dielectric response function,” *Chinese J. Chem. Phys.*, vol. 22, no. 5, pp. 481–488, 2009.

[94] Y. Feldman, A. Puzenko, and Y. Ryabov, “Dielectric Relaxation Phenomena in Complex Materials,” *Adv. Chem. Physics, Fractals, Diffus. Relax. Disord. Complex Syst.*, vol. 133, pp. 1–125, 2005.

[95] L. G. Molinari, “A derivation of hedin’s equations,” pp. 1–9, 2017.

[96] M. Jarrell, “Lecture 1 : The Equilibrium Green Function Method,” pp. 1–17, 2011.

[97] R. Godby, “GW Many-Body Theory for Electronic Structure,” *University of York lecture*, 2008.

[98] F. Bruneval, F. Sottile, V. Olevano, R. Del Sole, and L. Reining, “Many-body perturbation theory using the density-functional concept,” *Psi-K, Newslett.*,

vol. 69, pp. 79–92, 2005.

[99] F. Bruneval, F. Sottile, V. Olevano, R. D. Sole, L. Reining, "Many-body perturbation theory using the density-functional concept: beyond the GW approximation," *Phys. Rev. Lett.*, vol. 94, no. 186402, 2005.

[100] F. Aryasetiawan and O. Gunnarsson, "The GW method," *Reports Prog. Phys.*, vol. 61, no. 3, pp. 237–312, 1998.

[101] S. Botti, "Introduction to GW and Bethe-Salpeter," *European Theoretical Spectroscopy Facility*, 2010.

[102] J. Sun, R. Zhang, X. Li, and J. Yang, "A many-body GW+BSE investigation of electronic and optical properties of C_2N," *Appl. Phys. Lett.*, vol. 109 no. 133108, pp. 1–13, 2016.

[103] S. Botti, "Electronic excitations in complex systems: beyond density functional theory for real materials," *Condensed Matter*, p. 154, 2010.

[104] S. Masuda, S. Hosokawa, I. Tochizawa, K. Akutsu, K. Kuwano, and A. Iwata, "Surface Treatment of Plastic Material by Pulse Corona Induced Plasma Chemical Process-PPCP," *IEEE Trans. Ind. Appl.*, vol. 30, no. 2, pp. 377–380, 1994.

[105] A.R. Goñi, K.Syassen, "Semiconductors and Semimetals," *ScienceDirect*, vol. 54, pp. 247-425, 1998.

[106] V. Bhavsar and D. Tripathi, "Study of refractive index dispersion and optical conductivity of PPy doped PVC films," *Indian J. Pure Appl. Phys.*, vol. 54, no. 2, pp. 105–110, 2016.

[107] S. K. Tripathy and A. Pattanaik, "Optical and electronic properties of some semiconductors from energy gaps," *Opt. Mater. (Amst).*, vol. 53, pp. 123–133, 2016.

[108] J. Q. Lei, K. Liu, S. Huang, and X. L. Zhou, “The comparative study on bulk-PtSe2 and 2D 1-Layer-PtSe2 under high pressure via first-principle calculations,” *Theor. Chem. Acc.*, vol. 136, no. 9, pp. 1–10, 2017.

[109] P. Sałek, “Density-functional theory of linear response and nonlinear time-dependent molecular properties," *J.Chem.Phy.* vol. 117, no. 9630, 2002.

[110] T. Numai, “Optical Transitions,” *Fundam. Semicond. lasers*, vol. 93, pp. 89–186, 2015.

[111] W. S. Choi, S. S. A. Seo, K. W. Kim, and T. W. Noh, “Dielectric constants of Ir , Ru , Pt , and IrO_2 : Contributions from bound charges,” *Phys. Rev. B*, vol. 74, no. 205117, 2006.

[112] S. A. R. Horsley, M. Artoni, and G. C. La Rocca, “Spatial Kramers – Kronig relations and the reflection of waves,” *Nat. Photonics*, vol. 9, no. 7, pp. 436-439, 2015.

[113] Y. Jiang, S. Pillai, and M. A. Green, “Re-evaluation of literature values of silver optical constants,” *Optics Express*, no. 3, pp. 2133-2144, 2015.

[114] M. Kumar, S. Ishii, N. Umezawa, and T. Nagao, “Band engineering of ternary metal nitride system Ti1-x ZrxN for plasmonic applications,” *Opt. Mater. Express*, vol. 6, no. 1, p. 29, 2016.

[115] A. C. Sparavigna “The Boltzmann Equation Of Phonon Thermal Transport Solved In the Relaxation Time Approximation – I –Theory,” *Engineering Journal*, vol. 3, pp.34-45, 2016.

[116] G. Kresse and M. Marsman, “Vienna Ab-initio Simulation Package VASP the GUIDE,” *VASP Man.*, 2014.

[117] D. Joubert, “From ultrasoft pseudopotentials to the projector augmented-wave method,” *Phys. Rev. B - Condens. Matter Mater. Phys.*, no. 59, p. 1758, 1999.

[118] P. E. B. öchl, C. J. F. örst, and J. Schimpl, “Projector augmented wave method: ab initio molecular dynamics with full wave functions,” *Bull. Mater. Sci.*, vol. 26, no. 1, pp. 33–41, 2003.

[119] P.E. Bl¨ochl, “Projector augmented-wave method,” *Bull.Mater.Sci.*, vol. 26, no. 1, 2003.

[120] K. A. P. A. Jain, S.P. Ong, G. Hautier, W. Chen, W.D. Richards, S. Dacek, S. Cholia, D. Gunter, D. Skinner, G. Ceder, “The Materials Project: A materials genome approach to accelerating materials innovation," *APL Materials*,” vol. 1, no. 011002, 2013.

[121] R. Peverati and D. G. Truhlar, “Exchange-correlation functional with good accuracy for both structural and energetic properties while depending only on the density and its gradient,” *J. Chem. Theory Comput.*, vol. 8, no. 7, pp. 2310–2319, 2012.

[122] G. C. S.P. Ong, W.D. Richards, A. Jain, G. Hautier, M. Kocher, S. Cholia, D. Gunter, V. Chevrier, K. A. Persson, “Python Materials Genomics (pymatgen) : A Robust, Open-Source Python Library for Materials Analysis," *Computational Materials Science*, vol. 68, pp. 314–319, 2013.

[123] L. Zhou, D. Holec, and P. Mayrhofer, “First-principles study of elastic properties of Cr-Al-N,” *arXiv Prepr. arXiv1209.0955*, pp. 1–24, 2012.

[124] A. Togo and I. Tanaka, “First principles phonon calculations in materials science,” *Scr. Mater.*, vol. 108, pp. 1–5, 2015.

[125] J. Yang, D. T. Morelli, G. P. Meisner, W. Chen, J. S. Dyck, and C. Uher, “Influence of electron-phonon interaction on the lattice thermal conductivity of $Co_{1-x}Ni_xSb_3$"**,”** *Phys. Rev. B.*, vol. 65, no. 094115 vol. 25, 2002.

[126] J. Garai, “Universal Equation of States are Derived from the Isothermal Relationships of Elastic Solids,” *arXiv:physics.geo-ph*, vol. 3, no. 2, pp. 1–9,

2008.

[127] R. Gaillac, P. Pullumbi, and F. X. Coudert, “ELATE: An open-source online application for analysis and visualization of elastic tensors,” *J. Phys. Condens. Matter*, vol. 28, no. 27, p. 275201, 2016.

[128] B. B. Karki, G. J. Ackland and J. Crain, “Elastic instabilities in crystals from ab initio stress-strain relations,” *J. Phys.: Condens. Matter*, vol. 9, pp. 8579-8589, 1997.

[129] P. Thibault, “A Review of Equation of State Models , Chemical Equilibrium Calculations and CERV Code Requirements for SHS Detonation Modelling,” *Defence R&D Canada Contract Report*, no. 54, 2009.

[130] S. M. Naidu, “Engineering Physics,” vol. 1, 2009.

[131] B. J. Abdullah, M. S. Omar, N. S. Saadi, and Q. Jiang, “First-Principles Calculations on Cohesive Energy of Bulk and Nano Si,” *International Journal of Scientific & Engineering Research*, vol. 6, no. 9, pp. 842–846, 2015.

[132] P. Jund, R. Viennois, C. Colinet, G. Hug, and M. Fèvre, “Lattice stability and formation energies of intrinsic defects in Mg 2 Si and Mg 2 Ge via first principles simulations,” *J. Phys. Condens. Matter*, vol. 25, no. 25, pp. 1–25, 2013.

[133] A. H. Reshak and M. Jamal, “DFT calculation for elastic constants of tetragonal structure of crystalline solids with WIEN2K code: A new package (tetra-elastic),” *Int. J. Electrochem. Sci.*, vol. 8, no. 11, pp. 12252–12263, 2013.

[134] F. Mouhat and F. X. Coudert, “Necessary and sufficient elastic stability conditions in various crystal systems,” *Phys. Rev. B - Condens. Matter Mater. Phys.*, vol. 90, no. 22, pp. 0–3, 2014.

[135] R. Sot and K.J. Kurzydłowski, “Ab initio calculations of elastic properties of

Ni_3Al and TiAl under pressure," *Materials science-Poland*, vol. 23, no. 3, pp. 10–13, 2005.

[136] S. Savrasov, "Linear-response theory and lattice dynamics: A muffin-tin-orbital approach," *Phys. Rev. B - Condens. Matter Mater. Phys.*, vol. 54, no. 23, pp. 16470–16486, 1996.

[137] R. Heid, "Density Functional Perturbation Theory and Electron Phonon Coupling," *Emergent Phenom. Correl. Matter Model. Simul.*, vol. 3, pp. 1–27, 2013.

[138] D. Alfè, "PHON: A program to calculate phonons using the small displacement method," *Comput. Phys. Commun.*, vol. 180, no. 12, pp. 2622–2633, 2009.

[139] R. Jacob and J. Isac, "Band gap energy profile of BSFT (BaSr.9Fe.1TiO4)," *International Journal of Scientific and Research Publications*, vol. 4, no. 12, pp. 1–6, 2014.

[140] J. Tauc, "Optical properties and electronic structure of amorphous Ge and Si," *Mater. Res. Bull. 3*, pp. 37–46, 1968.

[141] J. J. Plata, D. Usanmaz, P. Nath, C. Toher, J. Carrete, M. Asta, M. de Jong, M. B. Nardelli, M. Fornari, S. Curtarolo., "Predicting the lattice thermal conductivity of solids by solving the Boltzmann transport equation: AFLOW - AAPL an automated, accurate and effcient framework," *cond-mat.mtrl-sci*, pp. 1–11, 2016.

[142] Y. Zhao and D. G. Truhlar, "Construction of a generalized gradient approximation by restoring the density-gradient expansion and enforcing a tight Lieb-Oxford bound," *J. Chem. Phys.*, vol. 128, no. 18, pp. 1–8, 2008.

[143] I. V. Lebedeva, A. V. Lebedev, A. M. Popov, and A. A. Knizhnik, "Comparison of performance of van der Waals-corrected exchange-correlation

functionals for interlayer interaction in graphene and hexagonal boron nitride," *Computational Materials Science*, vol. 128, pp. 45-58, 2017.

[144] B. S. Dey and V. K. Jain, "Platinum Group Metal Chalcogenides," *Platin. Met. Rev*, vol. 48, no. 1, pp. 16–29, 2004.

[145] G. Y. Guo and W. Y. Liang, "The electronic structures of platinum dichalcogenides: PtS_2, $PtSe_2$ and $PtTe_2$," *J. Phys. C Solid State Phys.*, vol. 19, no. 7, pp. 995–1008, 1986.

[146] Arne Kjekshus and Fredrick Gronvold, "High Temperature X-Ray Study of the Thermal Expansion of PtS2, PtSe2, PtTe2, PdTe2," *Acta Chem. Scand.*, vol. 13, pp. 1767–1774, 1959.

[147] H.Tributsch, O.Gorochov, "Photoelectrochemical reaction behaviour of platinum disulphide with water and reducing agents," *Electrochimica Acta*, vol. 27, no. 2, pp. 215-221, 1982.

[148] A. K. S. Furuseth, K. Selte, "Redertimined Crystal Structures of $PdTe_2$, $PtSe_2$, PtS_2 and $PtTe_2$," *Acta Chem. Scand.*, vol. 19, p. 257, 1965.

[149] S. Wu1, S. S. Naghavi1, G. H. Fecher1, C. Felser, "A Critical Study of the Elastic Properties and Stability of Heusler Compounds: Phase Change and Tetragonal X_2YZ Compounds," *Journal of Modern Physics*, vol. 9, pp. 775-805, 2018.

[150] G. Wang *et al.*, "Ab initio prediction of the mechanical properties of alloys: The case of Ni/Mn-doped ferromagnetic Fe," *Phys. Rev. B - Condens. Matter Mater. Phys.*, vol. 91, no. 22, pp. 1–14, 2015.

[151] H. Einollahzadeh, R. S. Dariani, and S. M. Fazeli, "Computing the band structure and energy gap of penta-graphene by using DFT and G_0W_0 approximations," *Solid State Commun.*, vol. 229, pp. 1–10, 2016.

[152] F. Parsapour, D. F. Kelley, and R. S. Williams, "Spectroscopy of Eu 3+ -

Doped PtS_2 Nanoclusters," *Physical Chemistry B*, vol. 102, no. 41, pp. 7971-7977, 1998.

[153] Z. Huang, W. Zhang, and W. Zhang, "Computational Search for Two-Dimensional MX2 Semiconductors with Possible High Electron Mobility at Room Temperature," *Materials (Basel).*, vol. 9, no. 9, p. 716, 2016.

[154] G. Y. Guo, W. Y. Liang "The electronic structures of platinum dichalcogenides: PtS2, PtSe2 and PtTe2," *J Phys C Solid State Phys*, vol. 19, no. 7, 2000.

[155] J. P. Perdew, W. Yang, K. Burke, Z. Yang, E. K. U. Gross, M. Scheffler, G. E. Scuseria, T. M. Henderson, I. Y. Zhang, A. Ruzsinszky, H. Peng, J. Sun, E. Trushin, and A. Görling, "Understanding Band Gaps of Solids in Generalized Kohn-Sham Theory," *PNAS*, vol. 114, no. 11, pp. 1–23, 2017.

[156] F. Ricci *et al.*, "Theoretical and experimental investigation of optical absorption anisotropy in β-Ga2O3.," *J. Phys. Condens. Matter*, vol. 28, no. 22, p. 224005, 2016.

[157] X. Blase, P. Boulanger, F. Bruneval, M. Fernandez-serra, and I. Duchemin, "GW and Bethe-Salpeter study of small water clusters," *The Journal of Chemical Physics*, vol. 144, no. 3, 2016.

[158] F. Seitz, D.Turnbull, "Solid State Physics," vol. 18, 1966.

[159] E. F. Westrum, Jr., and H. G. Carlson, "Low-Temperature Heat Capacities and Thermodynamic Functions of Some Palladium and Platinum Group Chalcogenides. II. Dichalcogenides; PtS_2, $PtTe_2$, and $PdTe_2$," *Chemical Physics*, vol. 35, no. 5, pp. 1670–1676, 1961.

[160] B. Mohamed, M. Allel, D. Bendouma, B. Miloud, M. Baghdad, and P. Technology, "Improved Electronic Structure and Optical Performance of Bi2 $Te_{3-x}Se_x$ From First-principle Calculations Within TB-mBJ Exchange

Potential," *Materials Research*, vol. 21, no. 1, pp. 1–9, 2018.

[161] Y. Matsuda, J. Tahir-kheli, and W. A. Goddard, "Definitive Band Gaps for Single-Wall Carbon Nanotubes," *J. Phys. Chem. Lett.*, vol. 1, no. 19, pp. 2946–2950, 2010.

[162] J. Yan, K. W. Jacobsen, and K. S. Thygesen, "Optical properties of bulk semiconductors and graphene/boron nitride: The Bethe-Salpeter equation with derivative discontinuity-corrected density functional energies," *Phys. Rev. B - Condens. Matter Mater. Phys.*, vol. 86, no. 4, 2012.

[163] P. R. Cantwell *et al.*, "Estimating the In-Plane Young ' s Modulus of Polycrystalline Films in MEMS," J*ournal of Microelectromechanical Systems*, vol. 21, no. 4, 2012.

[164] D. N. Blaschke, "Averaging of elastic constants for polycrystals," *Journal of Applied Physics*, vol. 22, no. 14, 2017.

Appendix A

Materials Project

Computational materials science is now powerful enough to predict numerous properties of materials before they are synthesized in the lab. All input files (INCAR, KPOINTS, POSCAR) for this study were obtained from Materials Project which provides open web-based access to computed information on known and predicted materials as well as analysis tools for designing new materials and to accelerate innovation in materials research. The POTCAR files were generated through Python Materials Genomics (pymatgen) which is a robust materials analysis code that defines core object representations for structures and molecules with support for many electronic structure codes.

Elastic constants

The general relationship between stress and strain is given by the generalized version of the Hooke's law.

$$\sigma_{ij} = C_{ijkl}\varepsilon_{kl}$$

Where *C* is a fourth order stiffness tensor σ, stress tensor ε, the strain and *i , j ,k ,l = x, y, z* . Expressing the strains in terms of the stresses gives,

$$\varepsilon_{ij} = S_{ijkl}\sigma_{kl}$$

where S_{ijkl} is a fourth order compliance tensor.

The elastic constants and moduli are fundamental parameters that provide information about the mechanical properties of materials. For anisotropic materials due to symmetry of the Cauchy stress tensor $\sigma_{ij} = \sigma_{ji}$ and the generalized Hooke's law it

implies that $C_{ijkl} = C_{jikl}$. These conditions reduce the number of elastic constants from 81 to 21 and they can be further reduced to 21 due to symmetry arguments.

$$C_{ij} = \begin{pmatrix} C_{11} & C_{12} & C_{13} & C_{14} & C_{15} & C_{16} \\ & C_{22} & C_{23} & C_{24} & C_{25} & C_{26} \\ & & C_{33} & C_{34} & C_{35} & C_{36} \\ & Symmetric & & C_{44} & C_{45} & C_{46} \\ & & & & C_{55} & C_{56} \\ & & & & & C_{66} \end{pmatrix}$$

The total number of independent elastic constants is illustrated in the table below.

Elastic conditions in various crystal systems

The following table illustrates different crystal systems including Laue groups and number of independent second-order elastic constants C_{ij} [134].

Crystal system	**Laue class**	**Point groups**	**C_{ij}'s**
Cubic(I) Cubic(II)	$m\bar{3}m$ $m\bar{3}$	432, $\bar{4}3m$, $m\bar{3}m$ 23, $m\bar{3}$	3
Hexagonal(I) Hexagonal(II)	6/*mmm* 6/*m*	6*mm*, 622, $\bar{6}2m$, 6/*mmm* 6, $\bar{6}$, 6/*m*	5
Rhombohedral(I)	$\bar{3}m$	32, 3*m*, , $\bar{3}m$	6
Rhombohedral(II)	$\bar{3}$	3, $\bar{3}$	7
Tetragonal(I)	4/*mmm*	4*mm*, 422,$\bar{4}2m$, 4/*mmm*	6
Tetragonal(II)	4/*m*	4, $\bar{4}$, 4/*m*	7
Orthorhombic	*Mmm*	222, 2*mm*, *mmm*	9
Monoclinic	2/*m*	2, *m*, 2/*m*	13

The corresponding Born elastic stability conditions are:

Crystal system	
Cubic	$C_{11}- C_{12} > 0$; $C_{11}+2 C_{12} > 0$; $C_{44} > 0$
Hexagonal Tetragonal(I)	$C_{11} > \|C_{12}\|$; $2C_{13}^2 < C_{33}(C_{11} + C_{12})$; $C_{44} > 0$; $C_{66} > 0$ and $C_{66} = (C_{11} - C_{12})/2$
Rhombohedral(I)	$C_{11} > \|C_{12}\|$; $C_{44} > 0$; $C_{13}^2 < \frac{1}{2} C_{33}(C_{11} + C_{12})$; $C_{14}^2 < \frac{1}{2} C_{44} (C_{11} - C_{12}) = C_{44}C_{66}$
Rhombohedral(II)	$C_{11} > \|C_{12}\|$; $C_{44} > 0$; $C_{13}^2 < \frac{1}{2} C_{33}(C_{11} + C_{12})$; $C_{14}^2 + C_{15}^2 < \frac{1}{2} C_{44} (C_{11} - C_{12}) = C_{44}C_{66}$
Tetragonal(II)	$C_{11} > \|C_{12}\|$; $C_{13}^2 < C_{33}(C_{11} + C_{12})$; $C_{44} > 0$; $2C_{16}^2 < C_{66} (C_{11} - C_{12})$
Orthorhombic	$C_{11} > 0$; $C_{11}C_{22} > C_{12}^2$; $C_{11}C_{22}C_{33} + C_{12}C_{13}C_{23} – C_{11}C_{23}^2 - C_{22}C_{13}^2 - C_{33}C_{12}^2 > 0$; $C_{44} > 0$; $C_{55} > 0$; $C_{66} > 0$

Voight, Reuss and Hill averaging schemes

Many materials of interest are polycrystals, with distributed orientations of single crystals leading to macroscopically isotropic properties. We may therefore derive effective isotropic elastic constants for polycrystals by averaging over the elastic constants of the single crystal grains since the Voight and Reuss methods at third order, unfortunately do not yield bounds on the true average in a polycrystal limiting their usefulness. The two schemes assume a uniform strain giving values that are often in the upper and lower limit numerical data respectively. This can be achieved by the Hill average, which is the mean between Voigt and Reuss averages [163][164].

The Voight bulk, B_V and shear, G_V moduli are given by:

$$B_V = \frac{2}{9}\left(C_{11} + C_{12} + 2C_{13} + \frac{1}{2}C_{33}\right)$$

$$G_V = \frac{1}{30}(C_{11} + C_{12} + 2C_{33} - 4C_{13} + 12C_{55} + 12C_{66})$$

Reuss bulk B_R, and shear G_R, moduli are given by:

$$B_R = \frac{[5C_{55}C_{66}(C_{11} + C_{12})C_{33} - 2C_{12}^2]}{C_{11} + C_{12} + 2C_{33} - 4C_{12}}$$

$$G_R = \frac{[5C_{55}C_{66}(C_{11} + C_{12})C_{33} - 2C_{12}^2]}{2\{3B_V C_{55}C_{66} + [(C_{11} + C_{12})C_{33} - 2C_{12}^2]\, C_{12} + (C_{55} + C_{66})\}}$$

The Hill bulk and shear moduli are given by,

$$B_H = \frac{1}{2}(B_V + B_R)$$

$$G_H = \frac{1}{2}(G_V + G_R)$$

Appendix B

Eigenvalues of the stiffness matrices

Table 1: Calculated eigenvalues for all compounds and functionals in Gpa from the elastic constants calculations

Compound	Functional	λ_1	λ_2	λ_3	λ_4	λ_5	λ_6
PtS_2	LDA	33.532	35.302	38.427	99.707	183.2	320.88
PtS_2	PBE	0.64665	0.64677	1.856	50.068	100.12	174.59
PtS_2	PBE+D2	50.479	55.376	68.33	123.87	225.84	395.31
PtS_2	PBE+D3	31.605	32.417	35.147	96.544	178.09	304.36
PtS_2	PBE+TS	21.663	23.449	24.415	77.052	148.01	260.3
PtS_2	PBEsol	13.344	27.386	29.097	87.227	164.19	287.32
PtS_2	optB86b	20.996	26.069	27.837	81.525	152.7	280.75
$PtSe_2$	LDA	29.166	32.918	49.621	85.438	151.4	288.56
$PtSe_2$	PBE	0.082564	1.4869	1.4876	42.249	84.458	147.14
$PtSe_2$	PBE+D2	39.704	45.906	56.039	105.99	183.34	341.85
$PtSe_2$	PBE+D3	28.003	31.174	40.876	78.607	141.22	261.81
$PtSe_2$	PBE+TS	23.124	25.109	40.621	67.725	124.74	241.88
$PtSe_2$	PBEsol	26.447	29.507	32.619	76.214	136.62	264.48
$PtSe_2$	optB86b	21.483	24.008	25.89	72.269	129.33	246.03
$PtTe_2$	LDA	18.109	24.737	47.574	112.07	164.08	507.97
$PtTe_2$	PBE	17.878	18.981	20.773	53.547	100.87	192.41
$PtTe_2$	PBE+D2	31.676	39.503	51.035	99.481	159.54	279.14
$PtTe_2$	PBE+D3	29.238	34.918	49.96	79.094	132.45	245.71
$PtTe_2$	PBE+TS	27.252	31.37	47.778	74.913	130.15	234.02
$PtTe_2$	PBEsol	28.461	33.043	43.8	67.806	116.81	239.53
$PtTe_2$	optB86b	26.113	30.361	41.912	64.741	111.37	240.24